2018

Physics of ignition and burn wave propagation in advanced thermonuclear fusion targets

Ross Jared Cortez

PHYSICS OF IGNITION AND BURN WAVE PROPAGATION IN ADVANCED THERMONUCLEAR FUSION TARGETS

by

ROSS JARED CORTEZ

A DISSERTATION

Submitted in partial fulfillment of the requirements
for the degree of Doctor of Philosophy
in
The Department of Mechanical and Aerospace Engineering
to
The School of Graduate Studies
of
The University of Alabama in Huntsville

HUNTSVILLE, ALABAMA

2018

In presenting this dissertation in partial fulfillment of the requirements for a doctoral degree from The University of Alabama in Huntsville, I agree that the Library of this University shall make it freely available for inspection. I further agree that permission for extensive copying for scholarly purposes may be granted by my advisor or, in his/her absence, by the Chair of the Department or the Dean of the School of Graduate Studies. It is also understood that due recognition shall be given to me and to The University of Alabama in Huntsville in any scholarly use which may be made of any material in this dissertation.

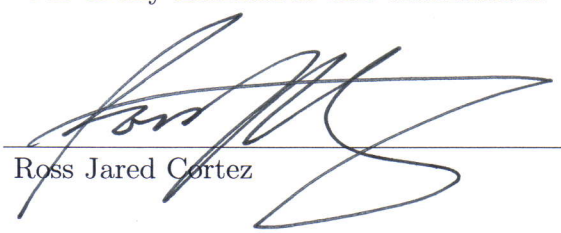

Ross Jared Cortez

6/17/18

(date)

DISSERTATION APPROVAL FORM

Submitted by Ross Jared Cortez in partial fulfillment of the requirements for the degree of Doctor of Philosophy in Mechanical Engineering and accepted on behalf of the Faculty of the School of Graduate Studies by the dissertation committee.

We, the undersigned members of the Graduate Faculty of The University of Alabama in Huntsville, certify that we have advised and/or supervised the candidate of the work described in this dissertation. We further certify that we have reviewed the dissertation manuscript and approve it in partial fulfillment of the requirements for the degree of Doctor of Philosophy in Mechanical Engineering.

Jason T Cassibry 5/30/18
Dr. Jason T. Cassibry (Date) Committee Chair

George H Miley 4/16/18
Dr. George H. Miley (Date)

William A Seidler II 6/4/2018
Dr. William Seidler, II (Date)

5/31/18
Dr. Gabe Xu (Date)

6/11/18
Dr. Gary P. Zank (Date)

6/18/18
Dr. Keith Hollingsworth (Date) Department Chair

Dr. Shankar Mahalingam (Date) College Dean

6/25/18
Dr. David Berkowitz (Date) Graduate Dean

ABSTRACT

School of Graduate Studies
The University of Alabama in Huntsville

Degree Doctor of Philosophy College/Dept. Engineering/Mechanical and Aerospace Engineering

Name of Candidate Ross Jared Cortez

Title Physics of Ignition and Burn Wave Propagation in Advanced Thermonuclear Fusion Targets

The objective of this dissertation is to explore the theoretical feasibility and technical potential of achieving thermonuclear ignition in a z-pinch plasma using a deuterium-lithium (D^6Li) fuel mixture at approximately solid density or higher. In this context, ignition occurs when a fusion plasma produces enough energy to sustain itself without auxiliary heating by external sources. The question of whether it is even possible to successfully ignite D^6Li targets to achieve a net positive energy gain finds a possible answer in two critical factors: (1) the high dependence of fusion reactivity on the density of the fuel, and (2) the physics of burn wave propagation through the target. The latter of these two factors is governed by the plasma stopping power, which is in turn heavily influenced by the density of the plasma. Ignition and high positive gain are greatly facilitated by localized (i.e. short) penetration depths of the fusion products into the surrounding cold fuel layer.

In this study, a recently formulated model of plasma stopping power is integrated into a Smoothed Particle Hydrodynamics (SPH) code called SPFMax in order to examine the behavior of burning fusion plasmas. The results show that the density of the fuel does indeed prove to be a heavy influence on the penetration depth.

Further, the conditions for which ignition will occur turn out to be more feasible than expected due to this high dependence of fusion reactivity on fuel density and the charge number ($Z = 3$) of fully ionized lithium. It is found that a central hotspot with a temperature of 40 keV between sections of colder fuel at 1 keV temperature will launch a burn wave in dense D^6Li. The ratio between the hotspot density and that of the exterior fuel (ρ_{hs}/ρ_{ext}) is also found to be a significant figure of merit in z-pinch target design. Additionally, simulations using initial conditions equivalent to the output of the Charger-1 pulsed power facility at 15 and 30 percent efficiency are used to predict the possible neutron yield that can be expected from a D^6Li pinch experiment using Charger-1 as the driver. The predicted yields are found to agree with a recent scaling model that was formulated based on combined data from multiple experiments.

The principal conclusion of this study is that thermonuclear ignition in a solid density D^6Li z-pinch plasma appears to be achievable in a parameter space that is accessible with current pulse power technology.

Abstract Approval: Committee Chair

Dr. Jason T. Cassibry

Department Chair

Dr. Keith Hollingsworth

Graduate Dean

Dr. David Berkowitz

TABLE OF CONTENTS

LIST OF FIGURES

LIST OF TABLES

There's an infinite number of monkeys outside who want to talk to us about this script for "Hamlet" they've worked out.

Douglas Adams

His lightnings enlightened the world: the earth saw, and trembled.

Psalm 97:4

CHAPTER 1

INTRODUCTION

> *It would mean a change in human conditions that I can only compare to the discovery of fire, that first discovery that lifted man above the brute.*
>
> —H.G. Wells, *The World Set Free*

1.1 Unfinished Obelisks

December 14, 1972 is the question mark placed at the end of one of the greatest interrogative statements in history: *Will mankind ever set foot on the surface of the moon again?* An affirmative answer to this question necessarily implies humanity's emergence into a new era of prosperity simply because the next commitment made to land on the moon will be to establish a permanent presence there, facilitating travel and commerce throughout the solar system [1].

At 11:34 p.m. that day, Gene Cernan stood alone on the surface of the moon, having taken one last look at the Earth-rise over the horizon, and spoke to posterity:

> ... I believe history will record that America's challenge of today has forged man's destiny of tomorrow.

Indeed, although this may have been true as can be seen through the numerous benefits and technologies derived from the space program, the unbridled optimism of his statement is palpable. With the gift of hindsight, this optimistic attitude is certainly warranted: the trajectory of modern society is invariably due not only to the technical, but also the political ramifications of the Apollo program and its progeny. Simultaneously, however, it is difficult to ignore the Saturn V rockets that lay unused in Texas, Florida, and Alabama, testifying to what now seems to be an anomalous event in American history. They are the unfinished obelisks that remain as monuments to and reminders of a dream that, while not broken, now lies dormant in the human psyche [2]. Ever since the retirement of the shuttle program in 2011, the dominant question has been: *What now?*

1.2 Quo Vadis, Space Travel?

It has been forty-five years since man's last tentative steps were taken on the moon. Since then, the relative importance of space travel to the majority of the population has diminished, leaving a technological vacuum in the nation's apce program.The motivations for the expansion of human civilization into space have been listed in numerous places, but Dr. Terry Kammash made an eloquent case when he stated:

> Although the debate on the wisdom of such an undertaking rages on between those who bemoan the prohibitive cost of such a venture and those who boast of the economic benefits that may accrue from reaping the

> riches of Mars and other planets, the fact remains that without a frontier to conquer humanity will be doomed to stagnation, will lose its spirit of creativity and inquisitiveness, and ultimately surrender the bouyancy and exuberance that seem to come only from the freedom associated with the existence of frontiers ... Yet to secure these riches people on Earth must become spacefaring for which suitable transportation must be developed and perfected [3].

This is a qualitative argument, to be sure, but the point being made is that without continuing to push outward to new frontiers there is an upper limit to the progression of civilization.

The rest of this chapter is dedicated to discussing the motivations for this dissertation. Section 1.3 explains the uses of fusion propulsion as a logical method of travel within the solar system, followed by a discussion of the reasoning behind using D^6Li as a practical fuel in fusion propulsion systems in Section 1.4. The objectives of this dissertation are defined in Section 1.6, and the layout of content in subsequent chapters is in Section 1.7.

1.3 The Case for Fusion Propulsion

Human exploration of space beyond low earth orbit (LEO) is severely hampered by Newton's second law. The fundamental limitation is exemplified by the rocket equation [4]:

$$\frac{m_f}{m_0} = e^{\frac{-\Delta v}{v_e}} \tag{1.1}$$

Equation 1.1 shows the fundamental tradeoff between exhaust velocity and required fuel mass. For voyages beyond the moon, mission Δv values range from $\sim 10^4$ to $\sim 10^5$ m/s [5], requiring increasingly high exhaust velocities to keep the fuel mass fraction as low as possible. The increase in exhaust velocity comes at the expense of thrust since it takes more energy per unit mass to accelerate a gas, further requiring large power supplies [5]. Any reduction in thrust will increase the total trip time. Longer trip times compound the inherent hazards of space travel to astronauts, making one of the primary objectives of propulsion system design to be producing a reasonable balance between trips times and payload mass fraction. Shorter durations of travel will reduce the radiation doses astronauts receive via cosmic radiation. Faster trips also decrease the overall atrophy of muscle tissue as well as the psychological impact of long journeys in confined spaces on the astronauts. These factors balance the enhanced "quality of life" that comes from larger payload mass fractions which also increase the mission reliability. In considering these competing, yet complementary, aspects of space travel, it becomes evident that achieving high exhaust velocities with minimal loss of thrust is desirable.

The reasons for fusion and fission-fusion hybrid propulsion systems have been discussed in review articles such as [6]. Large energy gains from fusion enable large specific powers ($\alpha \sim 1-10\text{kW/kg}$) and specific impulse ($I_{sp} \sim 10^4 - 5\times10^4$), reducing overall trip times. Indeed, fusion propulsion reduces round-trip missions to Mars, for

example, to under one year due to the higher specific powers. These factors provide the first key motivation for this dissertation.

1.4 D^{6}Li: A Practical Fuel

The second motivating factor for this study follows from the first since the chosen method of propulsion and the fuel used heavily influence the mission elements mentioned above. In a fusion plasma, the number of reactions per second is

$$\frac{dN}{dt} = \frac{n_i n_j}{1+\delta_{ij}} \langle \sigma v \rangle_{ij} V \tag{1.2}$$

for particle species i and j. n is the number density in m^{-3}, $\langle \sigma v \rangle$ is the reactivity, V is the volume of the reacting plasma, and $\delta_{ij} = 1$ for $i = j$ and 0 for $i \neq j$. Although the DT reaction is favored because the cross section is higher by an order of magnitude or more compared with other reactions, it produces high energy neutrons. Since neutrons cannot be confined, they represent a loss in the system and are deleterious to surrounding structures and materials. Aneutronic fuels are therefore highly desired; however, they also require more energy to ignite. Another issue, frequently ignored in the fusion community, is the cost of the fuel and its abundance.

The costs of prominent fusion fuels are illustrated in Table 1.1. It is immediately evident that tritium is very expensive. This is because it is produced by nuclear fission through an uncommon branching ratio. Helium-3 (^{3}He) is also costly because, although it is abundant in the solar system, it is rare on Earth. Since it is dependent on tritium decay, ^{3}He production is then limited by tritium production. The other fu-

els such as lithium isotopes, boron-11 (^{11}B), deuterium, and hydrogen have unit costs orders of magnitude cheaper as well as more abundant [6]. This fact is also illustrated in Table 1.2, which lists the fuel cost per pulse assuming a 1 GJ energy output and 1 cm^3 reacting volume. The data in Table 1.2 show that among the common reactions considered for fusion energy production, D^{6}Li is only surpassed by pure deuterium in cost-effectiveness.

Figure 1.1 shows total fuel costs for a mission with a 100 metric ton (mT) payload and specific power of 1 kW/kg for reactions DT, D^{3}He, DD, D^{6}Li, and p^{11}B. The difference in cost between missions that use tritium or ^{3}He and the other fuels is about three orders of magnitude; a significant disparity making the use of tritium or ^{3}He impractical without significant investment in tritium breeding infrastructure.

Table 1.1: Cost of common fusion fuel components in USD per kg [6].

Fuel	Cost per kg
Tritium	$3,000,000.00
^{3}He	$1,230,792.00
^{11}B	$4,000.00
^{7}Li	$7,500.00
^{6}Li	$6,000.00
Li	$270.00
Deuterium	$640.00
Hydrogen	$100.00

Table 1.2: Cost per 1 GJ shot of common fusion fuels in USD, assuming a 1 cm^3 reacting volume.

Fuel	Cost [USD/shot]
DT	4.47×10^{-5}
DD	5.51×10^{-9}
D^3He	3.51×10^{-6}
$p^{11}B$	5.72×10^{-8}
D^6Li	2.23×10^{-8}
p^7Li	3.97×10^{-8}

In the context of reactors or propulsion, the D^6Li fuel cycle is rarely discussed. McNally previously showed that the fuel cost per kg was cheaper than other options by multiple orders of magnitude [7]. The FIREBALL fusion propulsion concept considered field reversed configurations (FRCs) that are compressed to thermonuclear ignition in a lithium-lined cone [8]. Additionally, Winterberg has written about this fuel cycle in the context of inertial confinement fusion (ICF) [9], and lithium liners are also being considered for compression of a translating FRC for propulsion [10]. In a series of exploding wire experiments by Katzenstein and Sydor [11], D^6Li wires were included among the tests and observed neutron yields $\sim 10^6$ per discharge.

The motivation for investigating solid D^6Li as a possible fuel is supported by two observations. First, consider Equation 1.2, giving the number of reactions occuring per second in a given volume. Assuming a 50-50 mixture of the reacting species, this reaction rate is quadratic with the number density, n. D^6Li exists as

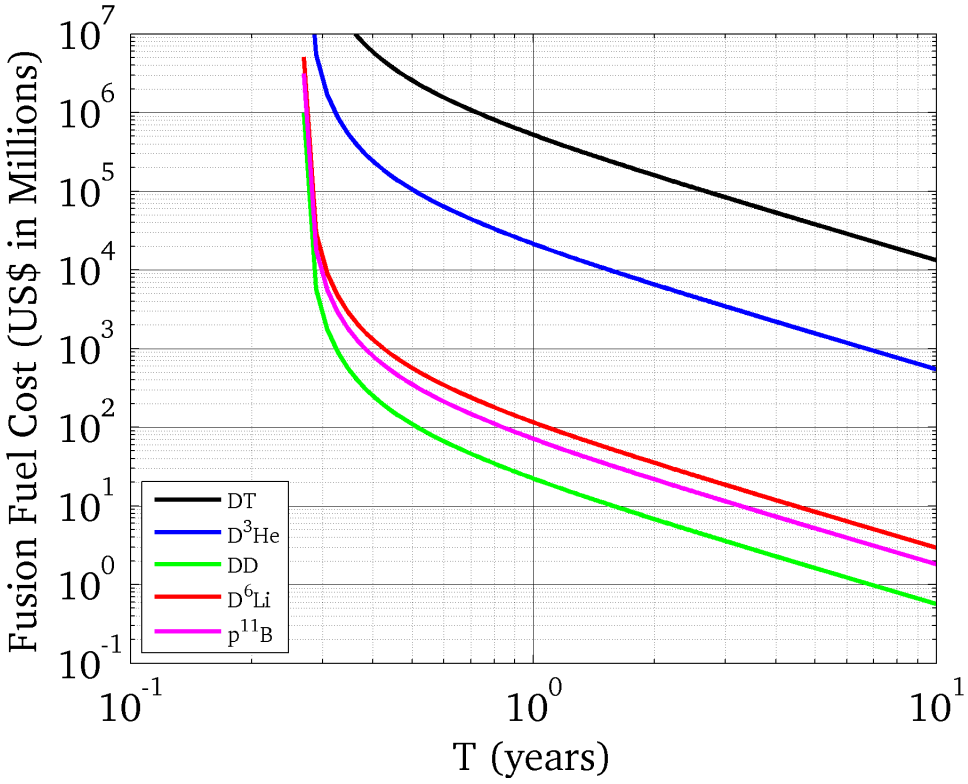

Figure 1.1: Cost comparison of fusion fuels in Millions USD vs. T for a 100 mT payload and 1 kW/kg output [6]

.

a salt with a mass density of ∼800 kg/m^3, corresponding to a number density of $\sim 10^{25}$ m^{-3}. This implies that working with solid targets will then obviate the need for high compression ratios and possibly create initial conditions for a highly reactive plasma. Second, since D^{6}Li is a solid at room temperature unlike the solid targets used in ICF like frozen DT ice, cryogenic storage is not required. This lowers the complexity of the fuel system which will increase its reliability.

1.5 The Physics of Burning Fusion Plasmas

A fusion plasma is considered to "burn" when the charged particles produced by fusion reactions in the plasma deposit their energy back into the plasma. The energy deposited by these fusion products raises the temperature of the plasma, causing more reactions to occur, releasing more energy to heat the plasma. This process is dominated by electron thermal conduction and the stopping power of the plasma, which is defined as the rate that energy is tranferred from the charged fusion products to the surrounding plasma. Charged particle products of fusion reactions lose energy through small- and large-angle collisions. The small-angle collisions are caused by Coulomb interactions, which act like a frictional drag force on the fusion products by local background species in the plasma [12]. Large-angle collisions are caused by binary interactions between particles in the plasma, and occur mainly near the end of a fusion product's range after it has lost the majority of its birth energy. As the density of the plasma increases, such collisions become more frequent and must be taken into account [13, 14].

Implementation of burn physics in a computational model is difficult due to the complex physics involved in the stopping power [15–18]. This is because it is extremely difficult to account for all possible interactions between ions and electrons in the plasma. Additionally, the stochastic nature of particle interactions and the methods used to model them introduce numerical obstacles that are hard to overcome without making simplifying assumptions [19]. For dense plasmas the calculations are made more complex because quantum effects must be accounted for since the scale

of the interactions approaches the thermal (deBroglie) wavelength of the electrons in the plasma. Most stopping power models make differing assumptions related to the condition of the plasma, which affect their fidelity and accuracy (see, for example, [13, 15, 16, 20, 21]).

The difficulties and assumptions mentioned here are further explored in Chapter 3 where a recent model, formulated by Grabowski *et al.* (see reference [17]), is discussed that accounts for the results of commonly used stopping power models. This model is implemented as part of a smoothed particle hydrodynamics (SPH) code to simulate burning fusion plasmas in this study. It was chosen due to its generality, accounting for the strengths of multiple state-of-the-art computational models used today. The results presented in Chapter 5 of this dissertation therefore reflect the current, state-of-the-art understanding of the physics governing burning plasmas, and provide a notional answer to the question of whether it is even possible to successfully ignite D^6Li targets without requiring extremely high driver energies to initiate the reactions.

1.6 The Objective of This Dissertation

The principal objective of this dissertation is to explore the theoretical feasibility and technical potential of achieving thermonuclear ignition in a z-pinch plasma using a deuterium-lithium fuel mixture. This is a unique contribution to the field since there is very little work examining burn in fusion targets using advanced fuels like D^6Li. The study of so-called "spark ignition" (ignition via hotspot) in solid density z-pinches is also a unique contribution to the development of fusion target designs.

A better understanding of the requirements for ignition in the targets studied here will inform future work designing in-space propulsion systems that will eventually be used for travel and human exploration within the solar system.

Harnessing the simplicity of the z-pinch method of confinement combined with the practicality of the D^6Li fuel cycle in a creative manner has the potential to either break through or otherwise circumvent key obstacles that have continually disrupted the development of two ultimately revolutionary technologies: (1) fusion power generation, and (2) interplanetary space propulsion. This work is therefore an essential step toward overcoming these obstacles.

1.7 Outline

A brief overview of fusion confinement concepts and the z-pinch plasma configuration of interest in this study is given in Chapter 2. The physics of ignition and burn wave propagation is also discussed along with target instabilities and how they might increase the possibility of achieving thermonuclear ignition. Chapter 2 also includes discussion of some useful parameters that quantify the ignition requirements of a plasma. The effects of interparticle interactions and plasma stopping power are then described in Chapter 3, followed by an overview of the numerical methods used in this study in Chapter 4. Chapter 5 gives the results of the burning plasma simulations followed by analysis and discussion of their implications. Finally, conclusions drawn from the analysis and some notional experimental designs for testing them are discussed, followed by a few closing remarks in Chapter 6.

CHAPTER 2

NUCLEAR FUSION: A BRIEF OVERVIEW

Plasma physics has a lot in common with summoning spirits from the vasty deep. Anyone can call them, but will they come?

—T. A. Heppenheimer

While fusion still promises to be an enabling technology that can be compared to the prehistoric utilization of fire, the quest has taken so long, and been so short in fulfillment, that many question the fruitfulness of the endeavor.

—R. Kirkpatrick

2.1 Overview

What follows in this chapter is a brief overview of the "traditional" methods used to confine fusion plasmas in Section 2.2.1 and Section 2.2.2, followed by a description of magneto-inertial fusion (MIF) in Section 2.2.3, which seeks to combine the favorable aspects of the traditional methods within a more practical, cost effective concept. The z-pinch method of confinement is described in Section 2.4 followed by discussion of the Rayleigh-Taylor instability (RTI) and its relationship to beam-target fusion yields in Section 2.4.1.

2.2 The Crucible of Confinement

Nuclear fusion is the process by which two nuclei collide, overcoming the Coulomb barrier and merging to form a heavier nucleus and another lighter charged particle [22]. The energy released in this process is proportional to the difference in the total mass of the particles after a collision occurs, corresponding to Einstein's mass-energy equivalence: $E = mc^2$. All energy systems are fundamentally required to acquire a sufficiently high reaction rate density to be viable. There are a number of exothermic fusion reactions (see Table 2.1) that can be utilized to do so. Achieving ion energies that overcome the Coulomb barrier is not difficult; it is the predeliction of the charged particles involved to scatter upon their interaction that makes further reactions unlikely. This deleterious behavior necessitates some method of confinement to make a fusion system feasible. The requirement, then, is to sustain a high temperature ($\sim$10 - 100 keV) plasma within a sufficiently small reaction volume over a period of time long enough for a large number of fusion reactions to occur.

2.2.1 Magnetic Confinement (MCF)

Confining a plasma at temperatures high enough for fusion reactions to occur necessitates the choice between two design requirements: (1) use materials capable of withstanding the extreme conditions of a fusion plasma to confine the reaction, or (2) maintain a stand-off distance between the plasma and the material walls to prevent the plasma from cooling and the reactor from melting down. Magnetic Confinement Fusion (MCF) takes advantage of the charged nature of the plasma components to

Table 2.1: Nuclear fusion reactions using both common and advanced fuels [23].

	Reactants		Products
1	${}^{2}_{1}D + {}^{3}_{1}T$	$\longrightarrow$	${}^{4}_{2}He$ (3.45 MeV) + n (14.1 MeV)
2a	${}^{2}_{1}D + {}^{2}_{1}D$	$\longrightarrow$	${}^{3}_{2}He$ (0.82 MeV) + n (2.45 MeV)
2b	${}^{2}_{1}D + {}^{2}_{1}D$	$\longrightarrow$	${}^{3}_{1}T$ (1.01 MeV) + p (3.02 MeV)
3	${}^{2}_{1}D + {}^{3}_{2}He$	$\longrightarrow$	${}^{4}_{2}He$ (3.6 MeV) + p (14.7 MeV)
4a	${}^{2}_{1}D + {}^{6}_{3}Li$	$\longrightarrow$	${}^{4}_{2}He$ (11.2 MeV) + ${}^{4}_{2}He$ (11.2 MeV)
4b	${}^{2}_{1}D + {}^{6}_{3}Li$	$\longrightarrow$	$p + {}^{4}_{2}He + {}^{3}_{1}T +$ 2.6 MeV
4c	${}^{2}_{1}D + {}^{6}_{3}Li$	$\longrightarrow$	${}^{7}_{4}Be + n +$ 3.4 MeV
5	$p + {}^{6}_{3}Li$	$\longrightarrow$	${}^{4}_{2}He$ (1.7 MeV) + ${}^{3}_{2}He$ 2.3 MeV
6a	$p + {}^{7}_{3}Li$	$\longrightarrow$	$2({}^{4}_{2}He)$ + 17.3 MeV
6b	$p + {}^{7}_{3}Li$	$\longrightarrow$	${}^{3}_{4}Be + n -$ 1.6 MeV
7	$p + {}^{11}_{5}B$	$\longrightarrow$	$3({}^{4}_{2}He)$ + 8.7 MeV
8	$n + {}^{6}_{3}Li$	$\longrightarrow$	${}^{3}_{1}T + {}^{4}_{2}He$ + 4.8 MeV
9	$n + {}^{7}_{3}Li$	$\longrightarrow$	${}^{3}_{1}T + {}^{4}_{2}He -$ 2.5 MeV

achieve the second of these design options by using magnetic fields to contain the plasma (Figure 2.1). This method of confinement is characterized by lower density ($\sim 10^{14}$ cm^{-3}) plasmas and longer confinement times (multiple seconds) [24].

2.2.2 Inertial Confinement (ICF)

Inertial Confinement Fusion (ICF) (Figure 2.2) relies exclusively on mass inertia with no externally applied means of confinement. In contrast with the essentially steady-state nature of MCF, the timescales involved in ICF are incredibly short

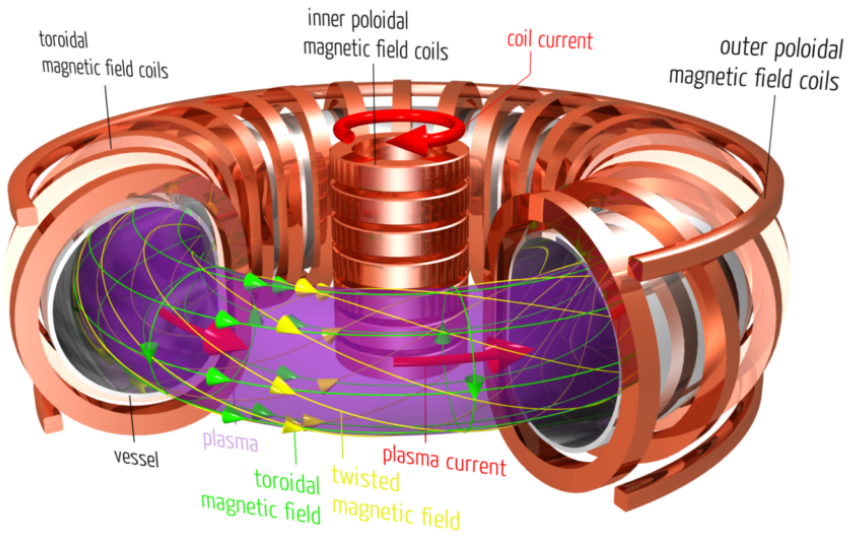

Figure 2.1: Schematic drawing of the tokamak magnetic confinement method. [Credit: Kurt Gimbel, University of Illinois, *https* : *//publish.illinois.edu/kgimbel2/plasma − fusion/*; Last Accessed 01/25/2018]

($\lesssim 10^{-12}$sec). The short timescale therefore implies that extremely high densities are required to achieve high reaction rates [24]. The most common process used to achieve such high plasma densities occurs in a four stage process (Figure 2.3):

1. An external driver delivers a high power pulse of energy to the target, irradiating the exterior shell forming an ablated plasma on its surface;

2. The interior shell reacts to the expansion of the ablator via conservation of momentum, compressing inward;

3. A "hotspot" is formed at the center of the target by the compression work from the outward momentum of the ablator, causing the fuel to ignite and burn;

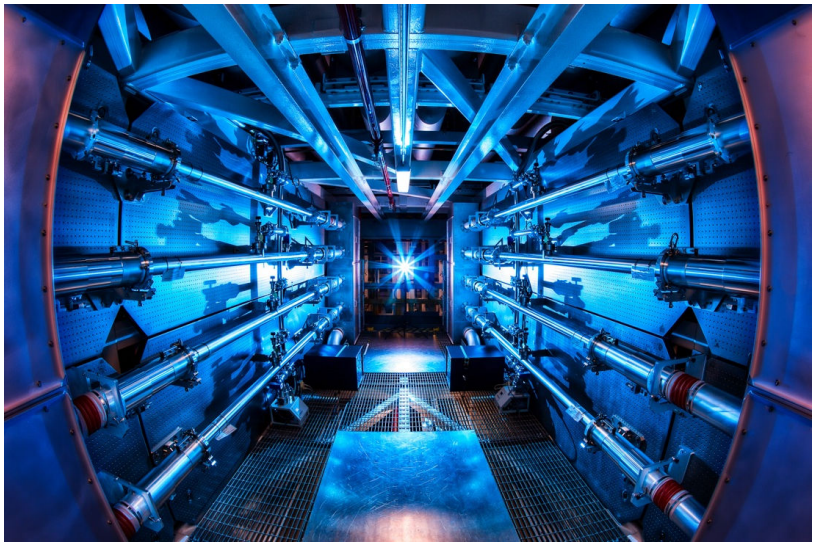

Figure 2.2: An inertial confinement experiment in the OMEGA laser facility located at the University of Rochester, New York.

4. The central burning fuel expands outward to heat the rest of the fuel, causing it to burn.

The concept of thermonuclear ignition due to a hotspot launching a burn wave through the rest of the fuel in the target plays an important role in this study, as will be seen in the coming chapters. It follows that many of the parameters used to characterize ICF targets will also be applicable to z-pinch plasmas due to the ease of formation of hotspots during the pinch compression phase (see Section 2.4.1). This particular point is noted here to contextualize the strong relationship between the two seemingly incongruous methods of confinement and to point out that there are similarities in how their particles interact with each other. This will be discussed further in Chapter 3.

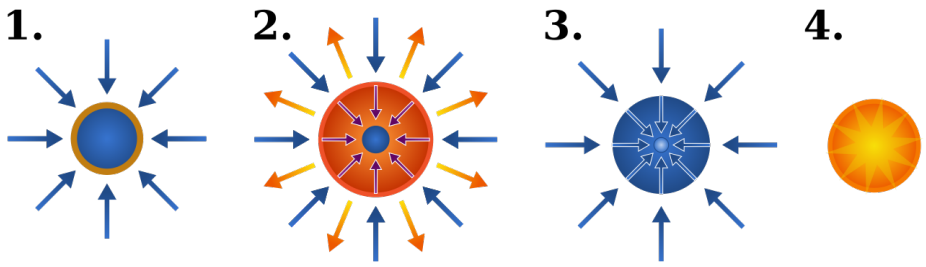

Figure 2.3: Stages of ICF implosion: (1) An external driver delivers a high power pulse of energy to the target, irradiating the exterior shell; (2) Interior shell reacts to expansion of the ablator, compressing inwards; (3) A "hotspot" is formed at the center of the target by the compression work from the outward momentum of the ablator, igniting the fuel; (4) Central burning fuel expands outward to heat and burn the rest of the fuel. [Credit: Benjamin D. Esham, marked as public domain image. *https://commons.wikimedia.org/wiki/File:Inertial_confinement_fusion.svg*; Last Accessed 03/18/2018]

2.2.3 Magneto-Inertial Confinement (MIF)

Magneto-Inertial Fusion (MIF) (also called Magnetized Target Fusion, or MTF) [25,26] is a hybrid approach to confinement combining favorable aspects of both MCF and ICF. This method uses magnetic fields to reduce thermal losses and enhance the self-heating of the fuel by charged fusion products. Similar to ICF, the target is compressed at a high velocity to achieve high densities over longer timescales ($\sim$ 100 nsec $-$ 1μsec). The magnetic fields lower the threshold for ignition thereby allowing lower implosion velocities to be used to compress the target.

When considering fusion propulsion systems for in-space travel, MIF has features that make it an attractive confinement approach. First, the density regime spans (roughly) from the molecular density of air at sea level ($\sim 10^{25}$ m^{-3}) up to solid density ($\sim 10^{29}$ m^{-3}). This means the reacting volume will only be $\sim 1-10$ cm^3, and the total energy required for fusion burn can potentially be $< 10^6$ J [27]. Second, cross

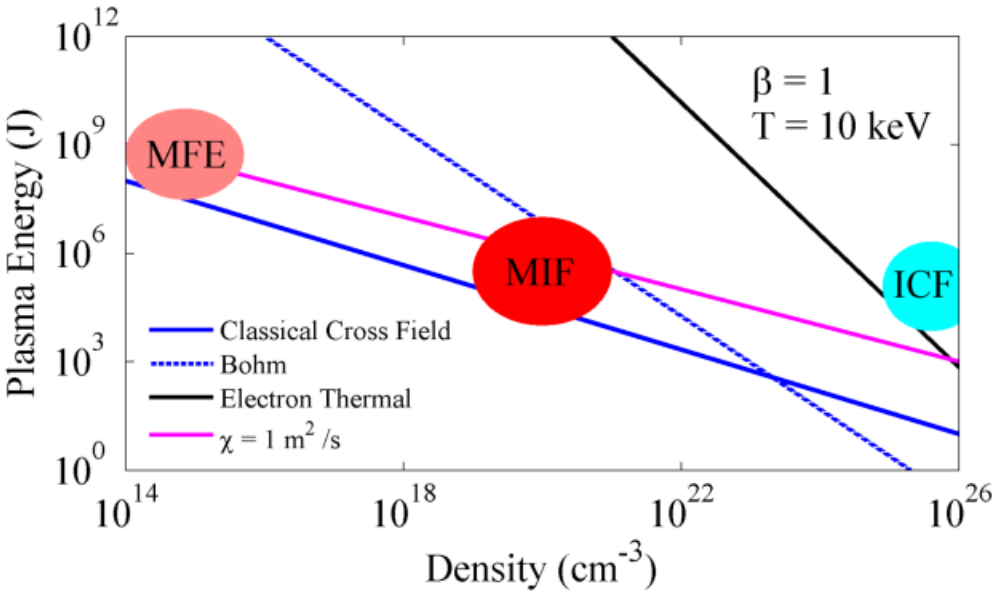

Figure 2.4: MIF parameter space [6].

field electron thermal conduction is suppressed by the presence of the magnetic field, reducing heat loss and thus the power required to compress and heat the target is lowered to $\sim 10^{12} - 10^{15}$ W. Since pulsed power systems at such power levels already exist (e.g. Shiva Star, Figure 2.5), the costs of accessing the MIF parameter space are considerably reduced [28].

Figure 2.4 illustrates the intermediate parameter space of MIF in relation to those of MCF and ICF. Approaches to reaching the MIF parameter space range from using cylindrical metal shells to implode a magnetized plasma called a compact toroid [29–31] (Figure 2.5) to using multiple plasma guns to create an imploding liner that compresses a spherical magnetized target [32, 33] (Figure 2.6).

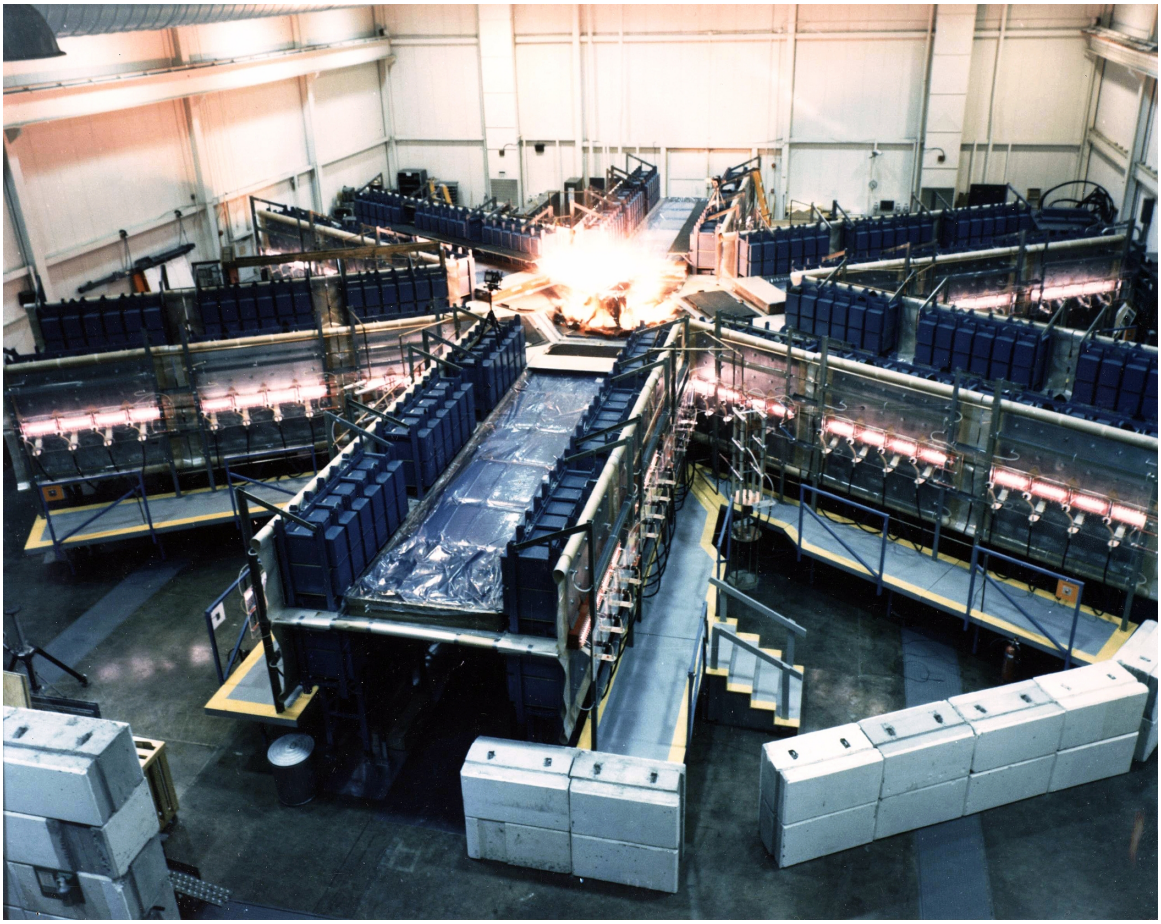

Figure 2.5: A liner implosion experiment on the Shiva Star pulsed power facility located at Kirtland Air Force Base, Albuquerque, NM. [Credit: U.S. Air Force, *https : //upload.wikimedia.org/wikipedia/commons/d/da/Shiva*$_s$*tar.jpg This image or file is a work of a U.S. Air Force Airman or employee, taken or made as part of that person's official duties. As a work of the U.S. federal government, the image or file is in the public domain in the United States.* Last Accessed 01/25/18]

2.3 The Physics of Ignition

Thermonuclear ignition and burn occurs in a plasma when the energy released by fusion reactions in the plasma exceeds all energy losses so that no further auxiliary heating is required to keep the plasma burning. Depending on the fuels involved and relevant loss mechanisms, specific conditions are required in the plasma to achieve

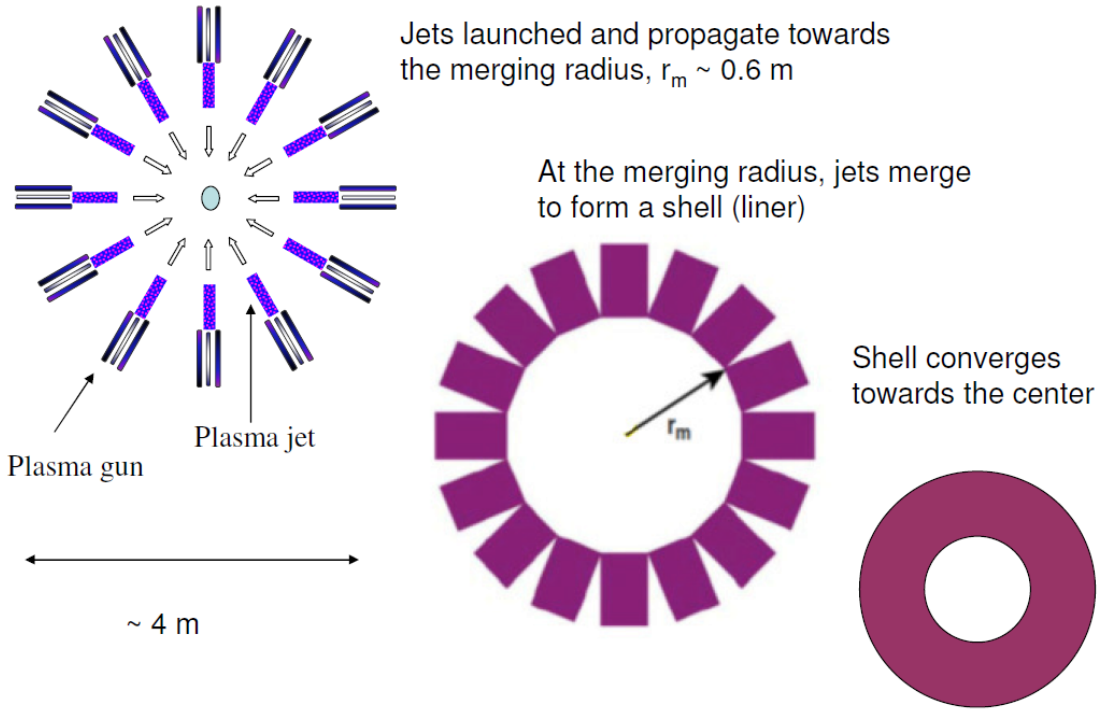

Figure 2.6: Plasma Jet driven Magneto-Inertial Fusion (PJMIF) concept drawing [34].

ignition [24]. The idea of "ignition" is defined along with the concept of "target energy gain" in Section 2.3.1. Two parameters commonly used to estimate minimum requirements for ignition to occur are then reviewed in Section 2.3.2.

2.3.1 Fusion Burn and the Definition of Ignition

In comparison with the traditional notion of "burn" (oxidation reactions), one of the principal issues of thermonuclear burn is the fact that ignition temperatures and reaction cross sections are orders of magnitude larger and smaller, respectively. However, the payoff comes from the energy per reaction being millions of times larger than those of chemical reactions [9]. A successful fusion system will operate in such

a way that any power losses are compensated by the fusion output power. This can be represented by:

$$Q = \frac{P_{fus}}{P_{aux}} > 1 \tag{2.1}$$

known as the reactor Q [24]. In this scenario no auxiliary heating is required and the fusion plasma becomes self-sustaining, i.e. $P_{aux} \to 0$ such that $Q \to \infty$. This condition is referred to as *thermonuclear ignition*. The *target energy gain* compares the energy released by fusion, E_{fus}, with the energy delivered to the target by the driver (e.g. Marx bank), E_d:

$$G = \frac{E_{fus}}{E_d}. \tag{2.2}$$

For pulsed systems like the ones examined in this study, ignition is required to achieve a high gain.

2.3.2 Ignition Conditions

Confinement requirements for thermonuclear ignition and sustained reactions can be represented by certain figures of merit derived from examining the power balance of a fusion plasma. Two key parameters, the Lawson criterion and the confinement parameter ρR, are useful when determining the minimum conditions necessary for ignition to occur. These two parameters are discussed in the following sections.

2.3.2.1 Lawson Criterion

Consider a plasma consisting of two oparticle species with densities n_1 and n_2. The rate of fusion reactions, R, is

$$R = n_1 n_2 \langle \sigma v \rangle_{12} \tag{2.3}$$

where v is the relative velocity of two nuclei and σ is the fusion cross-section. The amount of energy produced for a given time, τ, will depend upon the kinetic energy of the reaction products, W, and the reaction rate R. This is expressed as

$$E_{fus} = R\tau W = n_1 n_2 \langle \sigma v \rangle_{12} \tau W \tag{2.4}$$

where W is given in MeV. To achieve a net positive energy from the plasma the energy from fusion reactions must be larger than the total thermal energy of all the particles, i.e.

$$E_{fus} > E_{kin} \Rightarrow n_1 n_2 \langle \sigma v \rangle_{12} \tau W > 3 n k_B T \tag{2.5}$$

where the electron and ion temperatures are assumed to be equal such that

$$T_i = T_e = T \Rightarrow \frac{3}{2} n k_B (T_e + T_i) = \frac{3}{2} n k_B (2T) = 3 n k_B T \tag{2.6}$$

Assuming an equimolar mixture of fuel so that $n_1 = n_2 = n/2$, Equation 2.5 can be rearranged:

$$n\tau > \frac{12 k_B T}{\langle \sigma v \rangle_{12} W}. \tag{2.7}$$

This relation is known as the Lawson criterion [35].

Table 2.2: Example confinement parameters in MCF, MIF and ICF for deuterium-tritium fuel. MCF and ICF values are extracted from [36]

	MCF	MIF	ICF
Particle density $n_e\,[cm^{-3}]$	10^{14}	10^{19}	10^{26}
Confinement time $\tau\,[s]$	10	10^{-4}	10^{-11}
Lawson criterion $n_e\tau\,[s\cdot cm^{-3}]$	10^{15}	10^{15}	10^{15}

For DT fuel, a temperature of about 5 keV is required so that the fusion particles have kinetic energy sufficient to achieve a reaction rate high enough for ignition. With $W_{DT} = 17.6$ MeV the Lawson criterion is

$$n\tau \gtrsim 10^{15}\ \mathrm{s}\cdot\mathrm{cm}^{-3}. \tag{2.8}$$

Further examination of this inverse relationship helps to illustrate the rationale behind the disparate approaches to fusion confinement. For the extremely high densities of ICF, the Lawson criteron requires short confinement times on the order of picoseconds ($\sim$10 ps). At the opposite end of the spectrum, MCF attempts to fulfill the Lawson criterion by confining lower plasma densities for a longer period of time on the order of multiple seconds. Examples of these parameters for MCF and ICF are shown in Table 2.2. Values for the MIF parameter space are included to add context for the purposes of this study.

2.3.2.2 Confinement Parameter: ρR

At any time during the nuclear burn period, the total ion population in the burn volume decreases with time due to fusion reactions occurring at the rate

$$\frac{dN_b}{dt} = -2\int_{V_b} n_1(t)n_2(t)\langle\sigma v\rangle_{12}d^3r. \tag{2.9}$$

For an equimolar mixture $n_1 = n_2 = n_0/2$ this would be

$$\frac{dN_b}{dt} = -\frac{1}{2}\int_{V_b} n_i^2(t)\langle\sigma v\rangle_{12}d^3r \tag{2.10}$$

where n_i is the fuel ion number density. Assuming that during the burn time τ_b the fuel ion density and temperature are uniform and only a function of time, the ion density in the burn volume can then be related to the total number of fuel ions by:

$$n_i(t) = \frac{N_b(t)}{V_b} \Rightarrow V_b\frac{dn_i}{dt} = \frac{dN_b}{dt} \tag{2.11}$$

so that

$$V_b\frac{dn_i}{dt} = -\frac{n_i^2(t)}{2}\langle\sigma v\rangle\int_{V_b} d^3r = -\frac{n_i^2(t)}{2}\langle\sigma v\rangle V_b. \tag{2.12}$$

Equation 2.12 can then be integrated over time

$$\int_{n_{i,0}}^{n_{i,f}} \frac{dn_i}{n_i^2(t)} = -\frac{1}{2}\int_0^{\tau_b}\langle\sigma v\rangle(t)dt \tag{2.13}$$

where $n_{i,0}$ is the initial ion density at time $t = 0$ and $n_{i,f}$ is the final ion density at time $t = \tau_b$. Integrating Equation 2.13 followed by a little algebra leads to an expression for the fusion burn time:

$$\tau_b = \frac{2}{\overline{\langle \sigma v \rangle}} \left(\frac{1}{n_{i,f}} - \frac{1}{n_{i,0}} \right) \tag{2.14}$$

where$\overline{\langle \sigma v \rangle}$ is the reactivity averaged over the burn period: $\overline{\langle \sigma v \rangle} = \frac{1}{\tau_b} \int_0^{\tau_b} \langle \sigma v \rangle(t) dt$. Defining the burn fraction as

$$f_b = \frac{n_{i,0} - n_{i,f}}{n_{i,0}} \tag{2.15}$$

the fusion burn time can then be written as

$$\tau_b = \frac{2}{\overline{\langle \sigma v \rangle}} \frac{\overline{m_i}}{\rho_b} \left(\frac{f_b}{1 - f_b} \right) \tag{2.16}$$

where $\overline{m_i}$ is the average ion mass and ρ_b is the target density during the burn. Since the target is not static, there is a limited amount of time for the fuel to burn before it falls apart. Therefore, the natural goal is to confine the hot plasma for as long as possible to give the fuel time to burn, i.e. $\tau_{conf} > \tau_b$. The confinement time can be estimated by considering how fast the plasma will expand before the fuel conditions become inadequate for fusion reactions to take place. This can be expressed as

$$\tau_{conf} = \frac{R_b}{v_{exp}} \tag{2.17}$$

where v_{exp} is the speed at which the mass of the target moves outward. At this velocity, the kinetic energy of the plasma is of the order of the ion thermal energy:

$$\frac{1}{2}\overline{m_i}v_{exp}^2 \approx \frac{3}{2}k_B T_i \Rightarrow v_{exp} \approx \left(\frac{3k_b T_i}{\overline{m_i}}\right)^{1/2}. \tag{2.18}$$

Using Equation 2.16 with Equation 2.17 and Equation 2.18 then leads to an expression for the confinement parameter

$$\rho_b R_b > \frac{2\overline{m_i}v_{exp}}{\overline{\langle\sigma v\rangle}}\left(\frac{f_b}{1-f_b}\right). \tag{2.19}$$

This parameter illustrates the relationship between initial target size and density based on a specified burn fraction. Since the thermodynamic state of the plasma relies primarily on its density and temperature, the ρR confinement parameter serves as a useful tool for target design by providing minimum initial conditions based on the desired outcome.

2.4 Z-Pinch Research & Development

The pulsed z-pinch approach to MIF confinement is a simple, practical configuration that has recently received renewed interest in the fusion community due to more advanced pulsed-power technology and deeper understanding of the plasma physics involved [37]. A z-pinch [38, 39] is a radial implosion of a cylindrical plasma caused by compression of a strong azimuthal magnetic field on the order of thousands of Tesla (see Figure 2.8 below) produced by a current flowing down the length of the plasma (Figure 2.7). This concept is used in nuclear weapons effects (NWE) testing

for the defense industry, fusion confinement, and in industrial applications such as material coating for thermal protection systems (TPS) on re-entry vehicles or applying EMI/RFI shielding to enclosures. A few notable facilities include MAGPIE at Imperial College, London [40–42], the Z Machine at Sandia National Laboratories (SNL) [43, 44], and the DECADE facility, previously located at the Arnold Engineering Development Center (AEDC) in Tullahoma, Tennessee [45].

Possibly the earliest demonstration of the z-pinch was work done by Martinus van Marum in Amsterdam in 1790 related to the defense industry of the day. He employed a 1 kJ capacitive energy store composed of 100 Leyden jars, which was discharged into a 1 meter long wire causing an explosion and vaporization. Bennet was the first to analyze these configurations in 1934, followed by Tonks in 1937 [46] who introduced the term "pinch". Most of the pioneering work in steady state z-pinches occurred in the 1950s, with the realization that instabilities prevented breakeven fusion. Most of the neutrons observed occurred at the rapid disruption of the pinch at the late time maturation of the instabilities. The neutron yield was often asymmetric, and produced by an ion acceleration process which is not yet fully understood. The yield is often referred to as "beam-target" (see Section 2.4.1) [38]. The inherent instabilities halted z-pinch work in the 1960s, giving way to toroidal confinement approaches. The development of the Marx bank in the 1970s motivated renewed interest in z-pinches as pulsed devices.

A pinch can reach radial equilibrium in a few nanoseconds, evolving with a Bennett type equilibrium [38], which is the state of the plasma where the radial

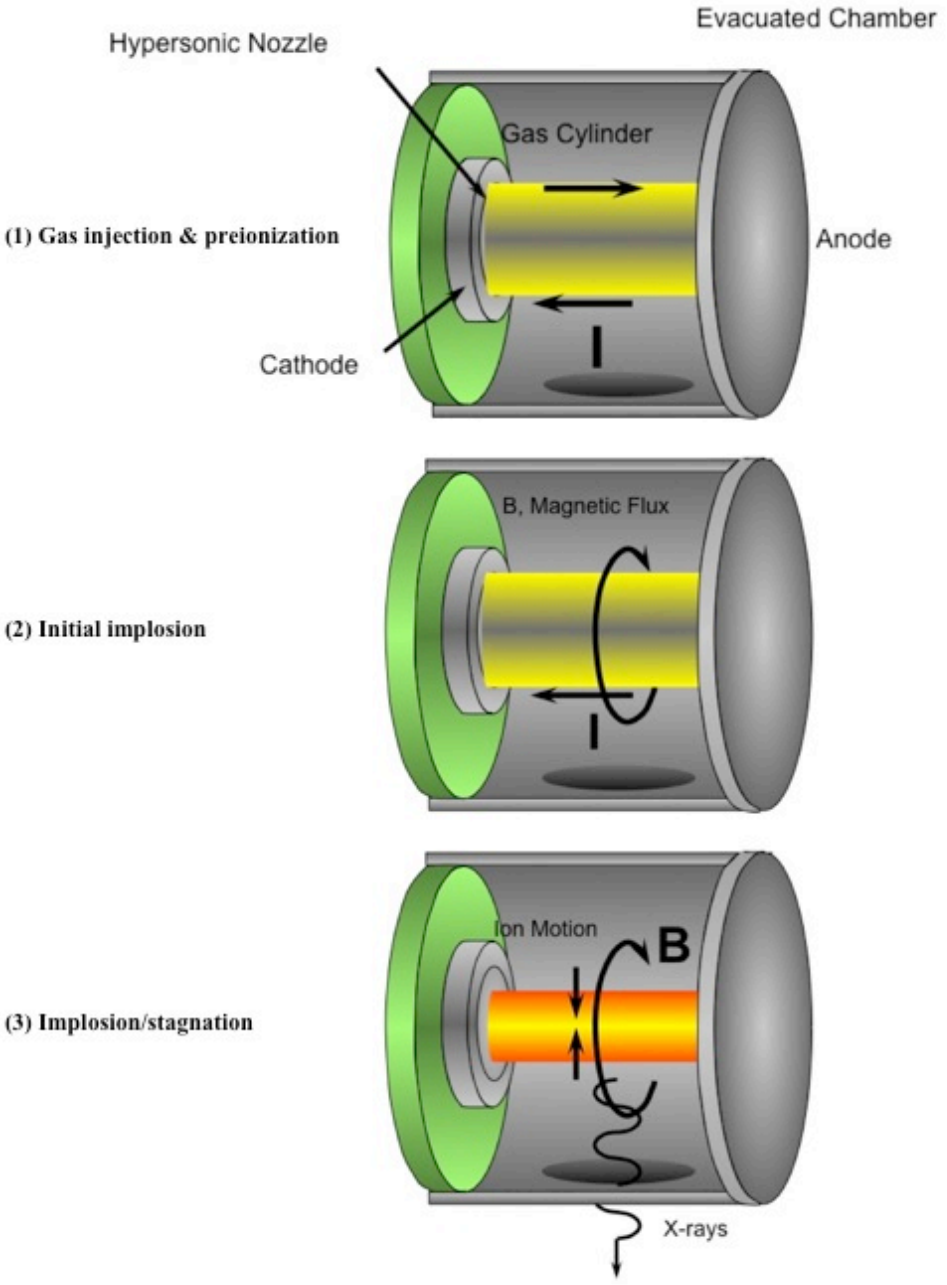

Figure 2.7: Stages of z-pinch formation [6].

magnetic pressure force balances against the internal gas pressure of the pinch. This pressure balance is derived from the momentum equation, and can be expressed as

$$\nabla p = \nabla(p_e + p_i) = j \times B. \tag{2.20}$$

For an axisymmetric pinch, this equation reduces to

$$\frac{\partial p}{\partial r} = -j_z B_\theta. \tag{2.21}$$

From Ampere's law,

$$\nabla \times B = \mu_0 j \Rightarrow \frac{1}{r}\frac{\partial}{\partial r}(rB_\theta) = \mu_0 j_z. \tag{2.22}$$

Integrating this gives

$$B_\theta = \frac{\mu_0}{r}\int_0^r j_z r dr. \tag{2.23}$$

Substituting Equation 2.23 into Equation 2.21 yields

$$\frac{\partial p}{\partial r} = -\mu_0 \frac{j_z}{r}\int_0^r j_z r dr. \tag{2.24}$$

Introducing the ion line density, N_i,

$$N_i = \int_0^a 2\pi n_i r dr \tag{2.25}$$

with units of m^{-1} such that $n = N_i/\pi a^2$, letting T_e and T_i be the mean electron and ion temperatures, and multiplying both sides of Equation 2.24 by $k_B(ZT_e + T_i)$, then

$$N_i k_B(ZT_e + T_i) = \int_0^a 2\pi p r dr \tag{2.26}$$

where the ideal gas law is assumed (i.e. $p = nk_B(ZT_e + T_i)$). Integrating Equation 2.26 by parts leads to

$$8\pi k_B N_i(ZT_e + T_i) = \mu_0 I^2 \tag{2.27}$$

or, assuming uniform density in the pinch,

$$n_i k_B(ZT_e + T_i) = \frac{\mu_0 I^2}{8\pi^2 a^2} \tag{2.28}$$

where

$$I = \int_0^a 2\pi j_z r dr. \tag{2.29}$$

Equation 2.28 is the well-known Bennett condition describing steady-state equilibrium that is valid for any profile of pressure, $p(r)$, and current, $I(r)$. The current density may be approximated by

$$j = A(\frac{r}{a})^n \tag{2.30}$$

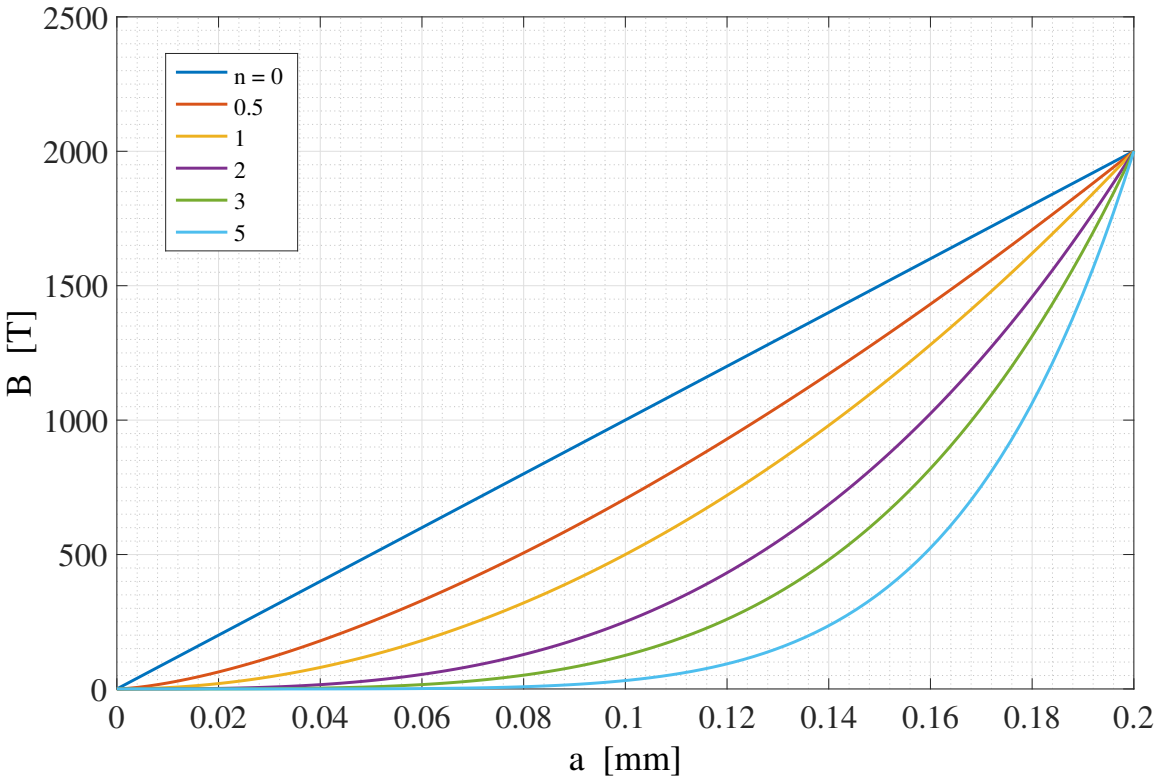

Figure 2.8: Magnetic field strength for a z-pinch with radius $a = 0.2$ mm, length 2 cm, and density $n_i = 2.9952 \times 10^{27}$ m^{-3}.

where a is the pinch radius, and A is a constant. n can take a value between 0 (constant, uniform current) and 5. If the total current I is known and a value for n is assumed, A can be determined by

$$A = \frac{1}{\int_0^a (r/a)^n \pi r dr}. \tag{2.31}$$

By using these expressions for the current density in Equation 2.23 and assuming a current of 1 MA, a pinch of radius $a = 0.2$ mm, length 2 cm, and density $n_i = 2.9952 \times 10^{27}$ m^{-3} can be expected to have a field strength of 2000 Tesla (Figure 2.8).

2.4.1 The Rayleigh-Taylor Instability and Beam-Target Fusion

One of the most infamous problems causing frequent head-scratching in the fusion community is the inherent inability of forming a confined plasma system that is completely homogeneous and without malformations deleterious to its yield. The requirement of homogeneity as a prerequisite for achieving a net positive energy output from the plasma is, from an engineering perspective, impractical; it is also a hindrance to success in the development of viable fusion systems. The immense difficulty of achieving symmetry in fusion target implosions without excessive perturbations in the process begs the question of whether or not there is a better way to approach the issue. In other words, is it possible to circumvent these instabilities or even utilize them to somehow enhance fusion reactivity in the plasma? As noted in Chapter 1, the objectives of this study are framed within the context of this question and the possibility of designing high density z-pinch plasma configurations that can enhance and utilize Rayleigh-Taylor (RT) instabilities to increase their fusion reaction rate density. An example of this is the possible applicability of the kappa distribution to hot plasmas, accounting for increases in higher energy particles (in the tail of the distribution function; see Figure 2.9 (extracted from [47]) illustrating this for hotspots in an imploded z-pinch plasma) due to beam-target interactions. The corresponding increase in population density of high energy particles is possibly a mechanism for launching burn waves in a compressed plasma.

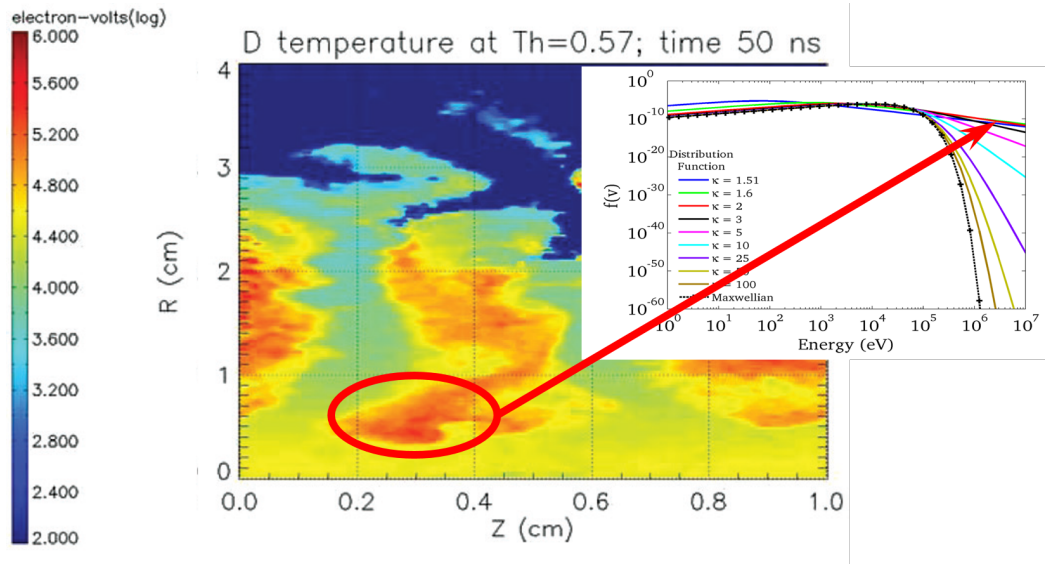

Figure 2.9: 2-D simulation [47] showing hotspot formation in a z-pinch due to RTI. The particle distributions in the hot regions may change from Maxwellian to a non-equilibrium distribution like the kappa distribution shown here.

2.4.1.1 Review of Rayleigh-Taylor Instabilities in Z-pinches

One of the principal challenges in utilizing these devices as neutron sources or for energy production is the observation that neutron yields scale as high as I^{10} for low power (< 10 MA) devices [48,49] with neutron spectra indicating beam-target fusion. At higher current, yields are $\sim I^{3.5}$ [47,50] and are of a more thermonuclear origin. In spite of the significant scaling with current, the "low power mode" peaks at about 10^{12} neutrons per shot, showing that low power devices are dominated by different physics. Interestingly, yields by these devices are poorly matched by magnetohydrodynamic (MHD) modeling, and frequently exceed the predicted yield by orders of magnitude. Insights into the mechanisms which promote or limit the RT instability have been hampered by the inapplicability of ideal MHD theory over most of the parameter

space [51] and the lack of computational resources until very recently (see, e.g. [49]) to conduct 3D kinetic modeling.

The high yields achieved in low power mode are caused by rapid acceleration of charged particles in the presence of strong field gradients. There remain numerous open questions: Why do some of the particles achieve energies greatly exceeding the potential drop in the pinch? What physics causes the change in dominance from beam-target to thermonuclear? What are the limits of the beam-target neutron sources, and can the RT modes be controlled and exploited to optimize yields? It is possible that in many cases the particle energy distribution is a consequence of nonequilibrium plasma produced by the rapid changes in field and plasma properties. From statistical mechanical arguments, there is a finite probability of particles reaching higher energies, with that probability increasing the farther the plasma is out of equilibrium.

2.4.1.2 Beam-Target Neutron Yield

Anderson *et al.* [52] provided some of the first published evidence that neutron production in a pulsed z-pinch with deuterium gas puffs is the result of a disruption in the current caused by the RT instability and is of beam-target rather than thermonuclear origin. Evidence for the nonthermal source was due to the observed neutron energy containing an additional 50 keV directed kinetic energy in the direction of the conduction current, consistent with beam-target generated fusion reactions. The theoretical discussion attributes the beam-target acceleration mechanism to the $m = 0$ sausage type RT instability mode, in which a rapidly changing inductance due to

the perturbation growth in the pinch produces a 50 to 100 keV beam of deuterons. This hypothesis was consistent with the theoretical work performed by Kruskal and Schwarzchild in 1954 [53] as well as Kurchatov in 1957 [54].

Recent analytical estimations for neutron yield on repetitive (1kHz) micro-x-pinches of DT and DD gas puffs have shown a 50 Joule pulse could produce 10^3 to 10^5 neutrons per pulse [55]. The neutron production relies on the late time disruption of the pinch by the onset of the RT instability. A summary of other x-pinch, z-pinch, and dense plasma focus devices from the open literature is review by Derzon *et al.* [55] to facilitate the scaling. The potential advantages of this approach include the long life and compact size of the neutron source.

The majority of dense plasma focus (DPF) experiments on neutron scaling have been performed with deuterium gas, where the scaling has been empirically determined to vary as I^4 [56]. While the results may vary significantly at a given pinch current, some general observations can be made. First, the variability can be largely attributed to the ratio of the rate of current rise induced by the back emf caused during the onset of RTI to the initial rate of current rise generated by the circuit [56]. Second, the prevailing thinking concerning the I^4 growth is that it is limited by the peak density achieved during the pinch. The onset and nature of RTI, along with the peak density, to some degree can be controlled by the geometry of the anode [57]. Finally, some recent results suggest that doping the deuterium gas with a small (1 to 18%) molar mixture of a high Z noble gas such as Argon can increase the yield by up to a factor of 8 [58, 59].

2.4.1.3 Rayleigh Taylor Instability Theory

Atchison and Lemons [60] studied the stability properties of a slab of current carrying cold fluid under acceleration by the $j \times B$ forcewhen this force is non-uniform in the slab. The RTI growth rate was found to increase (decrease) when the non-uniform force squeezes (stretches) the slab during acceleration. It was also found that the magnetic RTI growth rate γ in the linear regime is given by

$$\gamma^2 = kg_0 + \frac{g_0'}{2} \tag{2.32}$$

where k is the wave number, g_0 is the bulk acceleration of the slab, and g_0' is the local acceleration of the vaccum field/conducting fluid boundary. When $g_0' < 0$, this decreases the rate of growth. In the limit of g_0' becoming small, this expression recovers the gasdynamic RTI expression.

The Magneto-Rayleigh Taylor (MRT) instability mode limits the maximum initial radius of the wires. Hamann *et al.* [61] showed that the magnetic skin depth Δ is the essential scale length of importance for MRT growth, which must not exceed the plasma shell thickness prior to implosion. Thus Δ is connected to the implosion time. They developed an inequality:

$$R_0 \leq 2[\text{cm}]\sqrt{\frac{\tau}{100[\text{ns}]}} \tag{2.33}$$

where R_0 is the maximum recommended wire radius and τ is the implosion time in nanoseconds.

A series of subscale (1-2 kA, 20 kV, 500 ns) discharges were performed with 7.5 to 50 micron single wires of aluminum (Al), gold (Ag), tungsten (W), and copper (Cu) [62]. These experiments simulate the early time ablation of multiple wire array z-pinches on larger machines. Caterpillar-like striations were observed on the wires consistent with RTI at late stages of the pulse. Perturbations such as these grow nonlinearly in time leading to the formation of magnetic bubbles which penetrate the current sheet and arrive faster on axis compared with the main discharge [63]. The presence of these bubbles helps explain the higher than expected resistivity of the pinch during stagnation [64]. Magnetic field energy stored in the bubbles may be released during this time, explaining the heating of the plasma at the axis beyond what could be expected from conversion of kinetic to thermal energy.

CHAPTER 3

STOPPING POWER IN FUSION PLASMAS

3.1 Introduction

This chapter is derived from work recently published in Nuclear Fusion as part of this dissertation work, Reference [65]. The theory of stopping power in hot, dense plasmas is a prominent area of interest in fusion physics [13, 15–17, 66, 67]. Past studies have involved the stopping power in plasmas composed of fuels such as DT [15] and even DT mixed with uranium (U) [68]. The continual improvement in the accuracy of stopping power models in the last decade provides great insight into particle flow models such as electron and thermal conductivity, temperature relaxation and diffusion [17]. It has also complemented efforts in inertial confinement fusion (ICF) [13, 15, 16, 66, 69, 70], studies of charged particle deposition in thermonuclear fuels [15, 69], and development of more advanced target designs.

Recently, Grabowski *et al.* compared theoretical models of charged particle stopping, representing three major classes of kinetic theory, with nonrelativistic molecular dynamics (MD) simulations [17]. The kinetic theories studied were organized in three different classes:

1. The Lenard-Balescu class, representing weak scattering in a dense environment,

2. The Boltzmann class, representing strong scattering in a dilute environment, and

3. Convergent kinetic theories, which bridge the gap between the previous two classes.

The models are examined over a large parameter space of the plasma intratarget coupling parameter,

$$\Gamma_{ij} = \frac{1}{4\pi\epsilon_0}\frac{Z_i Z_j e^2}{r_0 k_B T} \tag{3.1}$$

for species i and j, and the projectile-target coupling parameter,

$$g = \sqrt{3}|Z|\Gamma^{3/2} = \frac{Ze^2}{\lambda_D k_B T} \tag{3.2}$$

where $r_0 = (4\pi n/3)^{-1/3}$ is the Wigner-Seitz radius, and $\lambda_D = (\epsilon_0 k_B T/e^2 n)^{1/2}$ is the Debye length.

Further, the authors extend the models in their study to better describe nonlinear effects and collective phenomena, introducing a new formulation for stopping power based on their MD simulations. The new method is shown to be accurate over a larger parameter space than state-of-the-art models such as Brown, Preston, and Singleton (BPS) [16], and Li and Petrasso (LP) [13]. Based on the accuracy and parameter range considerations of Grabowski et al.'s model, it has been implemented in SPFMax, a 3D plasma code recently developed for magneto-inertial fusion research

at the University of Alabama in Huntsville (UAH) [33]. SPFMax is described further in Chapter 4.

In this chapter, SPFMax is utilized to study stopping power in lithium deuteride and deuterium targets using the most recent stopping power models as an extension beyond the typical DT and D^{3}He targets that are more frequently investigated (e.g. see Ref. [15, 68]). The charged particle species for the DD background include the products from the reactions

$$D + D \longrightarrow {}^3He + n \tag{3.3}$$

$$D + D \longrightarrow T + p \tag{3.4}$$

and the species for the D^{6}Li background are the charged particle products from

$$D + {}^6Li \longrightarrow \alpha + \alpha \tag{3.5}$$

$$D + {}^6Li \longrightarrow p + \alpha + T \tag{3.6}$$

$$D + {}^6Li \longrightarrow {}^7Be + n \tag{3.7}$$

including the products from the DD reactions listed above in Equation 3.3 and Equation 3.4. For the sake of simplicity, simple spherical geometries representative of well known ICF configurations are used here to understand the variation of particle stopping length with respect to temperature and density, providing insight into energy transfer and coupling between plasma species. Improved understanding of these de-

pendencies in D^6Li plasmas will enable further exploration of the influence of energy coupling on burn wave propagation, yield, and other target performance parameters.

The remainder of this chapter is organized as follows: Section 3.2 describes the stopping power model used in this study followed by description of results from the model in Section 3.3.

3.2 Description of the Model

For brevity, the equations for stopping power developed by Grabowski *et al.* are simply stated here, and the reader is referred to [17] for further details. The stopping power is plotted as $dE/dx = (d\tilde{E}/dx)(Z^2 q_e^2/\lambda_D^2)/(1+g)^{2/3}$, the velocity is normalized as $\tilde{v} = v/[v_{th}(1+g)^{1/3}]$, with g and λ_D defined above, and

$$\frac{d\tilde{E}}{dx} \approx -R(w)[G(w)ln(e^{1/2} + \frac{\alpha + w^2}{g_0}) + H(w)] \tag{3.8}$$

$$R(w) = \frac{[M_1 + bM_2(w)w^2](1+g)^{2/3}}{w^2(1+bw^2)} \tag{3.9}$$

$$M_1 = s\frac{\ln(1 + \alpha e^{-1/2}/[g(1+aZ^2 g)])}{\ln(1+\alpha e^{-1/2}/g_0)} \tag{3.10}$$

$$M_2(w) = \frac{1}{s^2}\frac{\ln(1+s^3 w^3/g)}{\ln(1+w^3/g_0)} \tag{3.11}$$

$$G(w) = erf(\frac{w}{\sqrt{2}}) - \sqrt{\frac{2}{\pi}} w e^{-w^2/2} \tag{3.12}$$

$$H(w) = \frac{w^4 lnw}{12 + w^4} - \frac{w^3}{3\sqrt{2\pi}} e^{-w^2/2} \tag{3.13}$$

where $\alpha = 4e^{-2\gamma}$, $\gamma = 0.577216$, $s = d(1+cg)^{1/3}$, $w = v/(v_{th}s)$, with fitting parameters $a = 1.04102 \times 10^{-5}$, $b = 0.183260$, $c = 0.116053$, $d = 0.824982$, and $g_0 = 2.03301 \times 10^{-3}$.

Equation 3.8 is a modification of Peter and Meyer-ter-Vehn's work in [71] with $g = g_0$, a modified Coulomb logarithm, and scaling parameters s, M_1, and M_2. In the low velocity limit this form matches the BPS model [16] for weak coupling, and matches the MD simulation results for strong coupling. The scaling parameter M_2 preserves the Bohr limit and the results at moderate velocities are fit using the parameters b, c, and d. To describe the ionic component of the stopping power, the screening length must be larger than the interparticle spacing. Equation 3.8 can be used to describe the electron component as long as the screening length and classical distance of closest approach both remain larger than the thermal de Broglie wavelength. To take into account the effect of dynamic screening, the screening length has been rescaled as

$$\lambda_D \rightarrow \lambda_D \sqrt{1 + (v/v_{th})^2 (1 + \Gamma^3)^{1/4}} \tag{3.14}$$

following the convention of [17].

3.2.1 Code Verification

The UAH code [72] now has the capability to simulate charged particle deposition using the MD model. Tests for accuracy have been performed by reproducing results given in [17]. For the same input conditions (Γ, Z), the model reproduces their results accurately with minimal variation. Figure 3.1 illustrates an example of this verification for conditions $\Gamma = 0.1$ and Z = -1, corresponding to the top left plot of figure 1 in [17]. The MD model data in the plot was extracted from Grabowski [17] using a plot digitizer. In follow-on work to this study, further calculations for verification of this model will be performed for common (e.g. DT) and advanced fuels at solid density and lower using experimental data from [73, 74] and [75].

3.2.2 Target Conditions

The target conditions have been chosen to cover a broad parameter space representing spark-ignited spherical ICF targets. "Spark" ignition (see Chapter 2) in the context of ICF refers to a compressed target with a portion of its core heated to ignition temperatures. Two parameters were varied: density and temperature, defining the initial state of the target. The temperatures are chosen to be 1, 5, and 10 keV, and the density is varied as 100 (n = 2.4041×10^{31} cm^{-3}), 500 (n = 1.2021×10^{32} cm^{-3}), and 1000 (n = 2.4041×10^{32} cm^{-3}) g/cm^3, resulting in nine distinct thermodynamic states studied for each of two background plasmas: pure deuterium (DD) and a 50/50 mixture of lithium deuteride (D^6Li) (Table 3.1). The charge states of the "projectiles" and the background plasmas are constant and represented by the

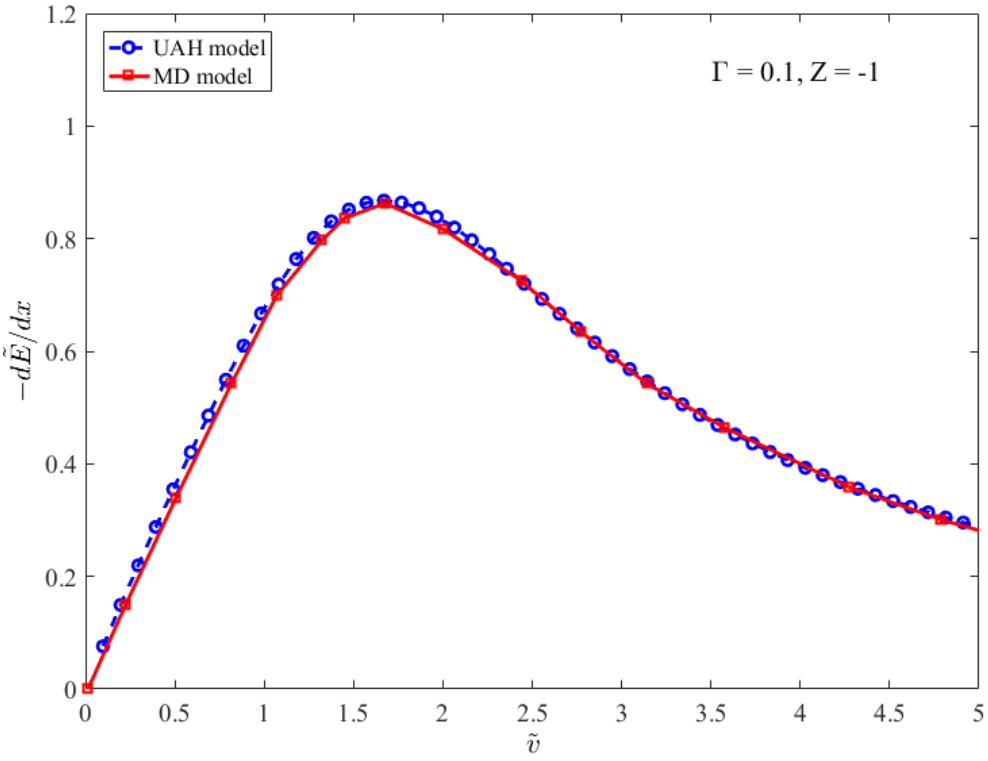

Figure 3.1: Code to code comparison of stopping power model in a one component plasma for conditions of $\Gamma = 0.1$, $Z = -1$ as a verification of the MD model implementation [17] in the present work.

coupling parameters in Equation 3.1 and Equation 3.2. Values of these parameters for each test case are given in Table 3.1, Table 3.2, and Table 3.3. The projectile particle velocities are set at their birth velocities. The radius of the spark region is held constant at 77 μm, a value extracted from the HIBALL target design study [69]. The values chosen for the spark radius, temperature and density have been selected to represent the extreme densities of hotspots in ICF targets (see, for example, Fraley et al. [20], Long and Tahir [15], and references therein) at "pre-ignition", ignition, and "post-ignition" temperatures. Collectively, these test cases give an overview of

Table 3.1: Target parameters corresponding to each test case.

Case	T [keV]	ρ [g/cm^3]	Γ_{DD}	Γ_{D^6Li}	$E_F[eV]$	Θ
1	1	100	0.0914	0.0978	301.11	3.3212
2	1	500	0.160	0.1443	880.451	1.1358
3	1	1000	0.2072	0.1210	1397.6	0.7155
4	5	100	0.0182	0.020	301.11	16.6059
5	5	500	0.0311	0.034	880.451	5.6791
6	5	1000	0.0393	0.0423	1397.6	3.5777
7	10	100	0.0091	0.010	301.11	33.2118
8	10	500	0.0155	0.0171	880.451	11.3583
9	10	1000	0.0195	0.0214	1397.6	7.1554

Table 3.2: Projectile-target coupling parameters (defined in Equation 3.2) corresponding to the DD reaction fusion product species for each test case.

	Case	T	p	^{3}He
	1	0.0479	0.0479	0.0957
	2	0.1109	0.1109	0.2218
	3	0.1633	0.1633	0.3266
	4	0.0042	0.0042	0.0085
g	5	0.0095	0.0095	0.0190
	6	0.0135	0.0135	0.0270
	7	0.0015	0.0015	0.0030
	8	0.0033	0.0033	0.0067
	9	0.0047	0.0047	0.0094

the parameter space for the purpose of examining the trends in the stopping power behavior while facilitating comparisons with DT and D^{3}He plasmas, which are more frequently characterized.

3.3 Results and Discussion

Figure 3.2 gives the stopping power versus range against a deuterium background plasma with density increasing from left to right and temperature increasing

Table 3.3: Projectile-target coupling parameters (defined in Equation 3.2) corresponding to the D^6Li reaction fusion product species for each test case.

	Case	α	^7Be	p_1	^7Li	T	p_2	^3He
g	1	0.106	0.212	0.053	0.159	0.053	0.053	0.106
	2	0.1899	0.3798	0.095	0.2849	0.095	0.095	0.1899
	3	0.1458	0.2916	0.0729	0.2187	0.0729	0.0729	0.1458
	4	0.0098	0.0196	0.0049	0.0147	0.0049	0.0049	0.0098
	5	0.0217	0.0433	0.0108	0.0325	0.0108	0.0108	0.0217
	6	0.0301	0.0603	0.0151	0.0452	0.0151	0.0151	0.0301
	7	0.0035	0.007	0.0017	0.0052	0.0017	0.0017	0.0035
	8	0.0077	0.0155	0.0039	0.0116	0.0039	0.0039	0.0077
	9	0.0109	0.0217	0.0054	0.0163	0.0054	0.0054	0.0109

from top to bottom. The vertical axis is in units of MeV/μm which gives numerical values of stopping power from 1 to 50 across the scope of the study. In each case, stopping power is seen to typically decrease with R as the charged particle loses energy to the background, with its deceleration dominated by the electrons. The ion stopping power overtakes the electrons as the charged particle velocity decreases, with a rapid increase as the particle approaches the average thermal velocity of the background ions. As a general rule, the range decreases linearly with density, varying from 1 μm down to 0.2 μm for the highest density. The range appears to be roughly linear with temperature, increasing by an order of magnitude as the temperature rises from 1 to 10 keV (Figure 3.2). For all cases in the DD plasma, the ^3He has the highest stopping power, followed by the proton and the triton. The values of stopping power for both the proton and triton tend to be approximately equal or within a few percent of each other. This is most likely due to their charge states being the same [71]. However,

observe that the triton has a shorter range than the proton, mainly due to its initial energy being $\sim 1/3$ that of the proton of the DD reaction.

Figure 3.3 shows the stopping power in a deuterium-lithium background plasma plotted in a manner similar to that of the DD plasma. In most cases the magnitude of the stopping power is similar to or greater than in the corresponding case in the deuterium background. The ranges of the DD reaction products (p,T,^{3}He) in the D^{6}Li plasma serve as a good basis of comparison to see any differences that may occur. It can be seen that the ranges of these products in the D^{6}Li plasma are comparable to those of the deuterium plasma. These observations are essentially valid as long as the temperature is not too low and the density too high. However, two cases for the D^{6}Li plasma stand out from the others due to their departure from the general trends observed so far. Cases 2 and 3, where T = 1 keV and ρ = 500, 1000 g/cm^3, show decreased stopping power and corresponding larger ranges for the DD reaction products. This departure is most conspicuous at the highest density, where the ranges of the charged particles actually increase beyond those at the lower density of 500 g/cm^3. It is also interesting to note that in case 3 the ranges of the DD reaction products increases by a factor of $\sim$4 in the D^{6}Li plasma. Table 3.4 shows that this increase is consistent for each of the DD products with a percent difference of $\sim$75%. Fraley et al. [20] observed this phenomenon in their study, noting that as the density, ρ, approaches 10^4 g/cm^3, there is a corresponding increase in the range, $\delta(\rho) = 1 \rightarrow 3$.

There are a few possible explanations that may account for the results of cases 2 and 3. As the plasma density increases to very large values ($n > 10^{26}$ cm^{-3}), the

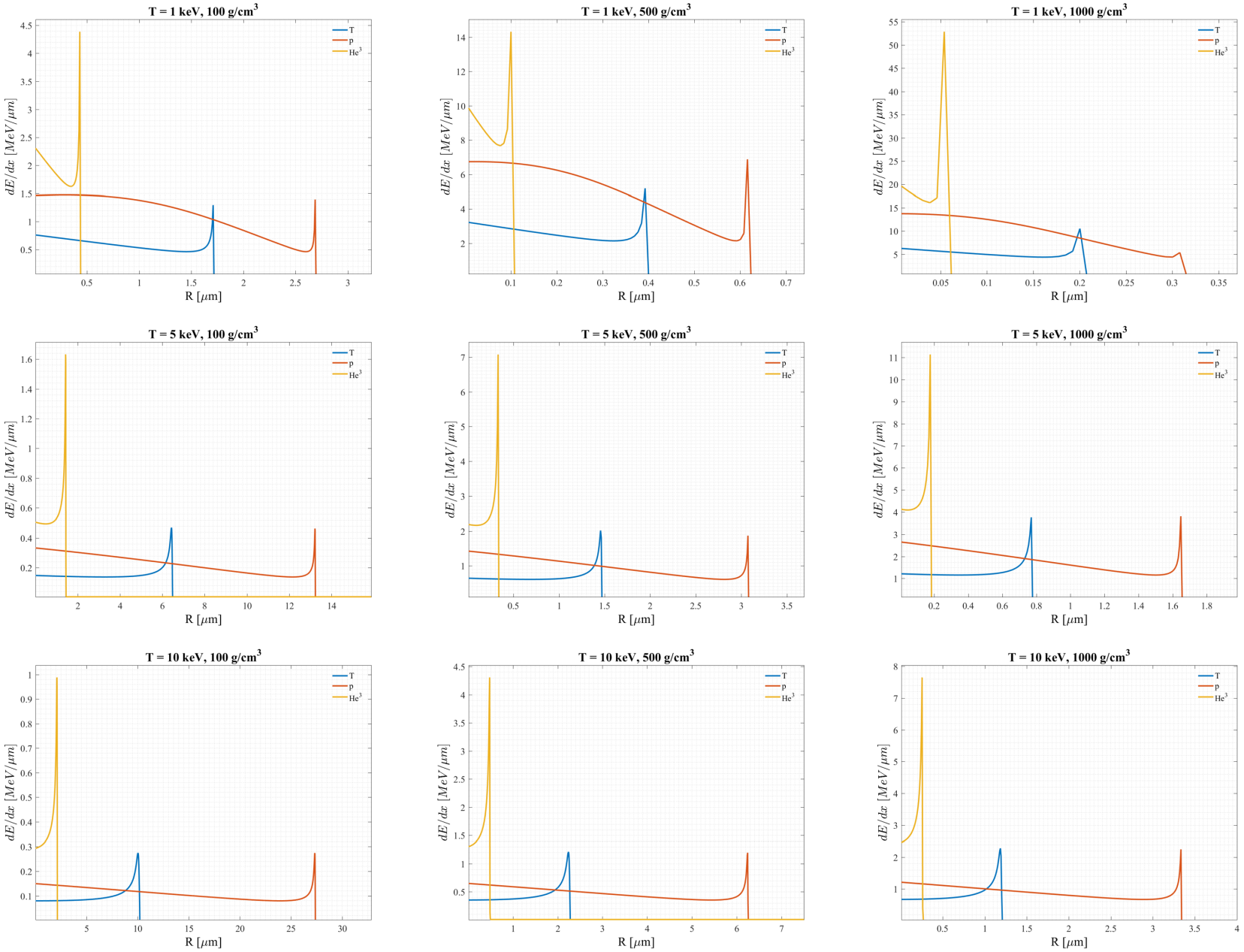

Figure 3.2: Stopping power of fusion products for deuterium plasma.

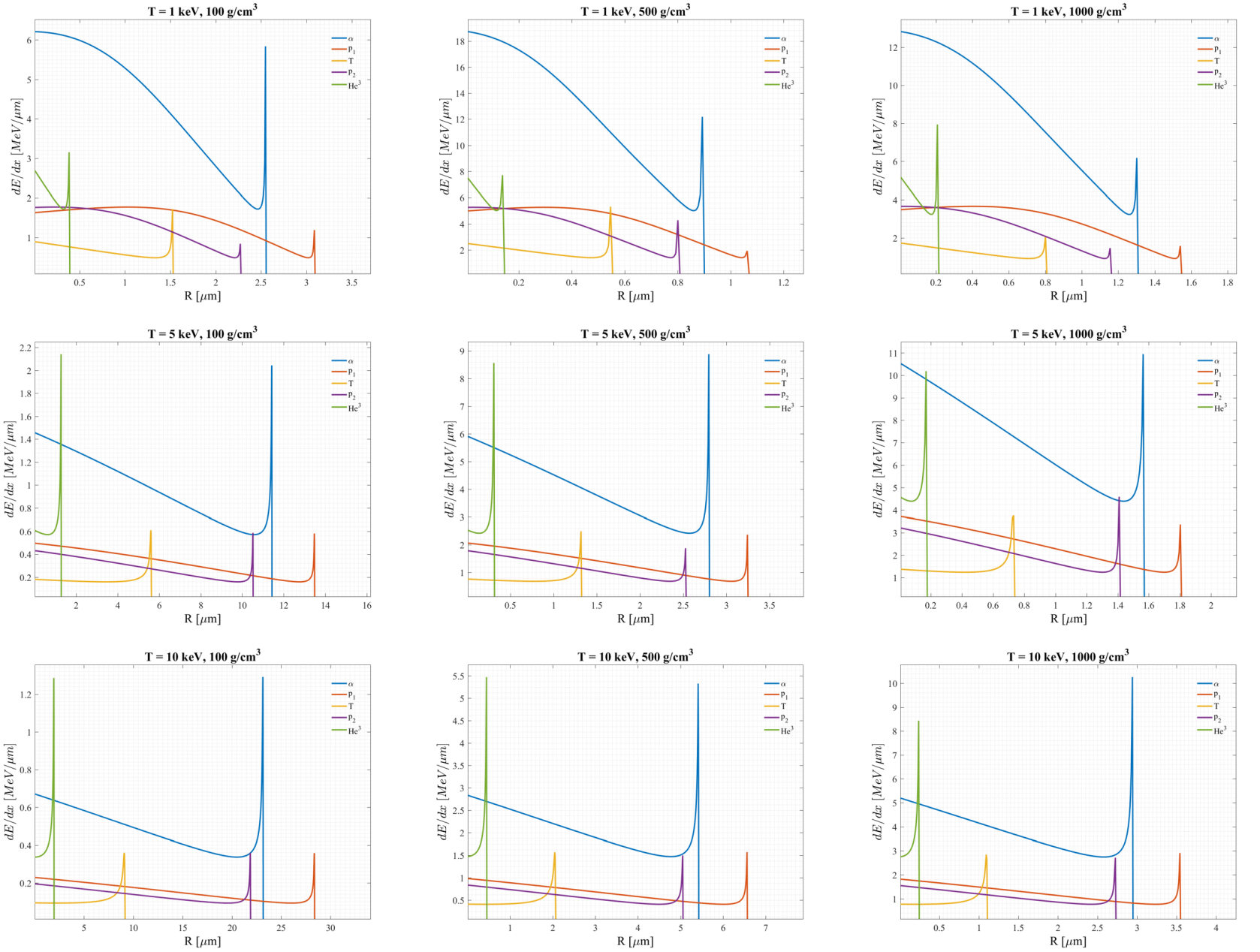

Figure 3.3: Stopping power of fusion products for D^{6}Li plasma.

intratarget coupling Γ (Equation 3.1) becomes stronger, increasing to $\sim$0.1 such that the plasma becomes weakly nonideal. It follows that the projectile-target coupling also increases. Additionally, in the high density limit, the plasma potential dominates the kinetic energy. When an ion moves through the plasma, it attracts electrons with its potential well, which screen out the ion's interaction (via the Coulomb potential) with other particles past a distance λ_D. Most of the Coulomb correlation is absorbed in collective oscillations in the plasma at its characteristic frequency, ω_p. However, in the high density limit these collective oscillations will not be excited by the ion due to strong Landau damping. This damping of collective modes occurs because the phase velocity of the potential wake following the ion is equal to the ion's velocity, v_p, which falls in the range $v_{th,i} \leq v_p \leq v_{th,e}$. This means the electrons in the plasma have more time to interact with the ion such that they do not drag behind it. Collective modes are induced by perturbations with phase velocities $v_{ph} \gg v_{th,e}$, and they are damped via the resonance interaction of electrons traveling with the wave. Since the phase velocity of the ion "disturbance" is not larger than the average electron thermal velocity, the effective friction drag force applied to the ion by the electrons lagging behind it does not occur. The absence of this additional mechanism of energy dissipation is a possible cause of the reduced stopping power values seen in case 3 where the density is high ($\rho = 1000$ g/cm^3) and the temperature is low (T = 1 keV).

In addition to the lack of collective modes in the plasma, at high densities and low temperatures the plasma becomes degenerate so that quantum effects come into play. One way of looking at this is by considering the quantum nature of electrons. Due to the uncertainty principle, one cannot localize electrons to any size smaller

Table 3.4: Approximate range (in μm) of projectile ions in D^6Li and DD backgrounds for T = 1 keV and $\rho = 1000$ g/cm^3.

	D^6Li	DD	% *Diff.*
T	0.8	0.2	75
p_{DD}	1.15	0.31	73
^{3}He	0.2	0.05	75
α	1.3	-	-
p_{D^6Li}	1.55	-	-

than their corresponding de Broglie wavelength, $\hbar/p$. In other words, instead of treating them as point particles, they have to be considered as a sort of "cloud" so that the integration over the impact parameter of the electron has to be cut off when it comes closer than the size of this cloud to another particle. Effects such as this are accounted for in the MD model through the utilization of velocity-scaled screening lengths and statistical potentials [17, 76]. The effects of quantum diffraction and dynamic screening are also discussed in [77]. At 1000 g/cm^3, the Fermi energy of the D^6Li plasma is

$$E_F = \frac{\hbar^2}{2m_e}(3\pi^2 n_e)^{2/3} \approx 1.398 \text{ keV} \tag{3.15}$$

implying the degenerate state of the plasma at 1 keV in contrast to the higher temperatures of 5 or 10 keV (this can be seen in the factor $\Theta = k_B T_e/E_F$ calculated for each case in table Table 3.1). It is then conceivable that the degeneracy effects play some role in the increasing range of ions in high density D^6Li plasmas.

CHAPTER 4

NUMERICAL METHODS

4.1 Smooth Particle Hydrodynamics

The state of the art of multidimensional modeling in the MIF physics regime includes the 3-D Rad-Hydro Code HYDRA [78], the MACH family of codes [79], the 2-D axisymmetric MHD code LASNEX [80], and state-of-the-art particle-in-cell (PIC) codes like LSP [81]. These codes are not a complete list, but are representative of the state of the art in computational modeling of the most prominent and active fusion experiments. There are two main reasons for developing an in-house capability with SPFMax. First, the codes available do not support nonlocal deposition of fusion products. There are hydrocodes available, including LASNEX and HYDRA, with this capability, but those packages are classified and not well documented. The method these codes use is typically based on flux-limited transport [82], but the details of the method specific to deposition are not published in peer reviewed journals. The second reason for developing this in-house capability is because most three dimensional (3D) simulation tools require a massively parallel cluster in order to produce useful results. Current experience in the UAH fusion research group [33, 72] has shown the utility

of producing a numerical tool that can study the burn physics problem and other relevant inertial fusion problems with a code that can be run on a high-end laptop.

In developing SPFMax, the goal was to develop a new three dimensional code to support research in MIF (see for example [6] and [83]) with the related objective of making it reasonably accurate with the ability to run on a laptop, facilitating a quick turn-around time for running simulations. The physics required to model a fusion plasma include tabular equations of state to model variable levels of ionization, thermal conduction, radiation emission and absorption, shock capturing, real viscosity, electromagnetic field propagation and forces in the plasma, a self-consistent circuit model, and nonlocal absorption of fusion ion product energy. The code also needs to resolve vacuum/plasma interfaces and nonlocal transport of charged particle deposition, heat transfer, radiation, shock capturing, and viscosity. The Smooth Particle Hydrodynamics with Maxwell equation solver (SPFMax) was developed to accomplish this.

4.2 The SPFMax Numerical Model

At the very core of this code is the smooth particle hydrodynamic (SPH) method [84], in which properties are approximated with the integral or kernel approximation according to

$$A_a(r) = \int A(r')W(r - r', h)dr' \tag{4.1}$$

where A is any property (like temperature or pressure), subscript a refers to point a, r is the position of point a in space, and W is the interpolating kernel function. In the limit that $h \to 0$, W becomes a delta function and the expression becomes exact. Any function can be approximated in this way, and this is the first assumption of SPH. The second assumption is to replace the integral with a summation:

$$A_a = \sum_b A_b V_b W_{ab}(r - r', h) \tag{4.2}$$

where V_b is the volume of the neighboring particles b. This is called the summation or particle approximation. This method is used because computers are finite and cannot solve the problem at every single point in space. The kernel function W is usually a Gaussian-like or cubic b-spline function which goes to zero at some κh, where $\kappa = 2$ normally. Gradients can be approximated as

$$\nabla A_a = \sum_b A_b V_b \nabla W_{ab}(r - r', h). \tag{4.3}$$

In SPFMax, the cubic spline function is used:

$$W_{ab} = \begin{cases} \frac{1}{4\pi h_{ab}^3}[(2-q)^3 - 4(1-q)^3], & 0 \le q \le 1 \\ \frac{1}{4\pi h_{ab}^3}(2-q)^2, & 1 \le q \le 2 \\ 0 & q > 2. \end{cases} \tag{4.4}$$

4.2.1 Finding the Compact Support Distance for Each Particle

The key to implementing any SPH method properly is to have an accurate list of neighbors for each particle and a compact support distance h which scales the kernel function and its gradients. This is done such that the following constraints are satisfied:

$$\sum_b V_b W_{ab} = 1 \tag{4.5}$$

and

$$\sum_b V_b \nabla W_{ab} = 0 \tag{4.6}$$

The particle volume is

$$V_a = \frac{h_a^3}{\eta^3} \tag{4.7}$$

and $\eta = 1.11$. It cannot be emphasized enough that if Equation 4.6 and Equation 4.7 are not satisfied, the code is not going to produce accurate results at all. In practice, it is very difficult to choose a compact support distance for each particle to satisfy this everywhere. In SPFMax, h is uniquely found for each particle to satisfy the first constraint, Equation 4.5, to within 1 %, and then the weights W_{ab} and ∇W_{ab} are scaled so that Equation 4.6 and Equation 4.7 are satisfied to within machine accuracy. For clarity, this procedure is described below.

First, particle position is tracked with

$$\frac{\partial r}{\partial t} = u. \tag{4.8}$$

Next, the particle neighbors have to be determined, and SPFMax uses the k-d tree to return the 60 nearest neighbors for each point in a script called ***update_neighbors.m***. The commands below are used:

```
p.NS = createns(pts);

[p.nbrs,p.r] = knnsearch(p.NS,pts,'K',60);
```

where `'pts'` stores the x, y, and z information, and the `nbrs` and Euclidean distances are stored in `'nbrs'` and `'r'`, respectively. To facilitate vector calculations, each particle has 60 neighbors so the `nbrs` matrix is a uniform, fixed block of memory. This is done even though ∼15 of the outer particles rarely contribute to the summation interpolant for computational speedup at the expense of memory. Once this has been done, h is first estimated to be half of the maximum distance between the particle and its neighbors. An iterative Newton-Raphson method is then used to improve the h estimate in the following manner. The particle volume is evaluated at $h + \delta h$ and $h - \delta h$, in which δh is $\sim h/0.01$. After this is done, the cubic spline kernel function is evaluated for $h + \delta h$ and $h - \delta h$. Equation 4.6 is then used to evaluate the particle consistency at the two values for h, and this is used to find the difference between the two summations. The value for h is then updated with

$$h_a = \frac{2\delta h_a}{(\sum_b VW_{ab})_{h_a+\delta h} - (\sum_b VW_{ab})_{h_a-\delta h}} sign[1 - \sum_b V_b W_{ab} \min(|1 - \sum_b V_b W_{ab}|, 0.25)] \tag{4.9}$$

This entire process is then repeated five times. The kernel weights (W_{ab}) are then scaled uniformly for the neighbors to force particle consistency, and this scaling changes the value of h by up to $\sim$1%. Once h is determined, the particle masses on the first time step should be determined to be consistent with the initial density specified in the input file (calculation of density is described below). The linear consistency constraint can also be enforced exactly by scaling either all of the negative or positive contributions to the summation of $V_b W_{ab}$ for each particle over its neighbors.

4.2.2 Governing Equations of Motion

SPFMax solves the single fluid equations of motion. Conservation of mass is given by

$$\frac{\partial \rho}{\partial t} + \nabla \cdot (\rho \mathbf{u}) = 0 \tag{4.10}$$

where ρ is the mass density in kg/m^3, $\mathbf{u}$ is the velocity vector, and t is time. SPFMax solves conservation of mass exactly because the continuity equation is not solved. Rather, density is determined by the particle mass divided by the particle volume, where the mass is a constant property of the particles. The density is computed from

$$\rho_a = \sum_b m_b W_b. \tag{4.11}$$

The momentum equation for a single fluid is given by

$$\frac{\partial u}{\partial t} = -\frac{1}{\rho}\nabla p + \nabla \cdot \tau + \frac{1}{\rho} j \times B \tag{4.12}$$

where p is the static pressure and τ is the deviatoric viscous stress tensor. The temperature is split between ions and electrons so that the energy equations are:

$$\frac{\partial e_i}{\partial t} = -\frac{p_i}{\rho}\nabla \cdot u + \frac{\tau}{\rho}\nabla \cdot u - \nabla \cdot (k_i \nabla T_i) + Q_{ei} \tag{4.13}$$

and

$$\frac{\partial e_e}{\partial t} = -\frac{p_e}{\rho}\nabla \cdot u - \nabla \cdot (k_e \nabla T_e) - 4\sigma T_e^4 \chi_{Planck} - Q_{ei} + \frac{\eta}{\rho} j^2 \tag{4.14}$$

where k is the thermal conductivity, σ is the Stefan-Boltzmann constant, T_i and T_e are ion and electron temperature, respectively, and χ_{Planck} is the single group Planck emission opacity. Alternatively, if the optical thickness $1/(\rho\chi_{Planck})$ is of the same order or smaller than the particle scale h, then radiation can be modeled as a diffusion process by adding an additional term to the overall thermal conductivity [85]

$$k_{total} = k + k_{Ross} = k + \frac{4acT_e^3}{3\rho\chi_{Ross}} \tag{4.15}$$

where $a = 4\sigma/c$ is the radiation density constant.

The rate of energy transfer between electrons and ions is

$$Q_{ei} = \frac{3m_e Zk}{m_i^2} \frac{(T_e - T_i)}{\tau_e} \tag{4.16}$$

and the electron collision time is [23]

$$\tau_e = \frac{3}{4\sqrt{2\pi}} \frac{m_i \sqrt{m_e}}{Z\rho} \frac{(kT_e)^{3/2}}{\lambda} \frac{(4\pi\epsilon_0)^2}{q^4} \tag{4.17}$$

where λ is the Coulomb logarithm.

4.2.3 Ray Tracing for Fast Ion, Beam Current, and EM Radiation Deposition

Nonlocal deposition of energy from radiation sources is a challenging problem. The philosophy behind SPFMax is to implement algorithms which capture the physics accurately while maintaining the ability to run full 3-D problems on a laptop or comparable desktop computer. The ray tracing algorithm implemented here is an attempt to handle nonlocal deposition with the ability to scale up as computers become more powerful. The basic approach is to specify a ray geometry and a type of source radiation (electromagnetic, fast ions from fusion or fission fragments, neutrons, or current), and the power of the radiation attenuates as it propagates through matter. There are exceptions to the attenuation, such as the specification of a current in a beam, which could be used to define a simple localized arc. Scattering is currently not modeled but will be implemented in the near future. The method assumes a single

pass of the radiation from the source along the center axis of the ray or branch (see next paragraph for definition of rays and branches).

Collectively, the term 'ray' means a beam (i.e. cylinder), axisymmetric cone, or 4π isotropic source of radiation in which the radiation/matter interaction occurs as illustrated in Figure 4.1. The intensity of the radiation source falls off as $1/r^2$ away from the source for the cone and 4π rays, but is collimated for the beam source. In any problem, the user is free to specify any number or combination of rays, although increasing the number and resolution of each ray will slow down the computation. The 4π rays are unique among the three ray options in that they are split into a number of 'branches' specified by the user so that anisotropic material properties may interact with an isotropic source, thus causing heating or other interactions away from the source to vary in any direction, down to the resolution of the branches. This 4π ray configuration is used for all simulations performed in this study.

The present physics options for rays include ohmic dissipation, electromagnetic radiation, and fusion or fission fragment ion deposition. The fusion ion deposition and radiation models are the ones used in this dissertation and are discussed below.

4.2.3.1 Bremsstrahlung Radiation Power

For electromagnetic radiation, if the Bremsstrahlung option is turned on, then the radiation power added to the energy equation is [24]

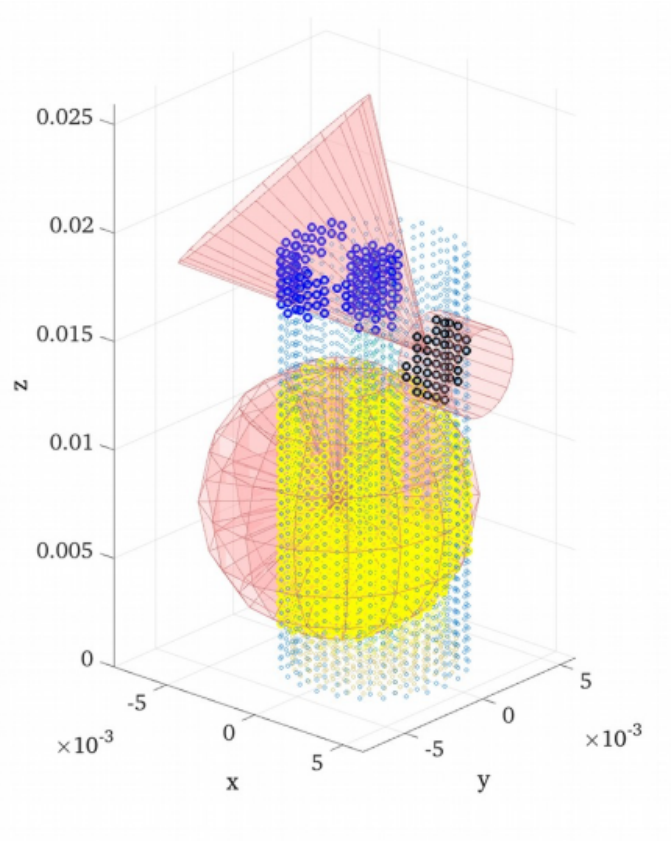

Figure 4.1: Options for ray tracing, showing a representative beam (cylinder), conical, and 4π (spherical) options. The black, blue, and yellow points are physical SPH particles residing in each of the beam, cone, and 4π rays that would interact with the radiation source.

$$(\frac{de}{dt})_{br} = \frac{-16\pi}{3\sqrt{6\pi}} \frac{q^6}{m_e^2 c^3 (4\pi\epsilon_0)^3} \frac{Z_i^2 n_e}{\sqrt{k_B T_e / m_e} M W_i m_a} \int_0^\infty 4\pi \exp \frac{-h\nu}{k_B T_e} d\nu \tag{4.18}$$

$$= \frac{-64\pi^2}{3\sqrt{6\pi}} \frac{q^6}{m_e^2 c^3 (4\pi\epsilon_0)^3} \sqrt{\frac{k_B T_e}{m_e}} \frac{Z_i^3 \rho}{(M W_i m_a)^2} \tag{4.19}$$

For spectrally dependent (i.e. multigroup) bremsstrahlung radiation,

$$(\frac{de}{dt})_{br_\nu} = \frac{-64\pi^2}{3\sqrt{6\pi}} \frac{q^6}{m_e^2 c^3 (4\pi\epsilon_0)^3} \sqrt{\frac{k_B T_e}{m_e}} \frac{Z_i^3 \rho}{(MW_i m_a)^2} (e^{-\frac{h\nu_{i+1}}{k_B T_e}} - e^{-\frac{h\nu_i}{k_B T_e}}). \tag{4.20}$$

The bremsstrahlung absorption coefficient works exactly like a mass attenuation coefficient:

$$\kappa_\nu = \frac{8\pi^2}{3\sqrt{6\pi}} \frac{q^6}{m_e^2 c^3 (4\pi\epsilon_0)^3} \frac{Z_i^3 \rho}{(MW_i m_a)^2 \nu^3} \sqrt{\frac{m_e}{k_B T_e}} = \frac{\mu}{\rho} \quad [\frac{\mathrm{m}^2}{\mathrm{kg}}]. \tag{4.21}$$

Finally, the bremsstrahlung power dropped in a ray segment is given as

$$P_{\nu,r} = P_{in,\nu,r}(1 - e^{-\kappa_\nu \rho \Delta r}) \tag{4.22}$$

where the power distributed in each ray segment is

$$P_{\nu,0r} = (\frac{de}{dt})_{br_\nu} \frac{\Omega_r}{4\pi} \tag{4.23}$$

and the solid angle subtended by the ray is

$$\Omega_r = \sin\phi d\phi d\theta \tag{4.24}$$

where ϕ is the angle from the z-axis (polar angle) and θ is the azimuthal angle measured counter-clockwise from the x-axis around the z-axis.

4.2.3.2 Fusion Ion Deposition Heating

The reactivity for a reaction of species i with species j is given by

$$\frac{dN}{dt} = \frac{n_{X_i} n_{X_j}}{1+\delta_{ij}} \langle \sigma v \rangle_{ij} V \tag{4.25}$$

where $\delta_{ij} = 1$ for $i = j$ and $\delta_{ij} = 0$ otherwise. The power per unit mass delivered to a particular fusion product species k is

$$(\frac{de}{dt})_k = \frac{n_{X_i} n_{X_j}}{\rho(1+\delta_{ij})} \langle \sigma v \rangle_{ij} E_k \tag{4.26}$$

where E_k is the initial kinetic energy of the fusion product species k. The total power of the system is then

$$P_{fus,k} = \sum_{a=1}^{N} \frac{n_{a,X_i} n_{a,X_j}}{(1+\delta_{ij})} \langle \sigma v \rangle_{a,ij} E_k V_a \tag{4.27}$$

where the sum is over all SPH particles. The fusion power dropped in a ray segment is then calculated starting with the fraction of power in a particular ray:

$$f_r = \frac{\Omega_r}{4\pi}. \tag{4.28}$$

The work done by a fast fusion ion traveling through a particular segment of i of a particular ray r is

$$\delta W_{ir} = (\frac{dE}{dr})_{ir} \Delta r_{ir} \tag{4.29}$$

where $(dE/dr)_{ir}$ is the function calculating the local stopping power (deceleration force) on the fast particles determined as a function of ion species, electron densities and temperatures. The local stopping power itself is a function of the kinetic energy of the fast ions moving through the ray segment, $\frac{1}{2}m_k v_{k,ir}^2$. It is assumed that the stopping power is constant through a ray segment so that the total change of kinetic energy of an ion in the segment is then

$$\frac{1}{2}m_k v_{k,ir}^2 - \frac{1}{2}m_k v_{k,i(r-1)}^2 = -\delta W_{ir} \tag{4.30}$$

The velocity of the ion is then

$$v_{k,ir} = \max[(v_{k,i(r-1)}^2 - \frac{2\delta W_{ir}}{m_k}), 0]. \tag{4.31}$$

Finally, the ion deposition power dropped in a ray segment is

$$P_{ion,0r} = (\frac{n_{X_i} n_{X_j}}{1+\delta_{ij}}\langle\sigma v\rangle_{ij} V)(\frac{\Omega_r}{4\pi})((\frac{dE}{dr})_{ir}\Delta r_{ir}). \tag{4.32}$$

The stopping power model used in this expression is the molecular dynamics model discussed in Chapter 3. Other examples in the literature include Harris and Miley [12], Long and Tahir [15], and Li and Petrasso [13].

4.3 Study Methodology

The burn simulations performed in this study focus on the ignition phase immediately following the compression of the target. This is an advantageous approach because:

1. Emphasizing the study focus on the physics of ignition without added complications of hotspot formation allows for a better understanding of the conditions a hotspot has to reach to achieve burn propagation and ignition in a target.

2. By first quantifying such requirements, one may narrow the parameter space describing the "type" of hotspot desired to achieve ignition, facilitating efficient study of the dynamics of hotspot creation.

3. Narrowing the aforementioned parameter space describing the ignition threshold of the hotspot further facilitates the development of methods to repeatably create the required hotspots in a fusion system configuration that will ignite and burn consistently.

4.3.1 Target Configuration

Following Linhart *et al.* in [86], the spark ignition configuration (Figure 4.2) is representative of the creation of a hotspot at full compression by the Rayleigh-Taylor instability (RTI). In this case the current flowing through the pinch is not constant. The disruptions formed by the RTI can cause large voltage gradients that accelerate plasma ions at very high energies, possibly igniting a burn wave in the fuel (see Section 5.2). Parameters used in the simulations are discussed in Chapter 5.

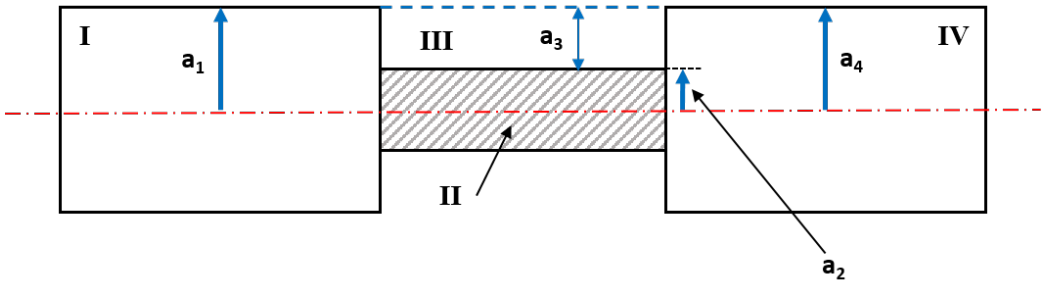

Figure 4.2: Basic geometry for "spark ignition" scenario. The basis for this geometry setup can be found in [86].

CHAPTER 5

SIMULATION RESULTS AND ANALYSIS

5.1 Introduction

This chapter begins with an examination of some simulation results obtained using SPFMax and how they compare with calculations made in a previous study by Linhart *et al.* [87]. Section 5.3 shows the results of the D^6Li study, followed by analysis and discussion in Section 5.4.

5.2 Verification Results

Two simulations performed by Linhart *et al.* [87] simulate a detonation propagating in a cylindrical DT plasma that serve as useful test cases to establish confidence in the results from SPFMax. The first verification test is a clear illustration of ignition in a z-pinch due to a "spark" region or hotspot. Results of this simulation are shown in figure 4 of [87] as a two dimensional contour plot of density, ρ, and temperature, T, as they evolve over time. Line plots of the density and temperature along the pinch axis in figure 4b of the same paper further illustrate the propagation of a burn wave as it travels along the pinch. Both of these plots are reproduced here in Figure 5.1 and Figure 5.2. Data for the second verification test is shown in Figure 5.5 (figure 6

of [87]). Initial conditions for this test are set so that the spark fizzles out without igniting the rest of the fuel in the pinch. Because of the challenging physics of burn wave calculations, there is no closed form analytical solution for meaningful parameters. See, for example, the discussion by Atzeni and Meyer-ter-Vehn [24], chapter 11. For this reason, any numerical simulation in the absence of experimental data is considered to be qualitative. The figure of merit in this numerical test is to confirm whether or not the SPFMax implementation of the Linhart *et al.* tests also produce a burn wave for Case 1 and a "fizzle" for Case 2. Parameters and initial conditions for these two verification test cases are listed in Table 5.1, and the results from SPFMax are shown in Figure 5.3 through Figure 5.7. One caveat to be mentioned here is for the ignition test case: in the SPFMax simulations, the initial temperature of the outer fuel of the pinch had to be set to 500 eV instead of 172 eV as in Linhart *et al.*. This problem was determined to be caused by uncertainty in reactivity and reaction rate calculations at relatively low (sub-keV) temperatures.

Table 5.1: Parameters and initial conditions for verification test cases extracted from Linhart et al. [87]

	Radius [μm]	Length [μm]	T_{spark} [keV]	T_{outer} [keV]	n_i [cm^{-3}]
Case 1	20	940	17.234	0.17234	7.003×10^{25}
Case 2	20	940	17.234	0.17234	1.401×10^{25}

In case 1, the results show a detonation wave that launches around $t \sim 4$ ps (Figure 5.1) [87]. Results for the same simulation in SPFMax are shown in Figure 5.3 and Figure 5.4. The data clearly shows a burn wave launching by ~ 10 ps, slightly

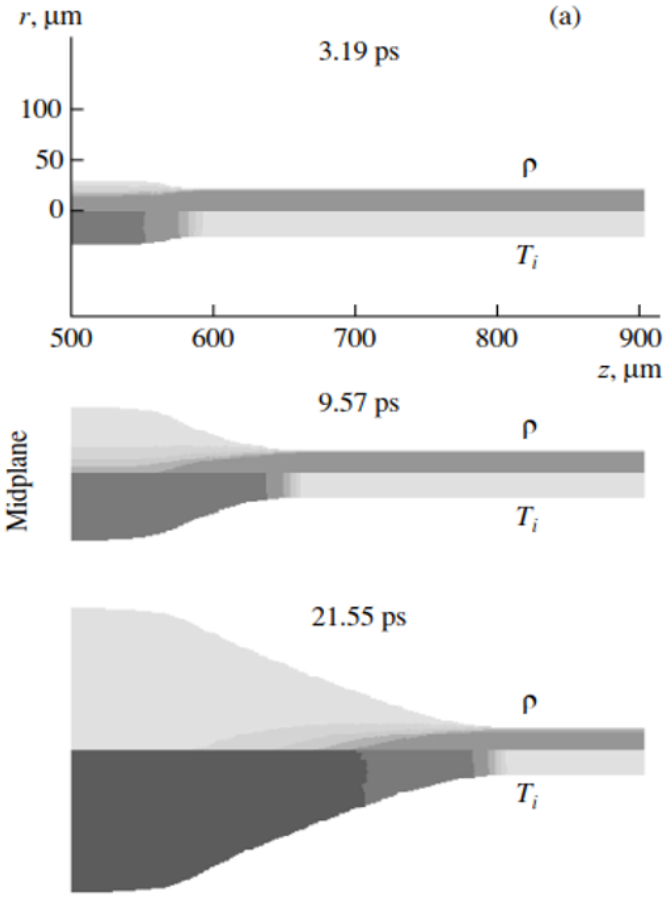

Figure 5.1: Figure 4a of reference [87] showing time sequences of ρ and T_i.

later than Linhart *et al.*'s results. There is a clear difference, however, in the propagation of the burn wave in Figure 5.3. One reason for this could be the difference between how Linhart *et al.*'s alpha particle diffusion model and the stopping power model used in SPFMax simulate alpha particle energy transport. The ranges of the alpha particles are likely shorter in the SPFMax simulations, which could cause the ion temperature to propagate along the pinch axis somewhat slower than it does in the Linhart *et al.* data. Examining the time evolution of the density along the pinch

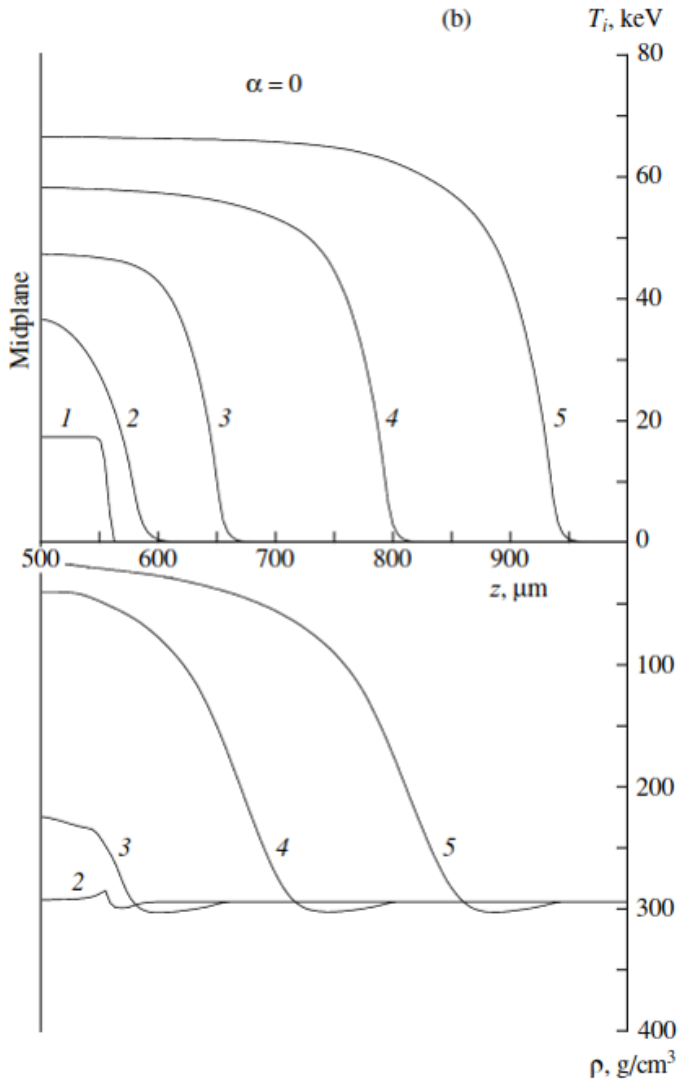

Figure 5.2: Figure 4b of reference [87] showing axial line plots of $\rho(z)$ and $T_i(z)$ at times (1) 0, (2) 3.2, (3) 9.6, (4) 21.5, and (5) 33 ps.

axis in Figure 5.4, the data is in good agreement with figure 4b in [87], which is reproduced here in Figure 5.2.

Case 2 shows the spark dying on a timescale similar to the data in Figure 5.5. This effect is reproduced in the results from SPFMax (Figure 5.6 and Figure 5.7). The differences in the SPFMax results are, as in Case 1, likely due to differences

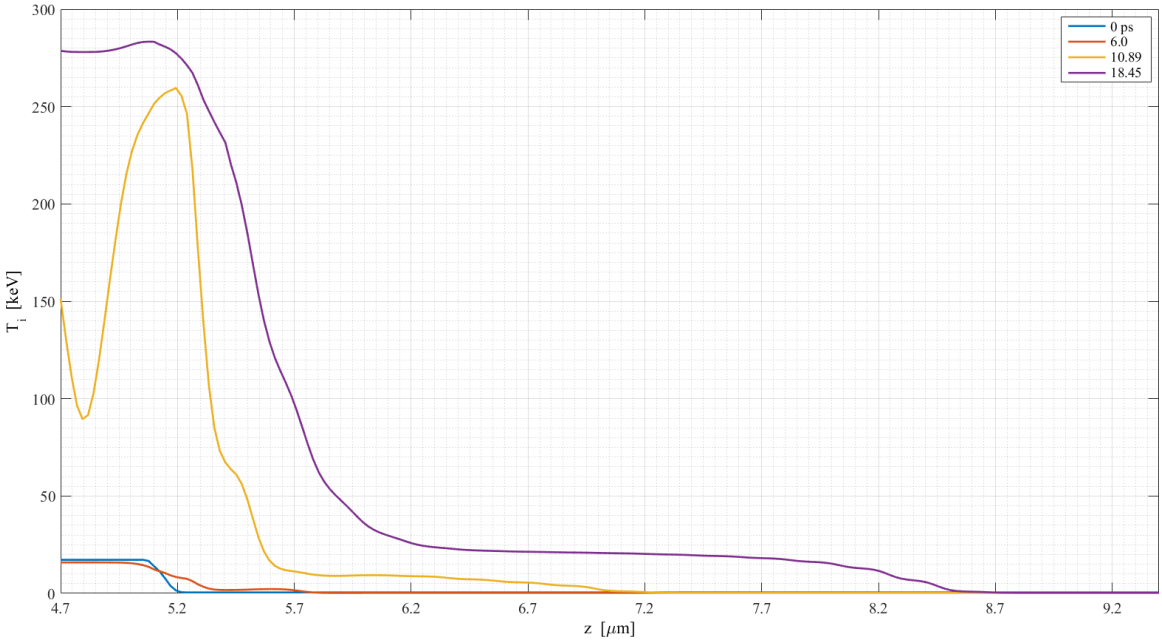

Figure 5.3: Burn wave propagation results in SPFMax for Case 1 showing time evolution of $T_i(z)$.

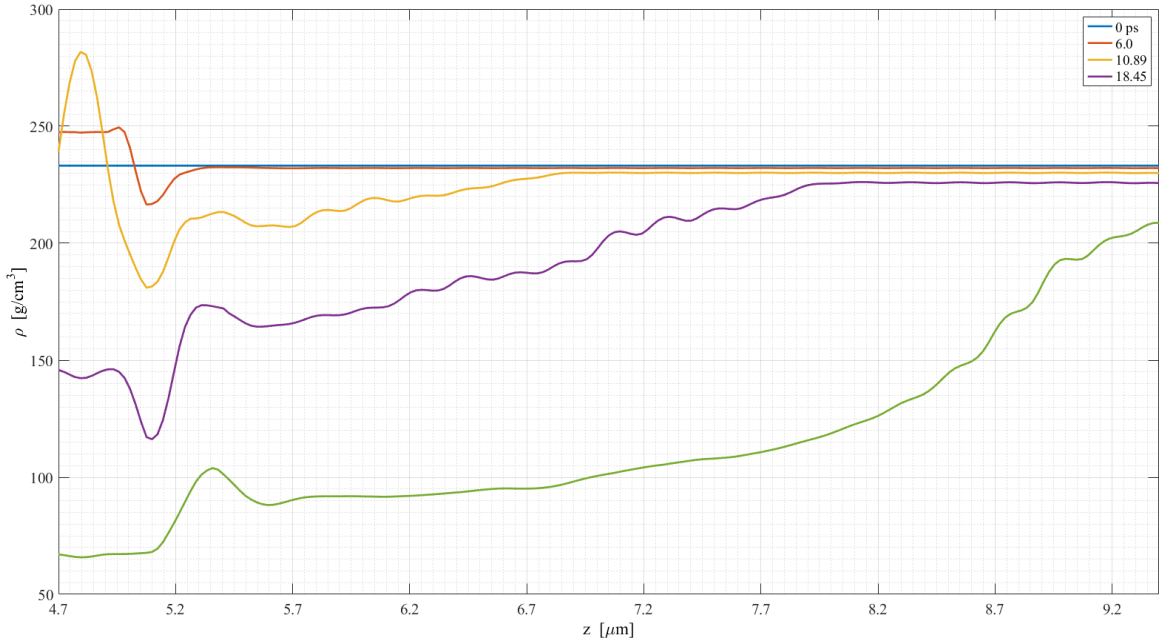

Figure 5.4: Burn wave propagation results in SPFMax for Linhart comparison Case 1 showing time evolution of $\rho(z)$.

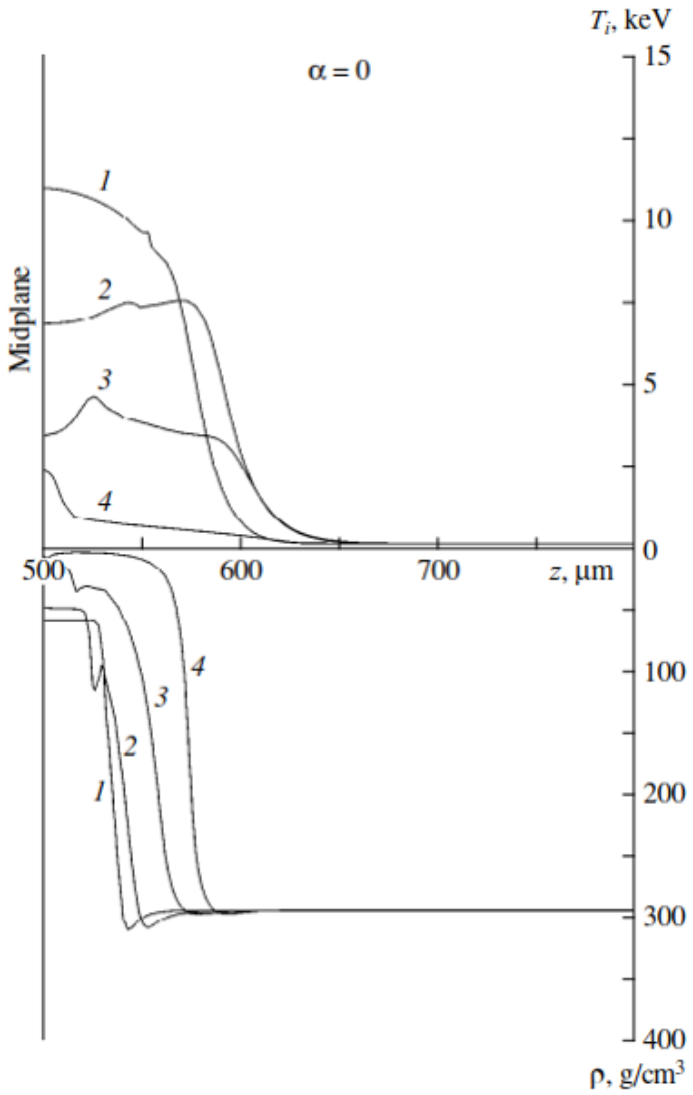

Figure 5.5: Figure 6 of reference [87] showing axial line plots of $\rho(z)$ and $T_i(z)$.

between Linhart *et al.*'s alpha deposition model and the SPFMax stopping power model. However, these differences are minor and overall the simulations are in good agreement with the data from [87].

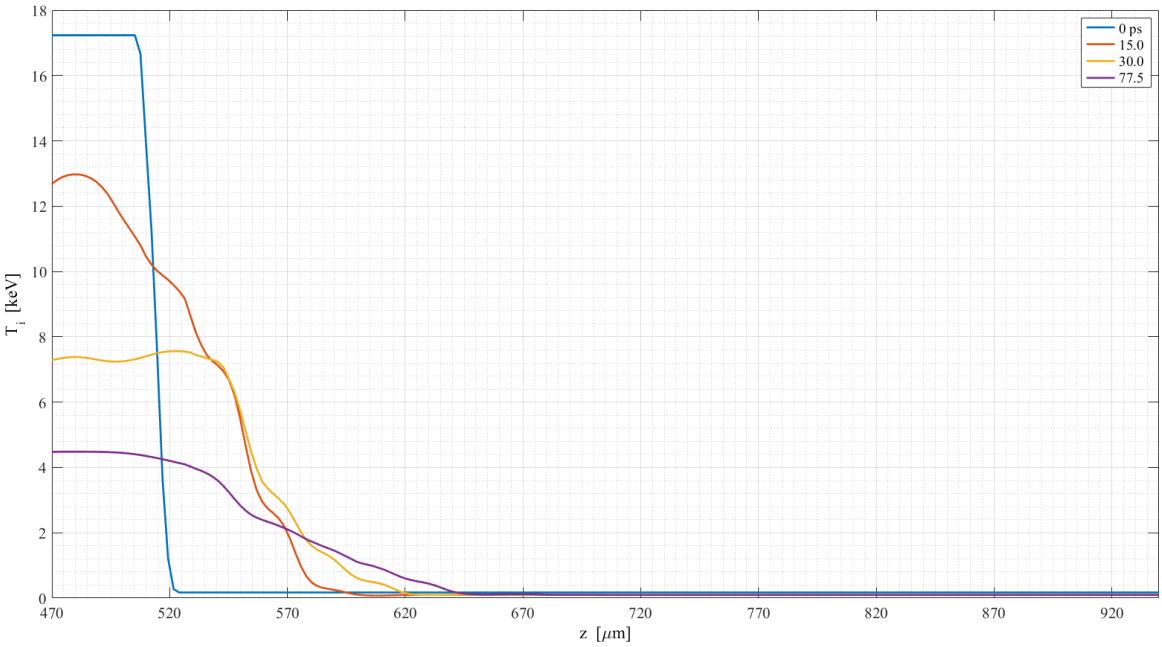

Figure 5.6: Burn wave propagation results in SPFMax for Linhart comparison Case 2 showing time evolution of $T_i(z)$.

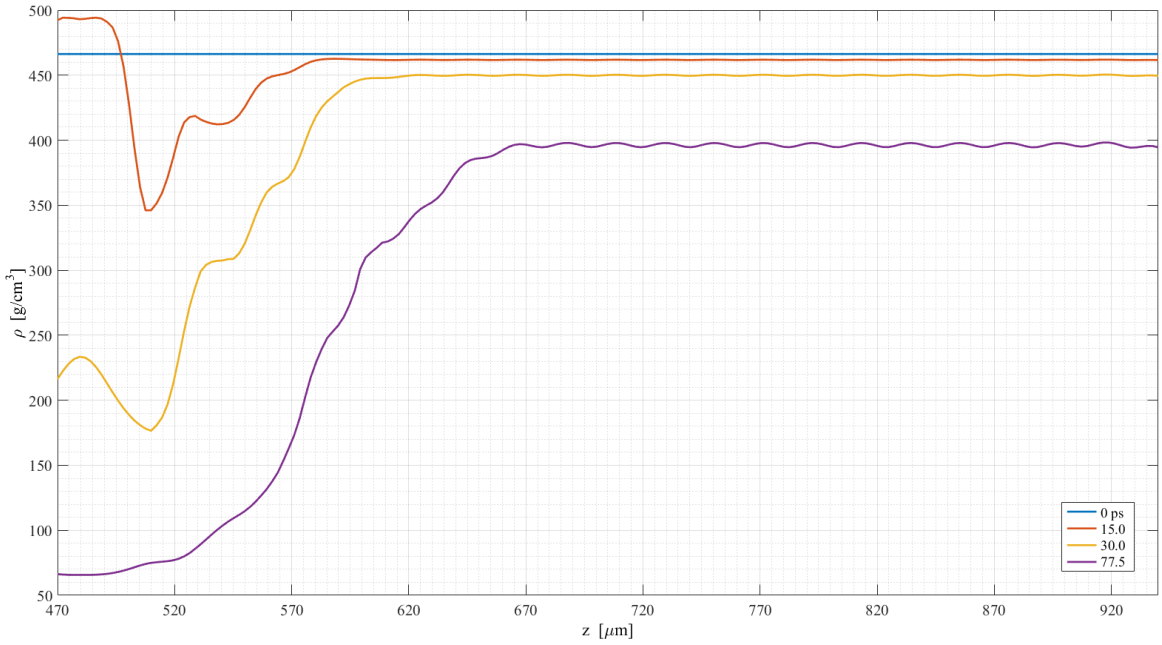

Figure 5.7: Burn wave propagation results in SPFMax for Linhart comparison Case 2 showing time evolution of $\rho(z)$.

5.3 D^6Li Simulation Results

Table 5.2 lists the initial parameters for the simulations using D^6Li fuel. Test cases 1 through 5 each demonstrate behaviors characteristic of the two primary scenarios of interest: (1) spark ignition, in which a burn wave launches in the plasma from a central hotspot, and (2) "batch burn", where the pinch burns some of the fuel without launching a burn wave. Test case 6 simulates an experimental scenario using the Charger-1 pulsed power facility at the University of Alabama in Huntsville. The initial temperature in the pinch is calculated by assuming the energy input from Charger-1 at 30% efficiency is directly deposited in a D^6Li wire. This scenario is discussed in Section 5.3.3. In all of these simulations the molar mixture of deuterium and lithium-6 is 50/50. Additionally, the size of the pinch and the hotspot remain constant in order to focus on the effects of changes in the thermodynamic state of the plasma. The configuration of the pinch is illustrated by Figure 4.2 in Chapter 4.

Section 5.3.1 through Section 5.3.3 illustrate the results of the six test cases, highlighting the characteristics of burn wave propagation (or lack thereof) in the pinch and general trends observable in the data. Section 5.3.1 demonstrates the temperature threshold in the hotspot above which a burn wave will ignite the pinch, followed by results showing the effects of the density ratio ρ_{spark}/ρ_{ext} on ignition and burn propagation in the pinch. The significance of these results and their implications are discussed in Section 5.4.

Table 5.2: Parameters and initial conditions for D^6Li test cases.

	Scenario	T_{spark} [keV]	ρ_{spark} [g/cm^3]	T_{ext} [keV]	ρ_{ext} [g/cm^3]
Case 1	Spark Ignition	40	1.5	1	2.5
Case 2	Batch Burn	35	1.5	1	2.5
Case 3	Spark Ignition	40	0.75	1	1.25
Case 4	Batch Burn	40	1.25	1	0.75
Case 5	Batch Burn	50	2.5	1	1.5
Case 6	Charger-1 Input	1.536	0.75	1.536	0.75

5.3.1 Spark Ignition Vs. Batch Burn

The first test case is designed to illustrate a z-pinch in which a burn wave clearly launches from a hotspot, igniting the plasma. For this reason, the densities are set at initial values higher than the density of solid D^6Li (see Table 5.2). The initial temperature of the hotspot was chosen to be near that required to ignite a deuterium plasma ($\sim$50 keV), but as low as possible to establish an approximate minimum point where a burn wave will still propagate through the plasma. This point was determined to be 40 keV.

Figure 5.8 shows the early time evolution of the pinch ion temperature along the z-axis from 2.5 mm (middle point) to the end of the pinch at 5 mm. After 30 ps the temperature in the hotspot rises quickly and the exterior portion of the pinch begins to heat by electron thermal conduction. At 50 ps a burn wave begins to form, heating more of the cold fuel. By the 70 ps mark, the wave has fully developed and begun to propagate outward from the hotspot. Figure 5.9 shows the time evolution of

the pinch ion temperature along the z-axis in 250 ps increments up to the end of the simulation at 2 ns. By the 238.84 ps mark, it is clear that the burn has propagated through the pinch and the fuel continues to burn. The ion temperature peaks at 160 keV in the center of the pinch within the first nanosecond, remaining at this temperature until the end of the simulation.

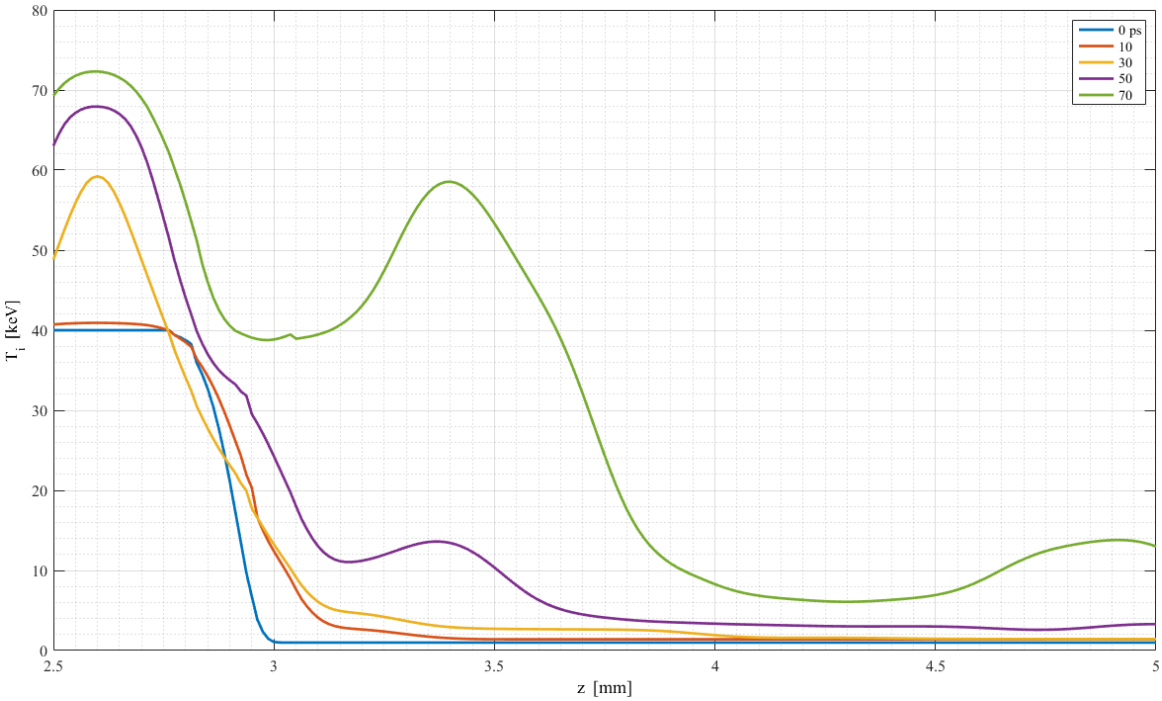

Figure 5.8: SPFMax results for a D^6Li pinch with initial hotspot temperature T = 40 keV and density ρ = 1.5 g/cm^3. The external portions of the pinch have initial temperature T = 1 keV and density 2.5 g/cm^3.

The fusion yield in the pinch for the first 250 picosends of the simulation is shown in Figure 5.10 to illustrate the initial stage of the burn wave formation in the first 50 ps. As the burn wave develops, the fusion reaction rates increase. Around 70 ps, when the burn front is fully formed, the reaction rates remain steady and the yield continues to increase at a linear rate. In Figure 5.11, the yield is plotted for

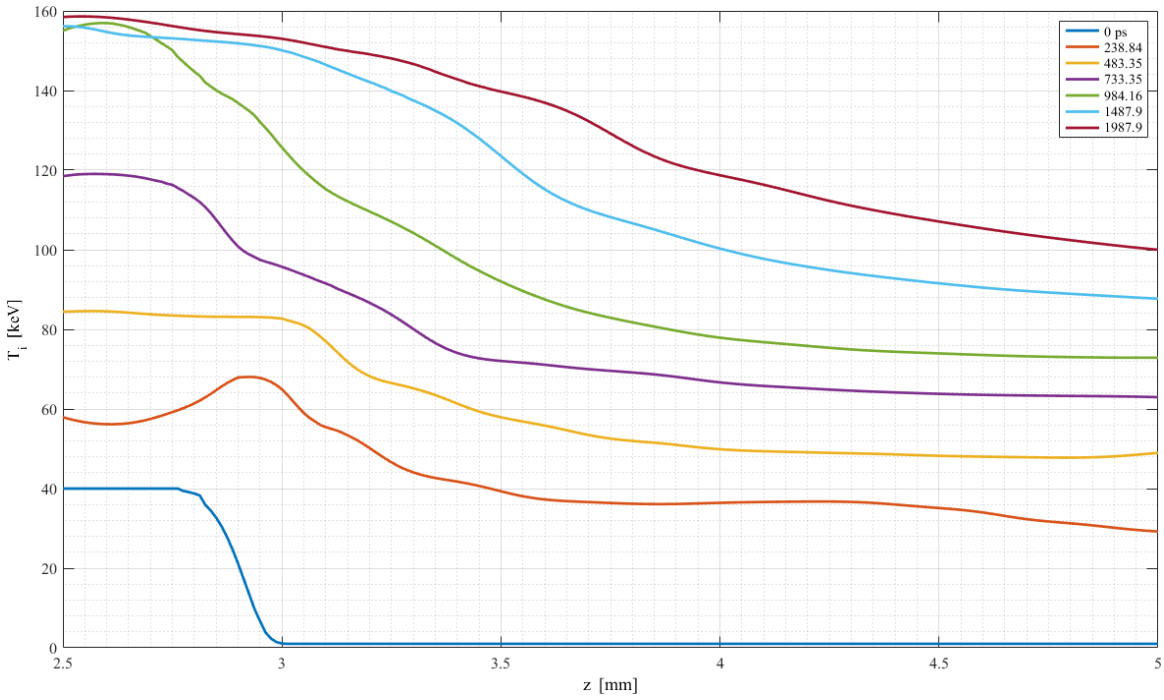

Figure 5.9: Time evolution of the igniting D^6Li pinch over 2 ns with initial hotspot temperature T = 40 keV and density $\rho = 1.5$ g/cm^3.

the entire 2 ns simulation. The yield is still increasing at the end of the simulation, illustrating just how energetic the D^6Li fuel is. The initial mass of the pinch is 35.6 mg. At T = 40 keV in the hotspot and 1 keV in the exterior fuel, the initial energy of the fuel can be estimated as 866.6 kJ. According to Figure 5.11, at 2 ns the yield is 102 MJ, so the fusion gain is $G \approx 117.7$.

When a burn wave launches in the target (for example, around $t = 44.81$ ps in an igniting target) the dominant mechanism of energy transfer is in the electron thermal conduction (4.119×10^{26} W/kg), followed by ion thermal conduction (5.356×10^{20} W/kg), and fusion heating (1.7×10^{18} W/kg). Radiation loss at the same point where the other measurements are taken amounts to 8.84×10^{13} W/kg. However, as the burn proceeds, the radiation losses increase ($\sim 5.4 \times 10^{21}$ W/kg at $t = 1.006$

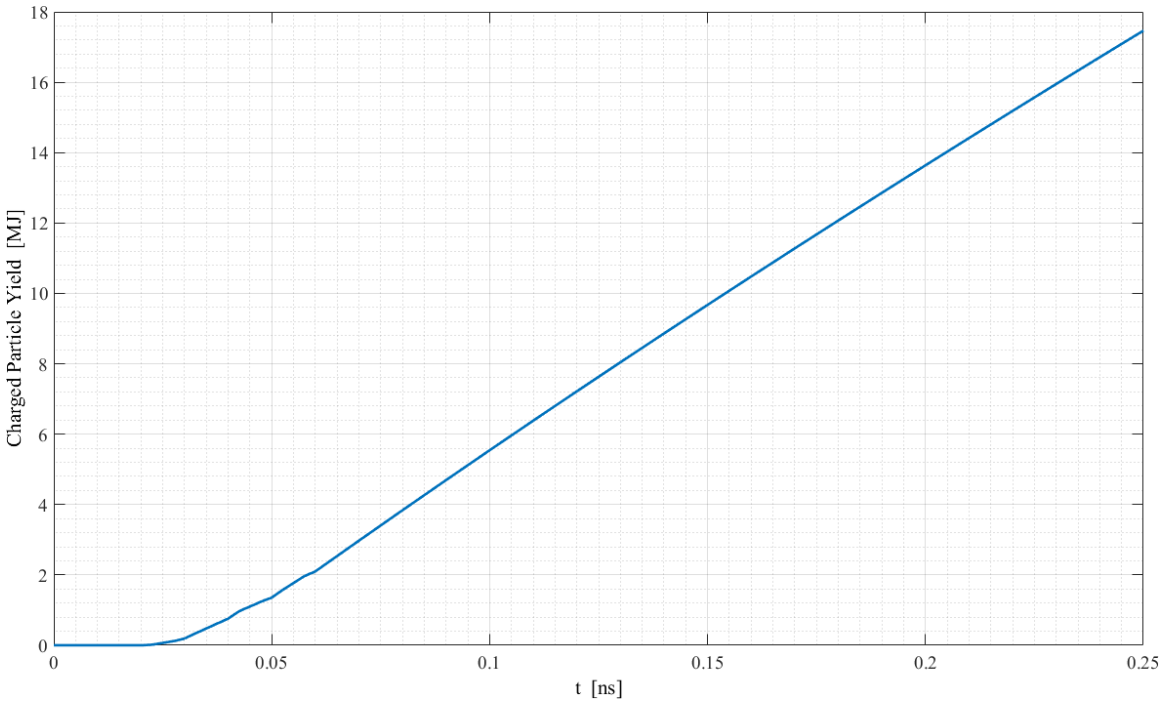

Figure 5.10: Yield resulting from the igniting D^6Li pinch with initial hotspot temperature T = 40 keV and density $\rho = 1.5$ g/cm^3.

ns) along with the fusion ion thermal conduction (6.266×10^{20} W/kg) and fusion ion heating power (2.363×10^{20} W/kg). At this point the electron thermal conduction has decreased to around 6.715×10^{18} W/kg, and continues to fluctuate around this value as the burn proceeds.

The second test case helps demonstrate an approximate margin where ignition can occur in a D^6Li pinch. With the same densities of case 1, the hotspot temperature is lowered to 35 keV. Figure 5.12 shows the evolution of the pinch ion temperature along the z-axis over a time period of 740 picoseconds. At the beginning of the simulation the temperature immediately begins to decrease in the hotspot as it loses heat due to electron thermal conduction through the rest of the pinch. The yield

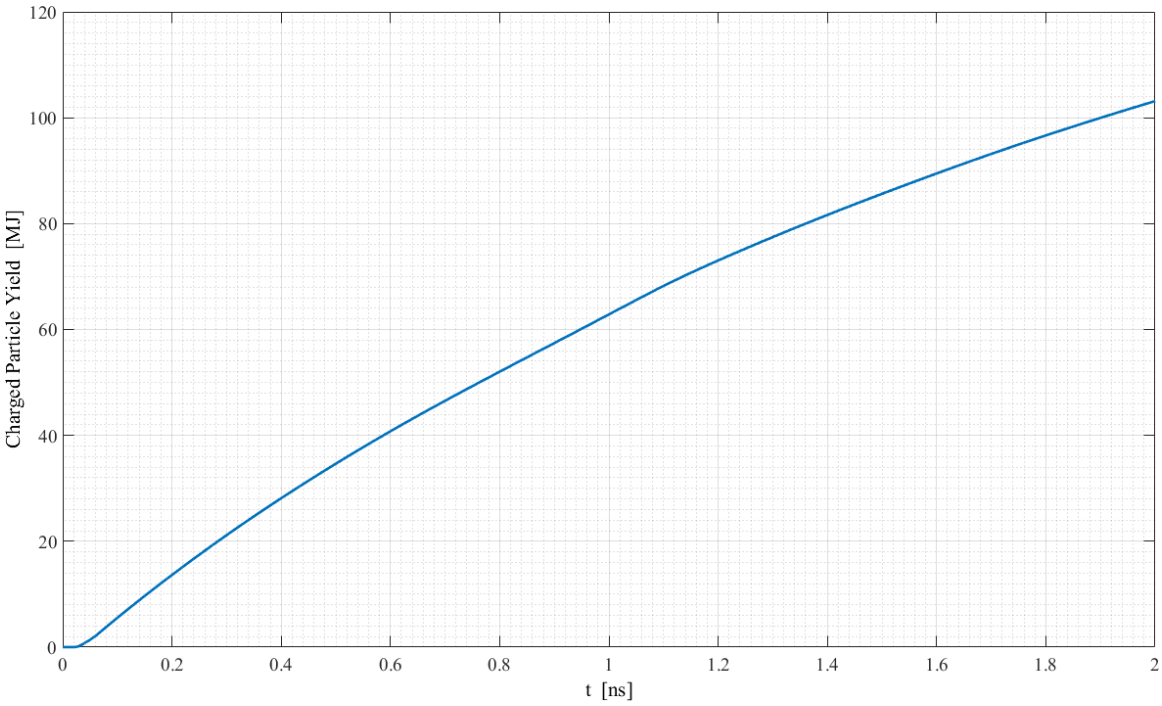

Figure 5.11: Yield resulting from the igniting D^6Li pinch with initial hotspot temperature T = 40 keV and density $\rho = 1.5$ g/cm^3.

is plotted in Figure 5.13, showing the initial heating from fusion reactions begin to decrease within the first 200 ps. At about 1 ns, the reaction rates drop and the yield peaks around 9.5 kJ. With an initial energy in the pinch of 783.66 kJ, the gain is greatly reduced to $G \approx 0.012$.

5.3.2 Effects of ρ_{spark}/ρ_{ext} on Ignition and Burn Wave Propagation

Test cases 3 and 4 help illustrate the utility of burn waves in the pursuit of target ignition. Figure 5.14 and Figure 5.15 show the time evolution of the ion temperature and yield from a pinch with initial conditions $T_{hs} = 40$ keV, $\rho_{hs} = 0.75$ g/cm^3, and $T_{ext} = 1$ keV, $\rho_{ext} = 1.25$ g/cm^3. This test case represents a target with a small compression ratio, $C \sim 1.5$, where the hotspot is slightly below solid density

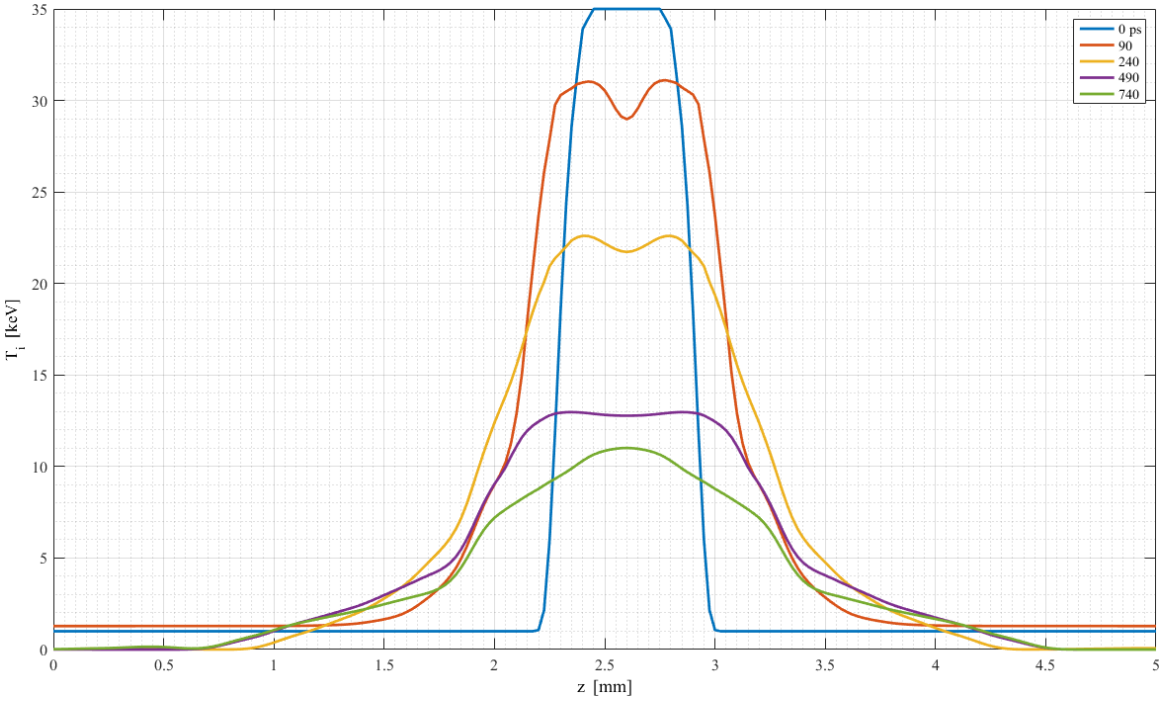

Figure 5.12: Time evolution of batch burn in a D^6Li pinch with hotspot temperature $T_{hs} = 35$ keV. Densities and exterior temperatures are the same as case 1.

(the density of solid D^6Li is $\sim 0.82 g/cm^3$) and the exterior fuel is compressed to 1.5 $\times$ solid density. Also note that the ratio between the hotspot density and the exterior fuel density is

$$\frac{\rho_{spark}}{\rho_{ext}} = 0.6 \tag{5.1}$$

In Figure 5.14 a burn front begins to develop around 290 ps into the simulation. The structure of the burn front is less well defined as compared to case 1, but it is clear that the initial heat in the hotspot propagates outward to heat the rest of the fuel.

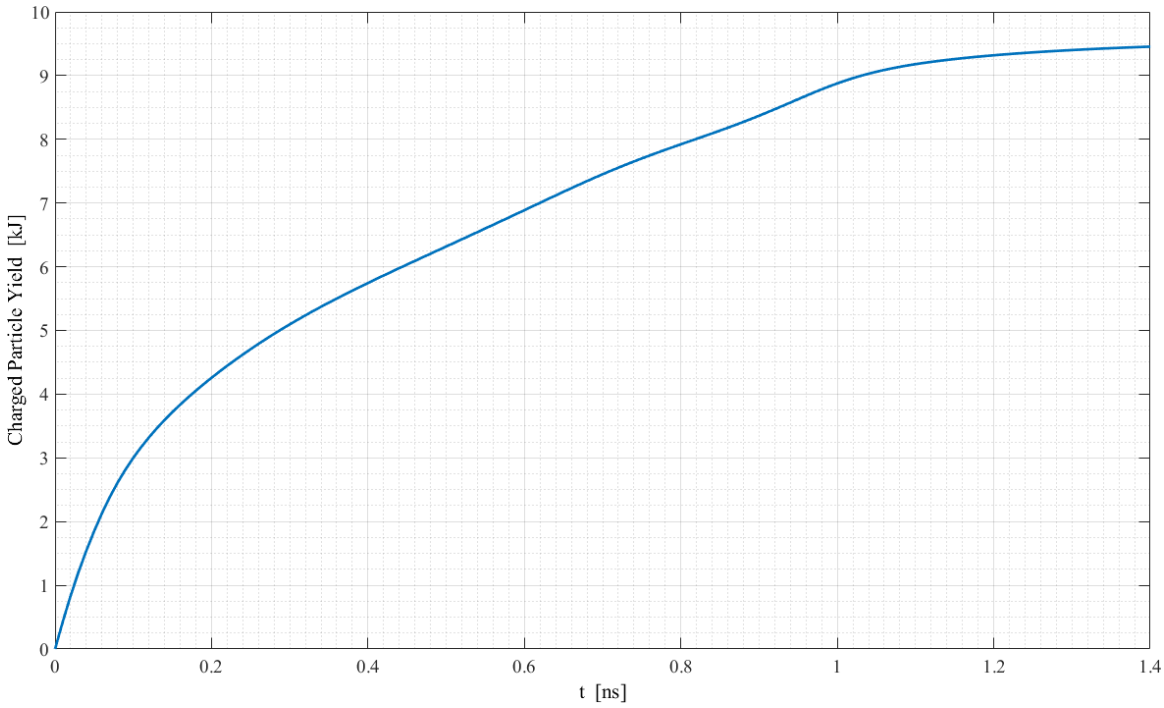

Figure 5.13: Fusion yield from batch burn in case 2 with $T_{hs} = 35$ keV.

At the end of the simulation, the yield is approximately 26 MJ (Figure 5.15). The initial energy in the pinch is ∼433.56 kJ, and the gain is then $G \approx 60$.

In Case 4, the densities are reversed so that

$$\frac{\rho_{spark}}{\rho_{ext}} = 1.67. \tag{5.2}$$

The time evolution of the ion temperature in this case is shown in Figure 5.16, where it is evident that instead of launching a burn wave, the heat from the central hotspot gradually spreads through the rest of the pinch, cooling it entirely without burning much of the fuel. This happens because the reaction rates in the dense hotspot are high enough to burn the fuel quickly and the stopping power is also high enough

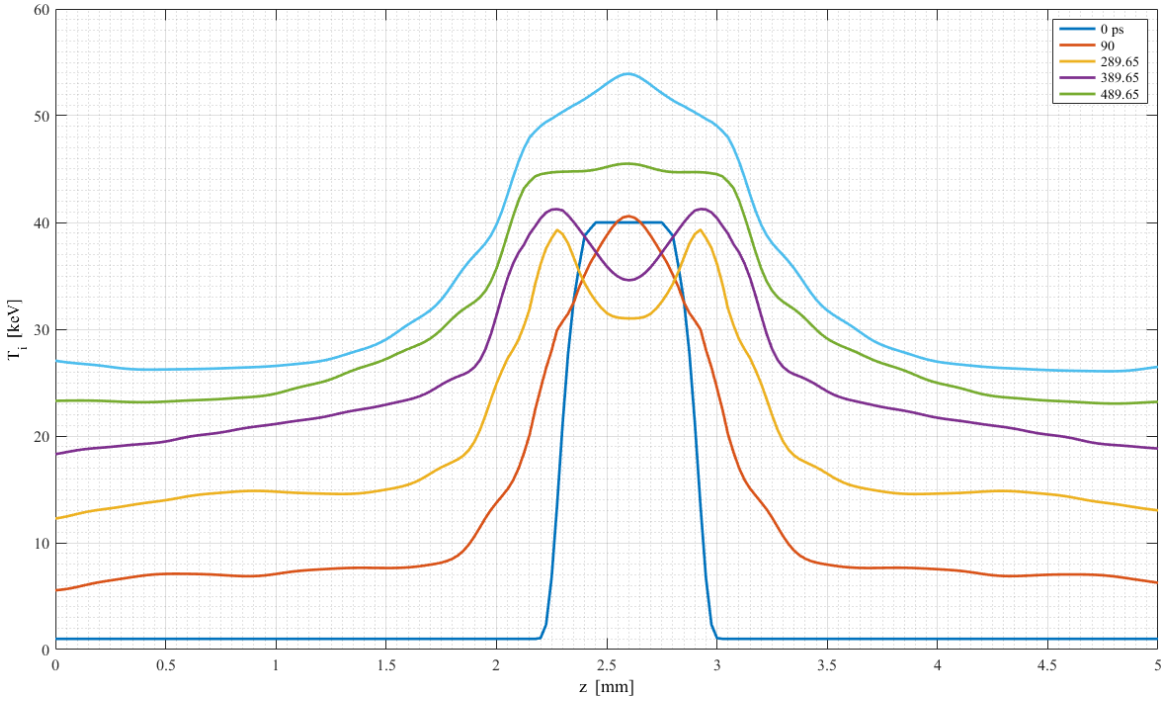

Figure 5.14: Time evolution of ion temperature in case 3 with $T_{hs} = 40$ keV, $\rho_{hs} = 0.75$ g/cm^3, and $T_{ext} = 1$ keV, $\rho_{ext} = 1.25$ g/cm^3. A weak burn front from the hotspot in the center of the pinch moves outward to heat the exterior fuel of the pinch.

to confine charged particles to the hotspot region, preventing the energy of fusion products from heating the exterior fuel. As time progresses, the hotspot will eventually lose heat through thermal conduction and bremsstrahlung, cooling the plasma. Overall, the yield in this case is ≈ 8.98 kJ. With an initial energy of ≈ 1.162 MJ, this implies a fusion gain of $G \sim 0.008$. This result stands in stark contrast with the previous test case, which achieved a gain of $G \sim 60$.

These considerations lead to the important observation that when the density ratio ρ_{spark}/ρ_{ext} is greater than unity, thermonuclear burn tends to be confined to the hotspot without launching a burn wave through the rest of the fuel. Likewise,

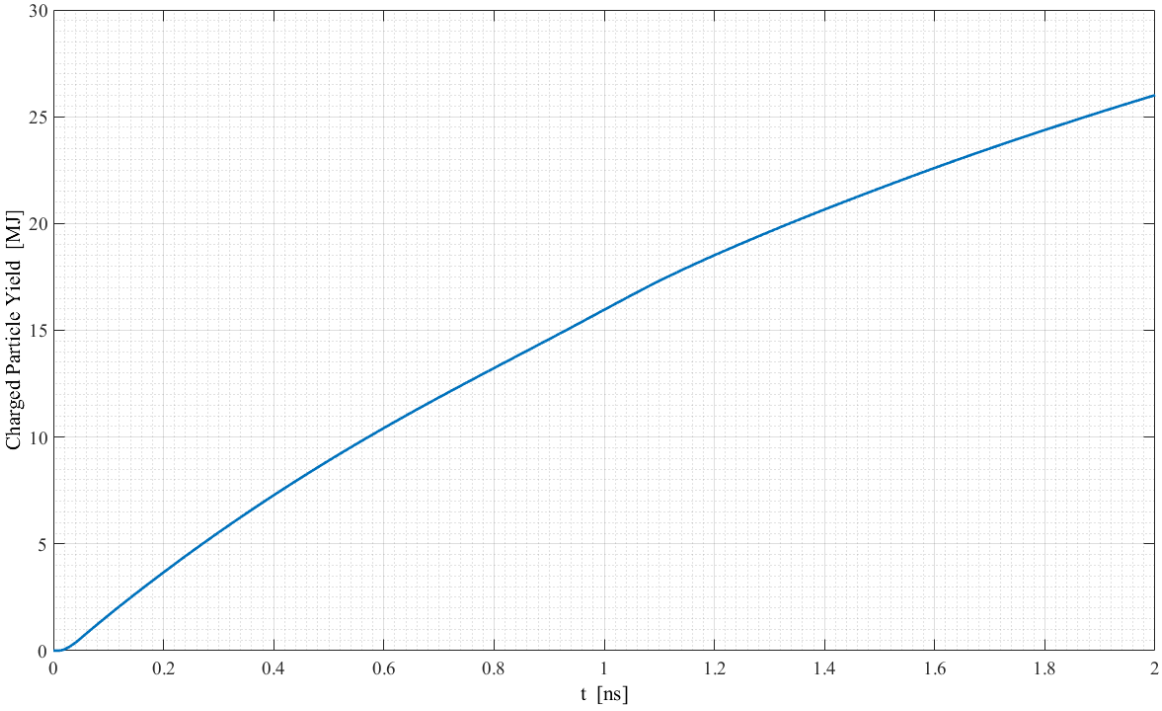

Figure 5.15: Yield of the D^6Li pinch in test case 3.

when the ratio is less than or unity, a burn wave will form and propagate through the exterior fuel.

If the hotspot and exterior fuel are dense enough, they will burn fast enough to achieve significant yield without need of a burn wave to ignite. The fifth test case illustrates this possibility of ignition by batch burn without launching a burn wave in the plasma. The first observation to note is the rapid rise of the ion temperature in the hotspot in Figure 5.19 due to the high initial density and temperature. The ion temperature peaks at 60 ps and then begins to decrease for $t > 60$ ps. Next notice how the heat of the initial spark does not begin to heat the rest of the pinch. At first, around 40 ps, a burn wave begins to form, but it does not add much energy to the fuel outside the hotspot. Instead, the hotspot region continues to heat without expand-

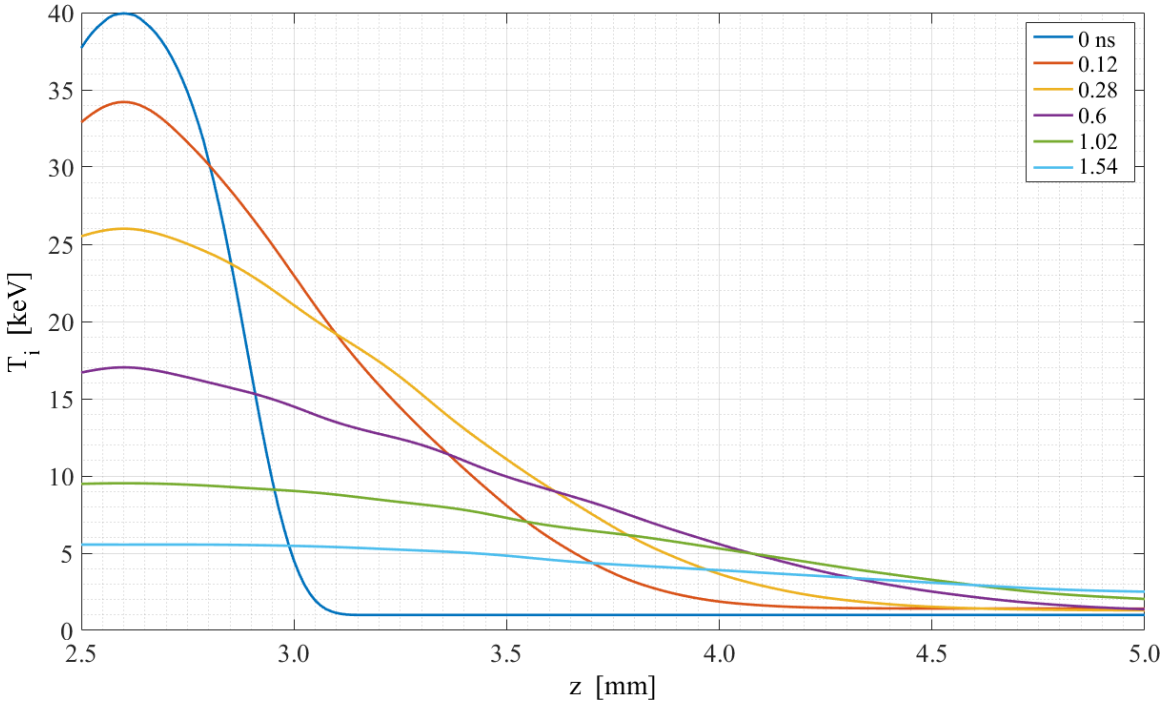

Figure 5.16: Time evolution of $T_i(z)$ in case 4 with $T_{hs} = 40$ keV, $\rho_{hs} = 1.25$ g/cm^3, and $T_{ext} = 1$ keV, $\rho_{ext} = 0.75$ g/cm^3.

ing. This behavior continues in Figure 5.20 until around 240 ps where the hotspot temperature begins to equilibrate with the exterior fuel. At this point, the plasma continues to heat through thermonuclear burn and the equilibration of temperature between the hotspot and exterior fuel.

In this case, the pinch achieves batch burn ignition due to its high fusion energy output of ∼43 MJ (Figure 5.21) compared with an initial energy of ∼1.5 MJ. The gain is then $G \approx 28.6$. The difference here is the lack of a burn wave launching and propagating in the pinch. Also note that the density ratio in this scenario is

$$\frac{\rho_{spark}}{\rho_{ext}} = 1.67, \tag{5.3}$$

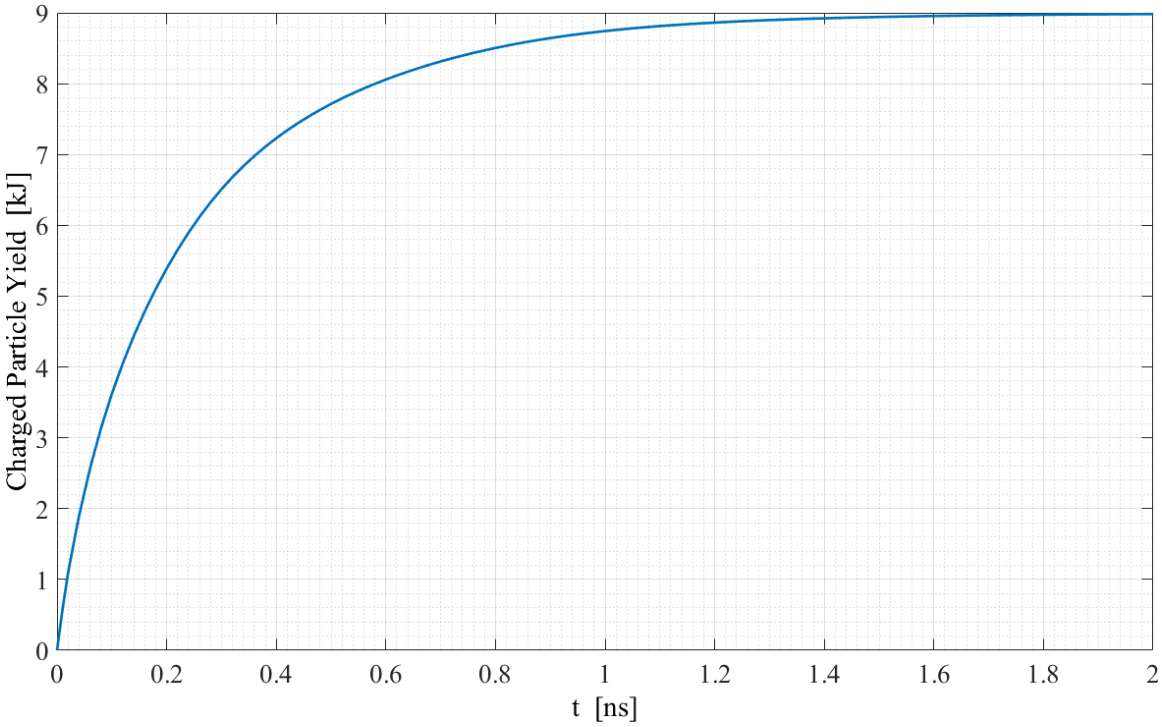

Figure 5.17: Yield of the D^6Li pinch in test case 4.

which is in agreement with the previous hypothesis that the ratio between the hotspot density and exterior fuel influences the formation of burn waves in the plasma. This will be discussed further in Section 5.4.

5.3.3 Pinch Experiment With Simulated Energy Input From Charger-1

The last test case to examine is a simulation where the initial conditions of the pinch are determined based on an input energy equivalent to the output of the Charger-1 facility at UAH running at 30% efficiency. Charger-1 is a 580 kJ pulsed power machine acquired by UAH for the purpose of running sub-scale fusion experiments. This facility serves as a first step toward the development of fusion propulsion

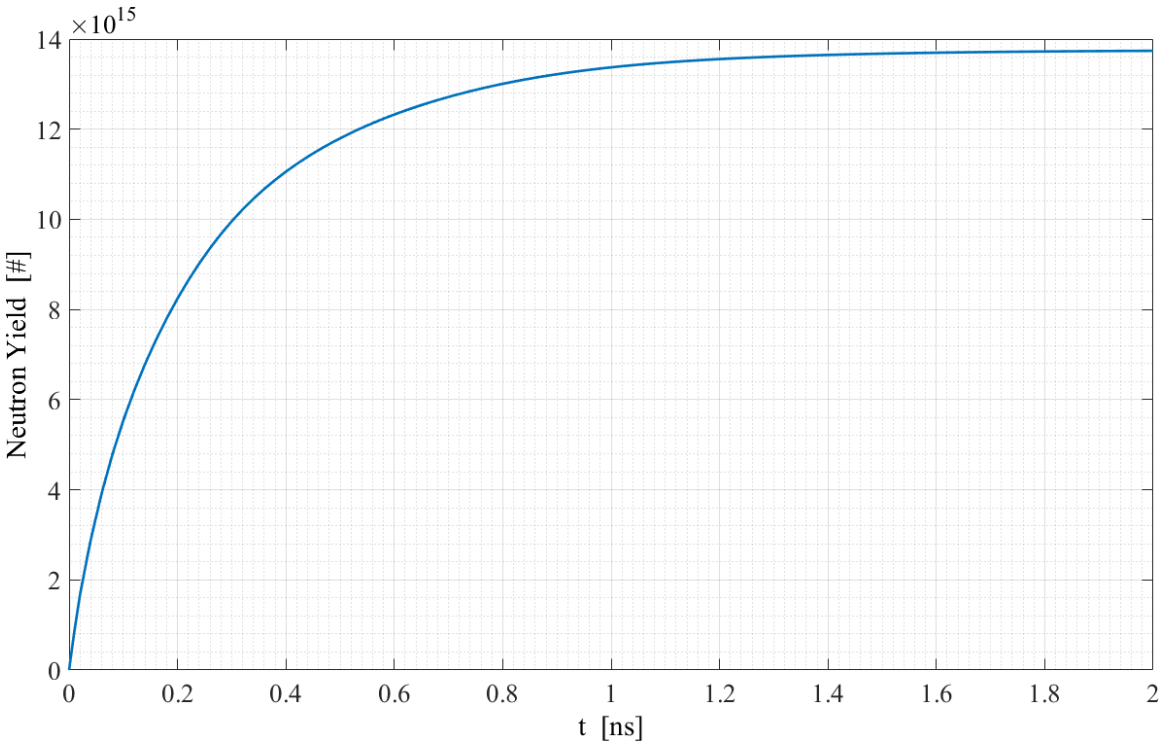

Figure 5.18: Neutron yield of the D^6Li pinch in test case 4.

technology for deep space missions. The first phase of experimentation will begin with standard wire array diodes to benchmark Charger-1's output performance against prior work. The next phase involves examination of the output from D^6Li wires. One of the most crucial aspects of the UAH research program in fusion propulsion is the measurement of fusion yield and development of scaling laws. It would be senseless to initiate any program without first developing a database to provide guidance for scaling any concept beyond breakeven. Additionally, diagnostic data from fusion experiments on Charger-1 will provide a basis for benchmarking SPFMax, improving the code's accuracy and predictive capability. Iterating between experimental target campaigns and modeling will help develop an understanding of general scaling laws

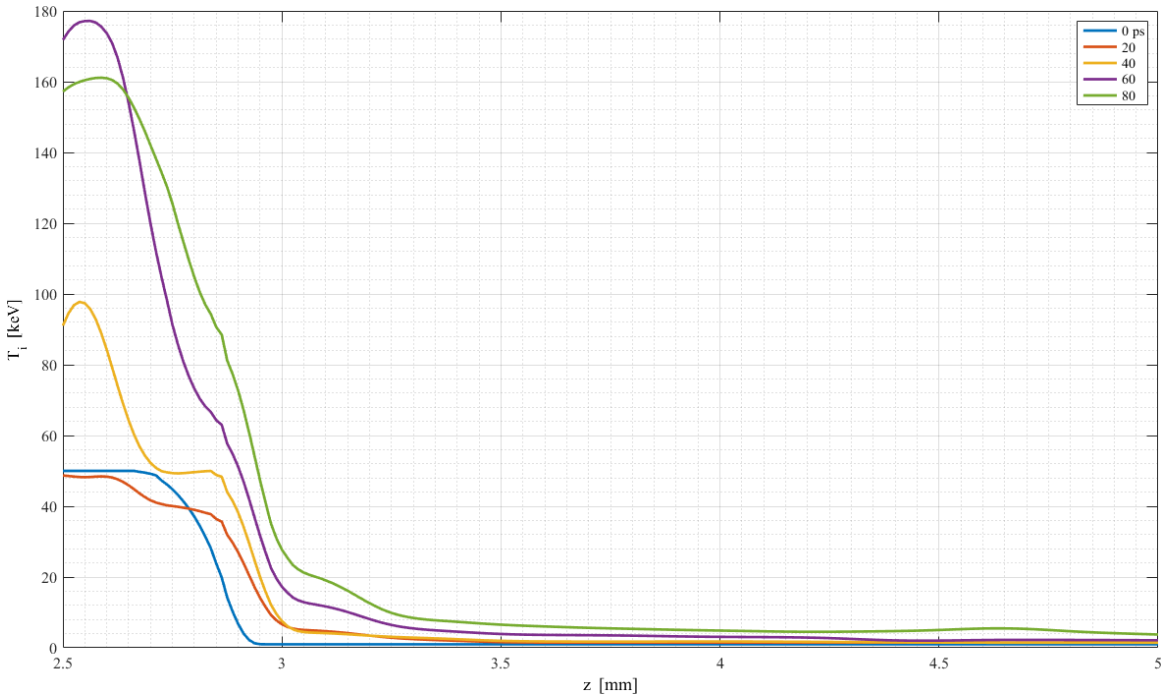

Figure 5.19: Time evolution of ion temperature in case 5 with $T_{hs} = 50$ keV, $\rho_{hs} = 2.5$ g/cm^3, and $T_{ext} = 1$ keV, $\rho_{ext} = 1.5$ g/cm^3. The hotspot in the center of the pinch heats up rapidly and the ion temperature peaks close to 180 keV at 60 ps begins to decrease for t ¿ 60 ps. The burn front that begins to form around 40 ps does not propagate to the exterior fuel.

versus stored driver energy. Comparison of yield measurements with calculations (such as those below) will also aide understanding of instabilities in the wires because they provide beam-target scaling of yield at currents below 10 MA [88].

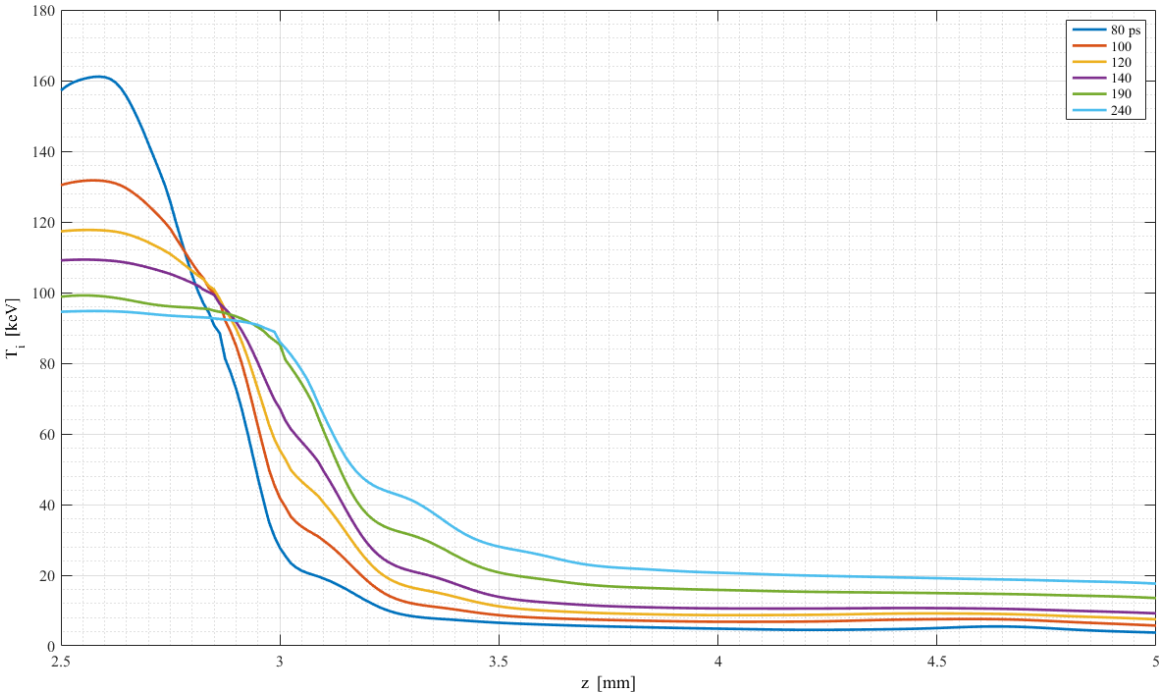

Figure 5.20: Ion temperature time evolution for period $80ps \leq t \leq 240ps$ in case 5. The temperature continues to decrease in the hotspot, equilibrating with the rest of the pinch.

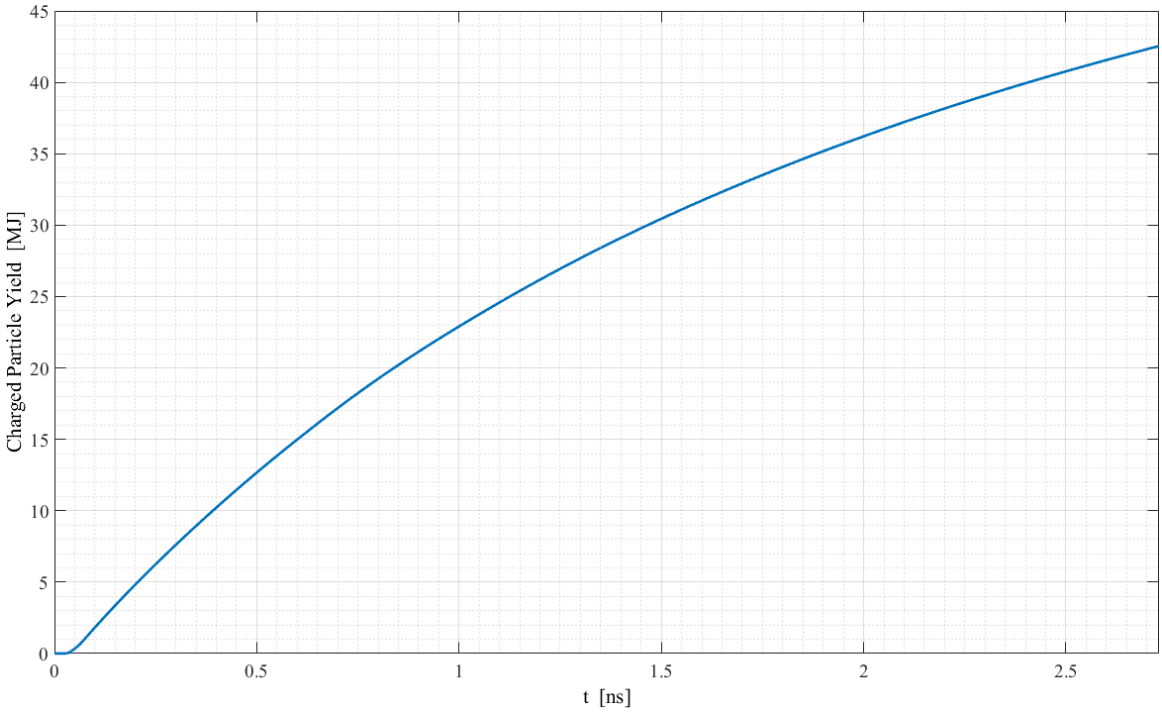

Figure 5.21: Fusion yield vs. time for case 5.

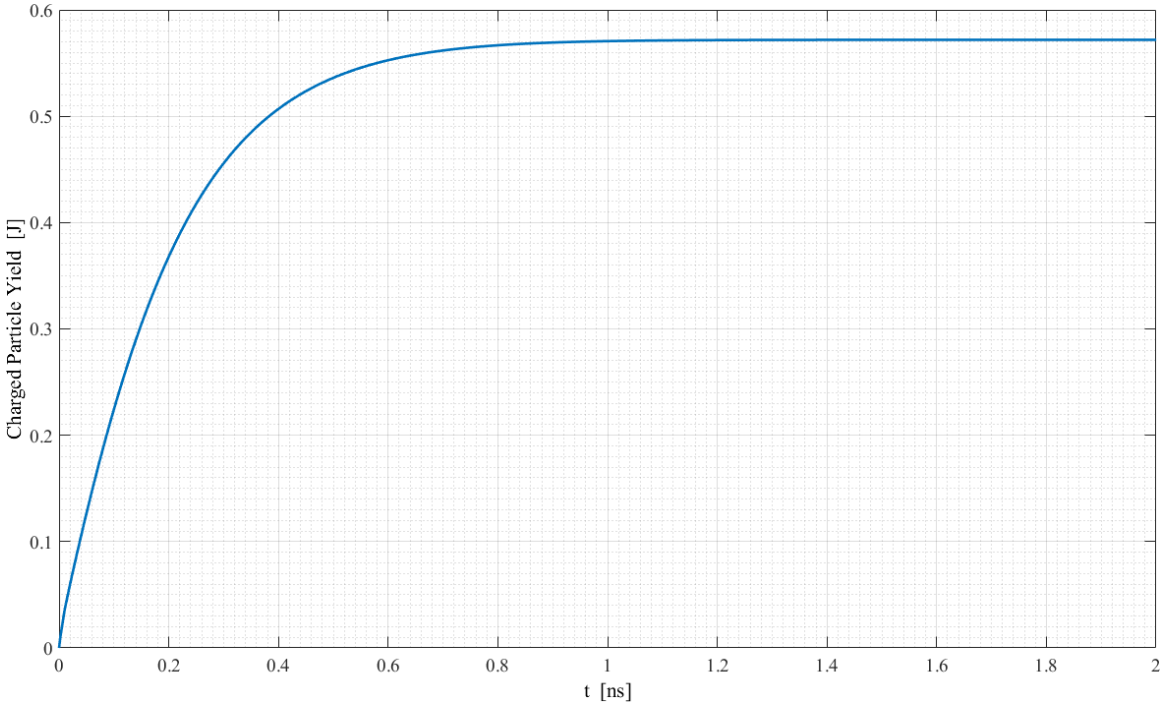

Figure 5.22: Predicted fusion yield from a D^6Li z-pinch with a simulated energy input of 174 kJ from Charger-1 at 30% efficiency.

The results presented in Figure 5.22 and Figure 5.23 are a first attempt at predicting a possible output from a D^6Li experiment using the Charger-1 facility. Assuming the initial energy in the pinch is equivalent to the output of Charger-1 at 30% efficiency (174 kJ), the initial temperature in the pinch can be estimated around 1.5 keV. Note that this also assumes the energy is deposited in the pinch instantaneously and the output efficiency may be lower, so the estimate given here is an upper bound at best. From Figure 5.22, the fusion yield is slightly less than 0.6 J. The neutron yield in Figure 5.23 approaches its maximum of slightly less than 9×10^{11} around the 1 ns mark. Additionally assuming that the majority of the fusion reactions that occur in the pinch at this energy level are DD reactions, this estimate

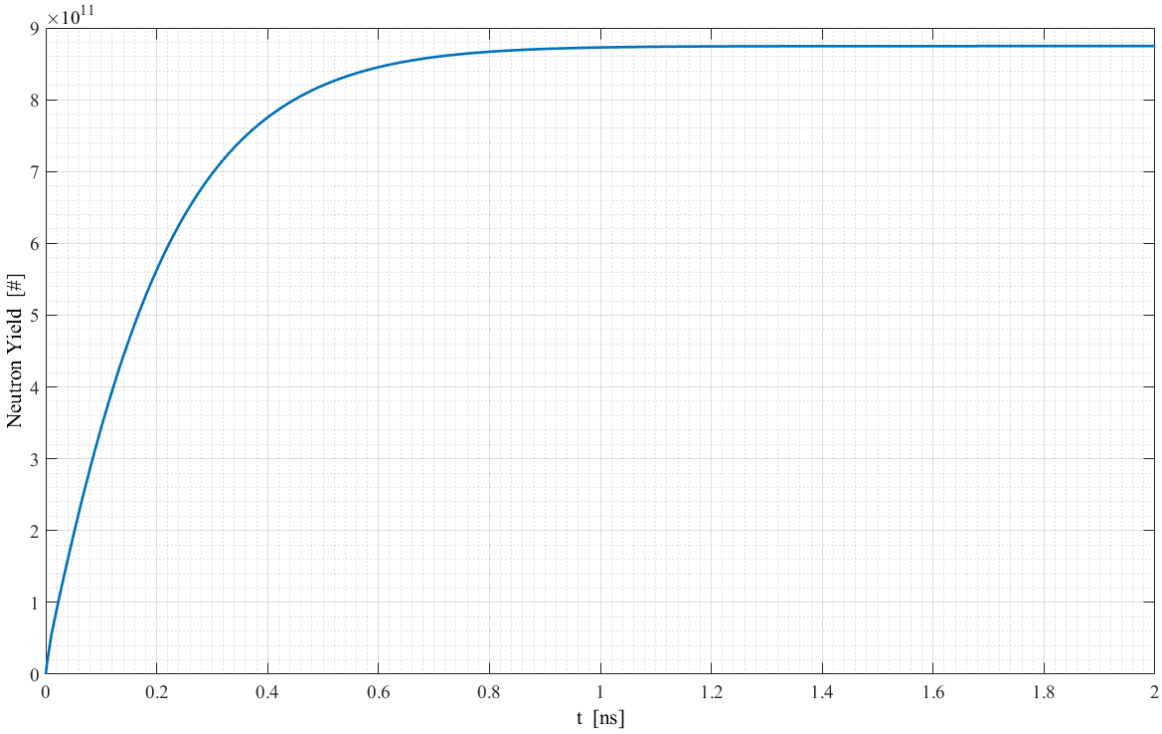

Figure 5.23: Predicted neutron yield from a D^6Li z-pinch with a simulated energy input of 174 kJ from Charger-1 at 30% efficiency.

is quite reasonable. In 2012, Bures *et al.* developed an improved scaling model for neutron production in z-pinches based on experimental data [56]. The scaling model with their improved data takes the form

$$Y_n \sim 0.1(I_{max})^{3.79} \tag{5.4}$$

where I_{max} is the maximum input current to the pinch, and Y_n is the neutron yield. With this scaling, a neutron yield of $\sim 9\times10^{11}$ implies a peak current input of $I \sim$ 2618.22 kA. This current level is on the upper end of what Charger-1 is capable of, but it is a reasonable upper bound to what can be expected from an experiment based on the parameters used in this simulation. As noted above, the estimated initial energy

in the pinch is also an upper bound to the possible energy input from Charger-1 at 30% efficiency. An input current of 1 MA using this scaling law gives a neutron yield of approximately 2.3×10^{10}, so a resulting yield on the order of $\sim10^{10}$ to $\sim10^{11}$ can be reasonably expected. Figure 5.24 shows a prediction based on a 15% efficiency input from Charger-1 of 87 kJ. In this case the initial temperature in the pinch would be approximately 770 eV. The neutron yield in this case, $\sim8\times10^{9}$, is possibly a more reasonable prediction of the performance that can be expected. An input current of $I \sim 700$ kA, according to the scaling law of Bures *et al.*, would give a neutron yield $\sim6.07\times10^{9}$. This current level is well within the performance capability of Charger-1, so this may be an even more appropriate prediction of the neutron yield that can be expected in such an experiment.

5.4 Discussion

Thermonuclear reaction waves, although similar in concept to chemical reaction waves, develop through the interplay of different modes of energy transfer to the electrons and ions in the plasma. Since the temperatures in thermonuclear reaction waves are so high, the plasma is completely ionized, giving rise to complex behaviors that result in a wave structure quite different to the structure of chemical burn fronts.

In a completely ionized medium, the difference in properties of ions and electrons give rise to a difference in their respective temperatures. Since ions are more massive than electrons, their viscosity will be greater than that of electrons, meaning ion viscous heating becomes significant as the temperature increases in the pinch [89]. At the same time, the electrons will have much higher conductivity due to their mo-

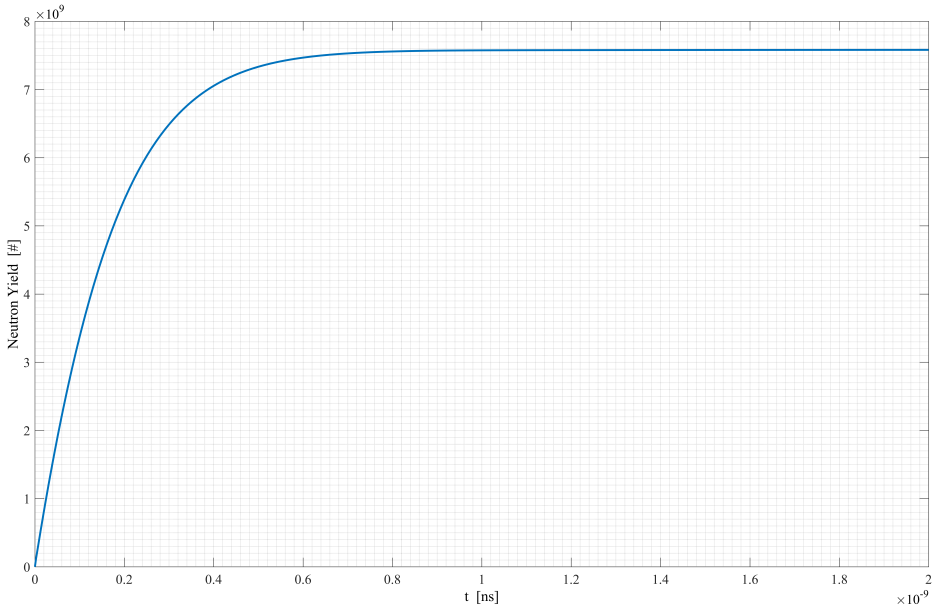

Figure 5.24: Predicted neutron yield from a D^6Li z-pinch with a simulated energy input of 87 kJ from Charger-1 at 15% efficiency.

bility. In addition to these factors, the charge states of the various ion species in the plasma cause differences in how energy is distributed from nuclear reactions. This is partially because the stopping power for a given species in the plasma is $\propto Z_{eff}^2$.

The small mass and corresponding mobility of the electrons means they will interact with high energy fusion products more readily than the ions. This results from the energy transferred to a target particle being inversely proportional to its mass:

$$\Delta E = \frac{(\Delta p)^2}{2m}. \tag{5.5}$$

Thus, the low mass of the electrons means they will absorb a large amount of energy from a fast particle moving through the plasma. As the plasma temperature increases, however, the high energy particles deposit more energy into the plasma ions and less in the electrons [90–92], further increasing the reaction rates in the plasma to yield more high energy particles.

The key process involved in launching burn waves in a given target is the stopping power. Whether a burn wave launches or not is dependent upon a couple of factors. First, small regions of the plasma (such as a hotspot) self-heat due to the initially high stopping power. As the plasma heats up, the internal pressure causes the hotspot region to expand, decreasing the local density. The drop in density and concurrent temperature increase reduces the stopping power of the high energy fusion products, extending their range outside the hotspot boundary to heat a small layer of the surrounding fuel. This process continues, propagating through the rest of the fuel as can be seen in Figure 5.8. Second, if the density of the surrounding fuel is much greater than that of the hotspot ($\rho_{ext} >> \rho_{hotspot}$), the stopping power of the outer fuel will be high enough to prevent the high energy particles in the hotspot from moving further, trapping them in the hotspot region. It follows that the outer fuel does not receive any further heating from the expanding spark region. If this were to happen, the hotspot region would heat up and expand but eventually be tamped out by the higher density fuel. This implies that the ratio of the hotspot density with the density of the outer fuel is a key parameter when determining the likelihood of burn wave initiation. A natural corollary to this conclusion is the ability to predict target ignition as a result of burn waves launching in the target.

One important implication of the results presented here is the possibility of achieving ignition in a D^6Li pinch very near solid density. This is a major point because it significantly lessens the requirements for ignition since D^6Li fuel is solid at room temperature, reducing the compression needed to reach sufficiently high reaction rates in the plasma. Another aspect of this is the reduction of initial temperature needed: if one can achieve a sufficiently high temperature in a localized area at solid density surrounded by low temperature fuel at a slightly higher density, a burn wave will launch into the colder fuel, raising its temperature as well. As the wave propagates through the rest of the pinch more fuel burns, increasing the overall yield high enough to exceed the initial energy deposited in the pinch, leading to ignition. The initiation of the burn wave will be determined by the density ratio ρ_{spark}/ρ_{ext}. Results in this study suggest that when

$$0.5 \lesssim \frac{\rho_{spark}}{\rho_{ext}} \lesssim 1 \tag{5.6}$$

a burn wave will launch in the plasma. Due to the dependence of plasma stopping power on the density, this shows the importance of how the exterior plasma density will affect the ability of a burn wave to propagate outward from the hotspot. If the ratio drops below 0.5, the exerior fuel is at a high enough density to attenuate the outward expansion of the hotspot, so a burn wave will not develop. While there will be fusion output from the pinch in this case, there is no burn wave to induce an increased output, burning more of the fuel. Instead, the fuel will batch burn and

the reaction rates level off rather quickly. If the density ratio drops below ~ 0.1, the dense exterior fuel will tamp the burning plasma in the hotspot, quenching the burn before it can ignite the rest of the fuel. When the density ratio increases to be greater than unity, a well-defined burn wave will not launch because the majority of the burn occurs in the hotspot before it expands outward. While the plasma will ignite, the requirements to achieve ignition will be high because the increased densities require higher compression ratios to reach them. This is why spark ignition combined with the natural solid density of D^6Li fuel is a desirable method for igniting fusion plasmas: the possibility of launching a burn wave from a hotspot in a D^6Li pinch at solid density negates the need for high compression and creates a plasma with reactivities that are 8 orders of magnitude higher prior to compression. In case 3 above, ignition with a gain factor of $G \approx 60$ is achieved with an initial energy of $\sim$433.56 kJ. Assuming this energy is deposited in the pinch by a driver with 15% efficiency, the total input energy required for ignition is $\sim$2.89 MJ. This energy output is quite achievable by current pulse power facilities, implying that this approach to fusion ignition is indeed feasible with current technology.

It is important to note that these simulations do not include the effects of magnetic fields, nor do they include any secondary fusion reactions such as DT that might occur between the products of the D^6Li reactions. This is significant because it makes calculations of fusion yield implicitly conservative. The reasoning for this follows from a few key factors:

1. The magnetic field surrounding the z-pinch will suppress electron thermal conduction losses while confining charged fusion products longer so they deposit their energy locally to heat the plasma further;

2. The insulating effect of the magnetic field significantly eases the task of ignition by lowering the required pressure at stagnation and driver requirements;

3. Secondary exothermic reactions occuring between the products of DD and D^6Li reactions are highly probable, and their energy output further enhances the overall yield of the plasma.

In addition to their conservatism, these results are also encouraging because they imply that instabilities in the pinch may actually enhance the ignition process by trapping small regions of plasma that will quickly energize the particles to levels high enough to launch a burn wave along the pinch axis through the rest of the fuel. These energized particles may even be directed along the axis due to their interaction with voltage gradients in the plasma that occur as a consequence of the change in current flow through these regions. In other words, disruptions in the pinch causing large voltage gradients in a given region influence the plasma particles in that area to move in a direction concomitant with the change in voltage once the disruption has reconnected. This hypothesis will be addressed in future work.

CHAPTER 6

CONCLUDING REMARKS

Our knowledge and use of the laws of nature that enable us to fly to the Moon also enable us to destroy our home planet with the atom bomb. Science itself does not address the question whether we should use the power at our disposal for good or for evil. The guidelines of what we ought to do are furnished in the moral law of God. It is no longer enough that we pray that God may be with us on our side. We must learn again that we may be on God's side.

—Wernher von Braun

6.1 Summary

In Chapter 1, the motivations for this dissertation are introduced, focusing on the rationale for space travel, the need for fusion propulsion to do so, and the practicality of D^6Li as a cost-effective fuel. Although the usage of D^6Li as fusion fuel is not a new concept [9, 93–96], there is not much work in the literature investigating its use in practical fusion concepts. More specifically, there has been no apparent research studying the use of D^6Li in a z-pinch target configuration or the conditions for which thermonuclear burn will propagate through it to achieve ignition. In this context, ignition occurs when a fusion plasma produces enough energy to sustain

itself without auxiliary heating by external sources. Indeed, the question of whether it is even possible to successfully ignite D^6Li targets without requiring inordinately high driver energies finds no satisfactory answer in current literature. The primary objective of this dissertation is to address this question by determining if it is possible to achieve hotspot ignition in a D^6Li z-pinch target. The conditions for which ignition will occur turn out to be more feasible than expected due to the high dependence of fusion reactivity on the density of the fuel. This possibility of ignition is further enhanced if a hotspot in the compressed target launches a burn wave through the colder fuel surrounding it.

The primary computational tool used in this study is a Smoothed Particle Hydrodynamics (SPH) code called SPFMax, described in Chapter 4. To achieve the primary objective of this dissertation a recently formulated model of plasma stopping power is integrated into SPFMax in order to study the behavior of burning fusion plasmas. In Chapter 3, the discussion focuses on the stopping power model used in this study and its effects on the ranges of charged particles produced in DD and D^6Li plasmas. By varying the density and temperature of the plasma, the results illustrate the plasma's ability to retain energy produced by fusion reactions.

The density of the fuel proves to be a heavy influence on where the energy from fusion reactions is deposited in the plasma. Further, this implies that the density has a two-fold influence on the reaction rates in the plasma: (1) the reaction rate is proportional to the square of the density, n^2, and (2) the reactivity, $\langle \sigma v \rangle$, is a function of temperature, which is a function of energy deposition in the plasma via the stopping power. The reliance of stopping power on the plasma density combined

with the significant influence of the stopping power on burn wave propagation is indicative of why the ignition of the plasma is so sensitive to its density.

For the purpose of understanding the conditions required to achieve hotspot ignition in a D^6Li z-pinch, the size and configuration of the plasma is held constant. The plasma configuration shown in Chapter 4 serves as the foundation for exploring the effect of density and temperature on burn wave initiation. The simplified parameter space helped to elucidate a few important results. First, a central hotspot with a temperature of $T = 40$ keV between sections of colder fuel with $T_{ext} = 1$ keV will launch a burn wave in dense D^6Li, achieving ignition with considerable yield. Second, in the same configuration with a hotspot in approximately solid density D^6Li ($\sim 0.75\ g/cm^3$) at $T_{hs} = 40$ keV and exterior D^6Li fuel at a slightly higher density of $1.25\ g/cm^3$ with $T_{ext} = 1$ keV, a burn wave will launch from the hotspot, igniting the plasma. Third, if these densities are reversed so that $\rho_{hs} = 1.25\ g/cm^3$ and $\rho_{ext} = 0.75\ g/cm^3$, a burn wave will not occur and the pinch cools without reaching ignition. Finally, if a D^6Li z-pinch is compressed to densities higher than solid density ($\sim$1.5 $\times$ solid density), a burn wave is not required for it to ignite. This is evident in case 5 of Chapter 5 where the hotspot and exterior fuel are 2.5 and 1.5 g/cm^3, respectively.

When considering these conclusions, it is important to keep in mind the assumptions underlying the simulations. Since the influence of a confining magnetic field is not included here, the results are somewhat conservative. This follows from the insulating magnetic field contributing to the confinement of charged particles, shortening their ranges in the plasma, and its suppression of thermal conduction

losses. Additionally, the dynamics and effects of implosions are not considered here. It is assumed that the pinch is at full compression and stagnation. Therefore, the processes by which the pinch reaches the conditions stipulated here must be considered in order to determine driver requirements more accurately.

In Section 5.3.3, a D^6Li pinch is assumed to have an initial energy equivalent to the output of the Charger-1 pulsed power facility at UAH at 15 and 30 percent efficiency. The purpose of these simulations is to examine the possible output that can be expected from a D^6Li pinch experiment using Charger-1 as the driver. Important diagnostics in such experiments using Charger-1 include neutron time-of-flight sensors and neutron counters, x-ray diodes, and a Schlieren system or streak camera. Other diagnostics that are considered essential for any experiment on Charger-1 include B-dot and high voltage probes for measuring currents, voltages, and magnetic field strengths. A basic diagnostic package using the components just listed is sufficient to acquire the essential data in these experiments to evaluate the predictions of the simulations. Predicted neutron yield in each case can be compared with measurements of the neutron yield from experiments with the same parameters. Data acquired in these experiments can then be used to benchmark and improve SPFMax, enabling more accurate simulations to aide future experimental designs. The predictions shown in this study are meant to be a humble first step toward this experimental process.

6.2 Future Research and Development

Fusion propulsion is a difficult endeavour. A few factors contribute additional constraints to fusion propulsion systems that are not generally considered for ground-

based reactors. First, space mission objectives determine the payload and propellant masses to be carried. Due to the expense of lifting any payload to orbit, the mass of the propellant and of the propulsion system itself must therefore be reduced as much as possible. Related to this constraint, any auxiliary systems required to support the propulsion system must be reduced or their mass limited. Such systems would include cryogenics, fuel systems, or auxiliary field magnets. These constraints provide motivation for reducing complexity in the propulsion system as much as possible. Another trade-off that must be considered is between propulsion system thrust and exhaust velocity. For this reason, the thrust-to-weight ratio and specific power become important parameters in space system design. By increasing the energy density of the propulsion system as high as possible, routine travel in the solar system over reasonable timescales can be made feasible.

It is a slight understatement to say that there are some obstacles to be overcome in order to reach such lofty goals. Following this work are a few interesting avenues for exploration in future research.

Simulations over an expanded parameter space of density and temperature are desirable to better understand the boundary between ignition and non-ignition in D^6Li pinches. Exploration of the $\rho - T$ parameter space will lead to an understanding of the minimum conditions required at stagnation to achieve ignition. It is important to note, however, that the minimum conditions capable of achieving ignition will not necessarily lead to appreciable yield from the plasma. This is because such conditions are just enough for the plasma to reach the state where the energy produced by the plasma exactly balances its losses. Such a state will typically not achieve

fusion reaction rates high enough to burn much of the fuel, leading to low yields. The minimum conditions in this case merely establish a lower bound in the $\rho - T$ parameter space. The logical progression of this research will then be to expand the parameter space and develop scaling laws that can be used to optimize target designs for experiments.

Related to the lower bound in the $\rho - T$ parameter space mentioned above, it is prudent to consider whether there exists a minimum fusion reaction rate, dN/dt, per pulse required for a propulsion system to be effective. For a propulsion system to work, net gain from fusion is technically not required. This is because, in the case where there is not enough fusion energy being generated in each pulse to achieve net gain, the fusion reactions that do occur still serve to add enthalpy to the plasma exhaust, increasing the amount of power available for thrust. In this sense the thruster would effectively be a pulsed plasma thruster with a higher power output due to fusion. If one accepts this assessment to be true, then a minimum reaction rate per pulse would not be required. In the case where one is attempting to achieve a net gain from fusion output, a minimum reaction rate would be calculated based on the ignition conditions of the fuel being used. As an example, using D6Li and assuming the ignition conditions found in this study are feasible, the minimum reaction rate required would be calculated for a density of 0.75 g/cm^3 at a temperature of about 45 keV. Assuming a 1 cm^3 reacting volume, this calculation results in a reaction rate $dN/dt \approx 3.03 \times 10^{28}$ reactions per second (s^{-1}). If the reaction rate falls below this threshold, a net gain in energy might not be achieved. However, the fusion output will still provide some benefit to the performance of the thruster.

Using the methods discussed in this work, an important figure of merit worth exploring is the minimum flame kernel (a combination of mass and temperature) necessary to achieve gain greater than unity. This is a multidimensional problem. This study has provided a "rule of thumb" involving the ratio of densities of the target and surrounding cold fuel layer. However, these results were generated for only a few cases, and it will be highly dependent on the fuel, cross sections, fusion product stopping distances, and target geometry. The numerous multi-variable parameters involved in determining simple ignition conditions will therefore complicate how the minimum flame kernel required to achieve net gain is calculated. In any case, such a figure of merit will be a powerful tool in the engineering design of future fusion propulsion systems.

It will also be important to include an intensive study of magnetic field effects on the ignition conditions since it is the primary compressive force on the pinch while also confining the plasma and reducing thermal losses. The parameter BR features prominently in MIF ignition studies [97–99], and will be important to include in further studies of D^6Li pinches because of the role the magnetic field plays in both the initial conditions of the z-pinch (or liner) and the confinement of the burning plasma at stagnation.

Further work on the role of instabilities in the creation of hotspot and beam-target fusion reactions will also provide guidance on how to create plasma configurations that will ignite and burn. Additionally, research in non-equilibrium plasmas with non-Maxwellian distributions will be of interest due to their possible role in developing chain reactions via high energy fusion products [100, 101]. Understanding how beam-

target fusion reactions occur in non-equilibrium plasmas can be further enhanced by experimental measurements of the time-integrated neutron spectrum emitted by the plasma as well as the neutron yield. The variation in neutron yield with direction indicates that beam-target reactions are occurring in the pinch [102–104]. Thermal broadening of the neutron spectra will also indicate the presence of athermal fusion reactions taking place. Integrating such diagnostics in the simulations and benchmarking them with experimental data will be a powerful capability that can then be applied to optimizing target designs to enhance their yield.

REFERENCES

[1] Nasa strategic plan. Technical report, institution, 2018.

[2] Andrew Chaikin. *A Man on the Moon: The Triumphant Story of the Apollo Space Program*. Penguin Putnam Inc., 1994.

[3] T. Kammash, editor. *Fusion Energy in Space Propulsion*. AIAA, Washington, D.C., 1995.

[4] G. P. Sutton and O. Biblarz. *Rocket Propulsion Elements*. John Wiley and Sons, 2001.

[5] Robert G. Jahn. *Physics of Electric Propulsion*. Dover Publications, Inc., 2006.

[6] J. Cassibry, R. Cortez, M. Stanic, W. Seidler II, R. Adams, G. Statham, and L. Fabisinski. Case and development path for fusion propulsion. *Journal of Spacecraft and Rockets*, 52(2):595–612, 2015.

[7] J. R. McNally. Physics of fusion fuel cycles. *Nuclear Technology/Fusion*, 2:2–28, 1982.

[8] A. Martin, R. Eskridge, P. Fimognari, and M. H. Lee. Fireball: Fusion ignition rocket engine with ballistic ablative lithium liner. In *Space Technology & Applications International Forum*, 2006.

[9] F. Winterberg. *The Release of Thermonuclear Energy by Inertial Confinement: Ways Toward Ignition*. World Scientific Publishing Co., 2010.

[10] A. Pancotti, J. Slough, D. Kirtley, M. Pfaff, C. Pihl, and G. Votroubek. Mission design architecture for the fusion driven rocket. In *48th AIAA/ASME/SAE/ASEE Joint Propulsion Conference & Exhibit*, Atlanta, GA, 2012.

[11] Jack Katzenstein and Michael Sydor. Exploding wire as fast dynamic pinch. *Journal of Applied Physics*, 33(2):718–723, 1962.

[12] D.B. Harris and G.H. Miley. Burn performance of inertial confinement fusion targets. *Nuclear Fusion*, 28(1):25, 1988.

[13] Chi-Kang Li and Richard D Petrasso. Charged-particle stopping powers in inertial confinement fusion plasmas. *Physical Review Letters*, 70(20):3059, May 1993.

[14] A. E. Turrell, M. Sherlock, and S. J. Rose. Effects of large-angle Coulomb collisions on inertial confinement fusion plasmas. *Physical Review Letters*, 112(245002), June 2014.

[15] K A Long and N A Tahir. Theory and calculation of the energy loss of charged particles in inertial confinement fusion burning plasmas. *Nuclear Fusion*, 26(5):555–592, 1986.

[16] Lowell S Brown, Dean L Preston, and Robert L Singleton Jr. Charged particle motion in a highly ionized plasma. *Physics Reports*, 410(4):237–333, 2005.

[17] Paul E. Grabowski, Michael P. Surh, David F. Richards, Frank R. Graziani, and Michael S. Murillo. Molecular dynamics simulations of classical stopping power. *Physical Review Letters*, 111(215002), 2013.

[18] P. Sigmund. *Particle Penetration and Radiation Effects*. Springer Series in Solid-State Sciences. Springer-Verlag, 2006.

[19] H. P. Le. Hydrodynamic models for multicomponent plasmas with collisional-radiative kinetics.

[20] G. S. Fraley, E. J. Linnebur, R. J. Mason, and R. L. Morse. Thermonuclear burn characteristics of compressed deuteriumtritium microspheres. *Physics of Fluids*, 17(2):474–489, 1974.

[21] D. J. Sigmar and G. Joyce. Plasma heating by energetic particles. *Nuclear Fusion*, 11:447–456, 1971.

[22] R. Lovberg and S. Glasstone. *Controlled Thermonuclear Reactions: An Introduction to Theory and Experiment*. 1960.

[23] J. D. Huba. Nrl plasma formulary. United States Navy, Washington, DC 20375, 2013.

[24] S. Atzeni and J. Meyer-ter Vehn. *The Physics of Inertial Fusion - Beam Plasma Interaction, Hydrodynamics, Hot Dense Matter*. International Series of Monographs on Physics 125. Oxford Science Publications, 2004.

[25] Y. C. F. Thio. Magneto-inertial fusion: an emerging concept for inertial fusion and dense plasmas in ultrahigh magnetic fields. White paper, Department of Energy, Office of Fusion Energy Sciences, Germantown, MD, 2008.

[26] R C Kirkpatrick. Magnetized target fusion - an overview of the concept. Technical Report 94-4354, Los Alamos National Laboratory, 1994.

[27] R P Drake, J H Hammer, C W Hartman, L J Perkins, and D D Ryutov. Sub-megajoule liner implosion of a closed field line configuration. *Fusion Technology*, 30(3):310–325, Dec 1996.

[28] I. R. Lindemuth and R. E. Siemon. The fundamental parameter space of thermonuclear fusion. *American Journal of Physics*, 77(5):407–416, 2009.

[29] T P Intrator, J Y Park, J H Degnan, I Furno, C Grabowski, S C Hsu, E L Ruden, P G Sanchez, J M Taccetti, M Tuszewski, W J Waganaar, G A Wurden, S Y Zhang, and Z Wang. A high-density field reversed configuration plasma for magnetized target fusion. *IEEE Transactions on Plasma Science*, 32(1):152–160, Feb 2004.

[30] J. M. Taccetti, T. P. Intrator, G. A. Wurden, S. Y. Zhang, R. Aragonez, P. N. Assmus, C. M. Bass, C. Carey, S. A. deVries, W. J. Fienup, I. Furno, S. C. Hsu, M. P. Kozar, M. C. Langner, J. Liang, R. J. Maqueda, R. A. Martinez, P. G. Sanchez, K. F. Schoenberg, K. J. Scott, R. E. Siemon, E. M. Tejero, E. H. Trask, M. Tuszewski, W. J. Waganaar, C. Grabowski, E. L. Ruden, J. H. Degnan, T. Cavazos, D. G. Gale, and W. Sommars. Frx-l: A field-reversed configuration plasma injector for magnetized target fusion. July 2003. PACS 52.55.Lf.

[31] G. A. Wurden, T. P. Intrator, P. E. Sieck, L. Dorf, S. C. Hsu, R. M. Renneke, W. J. Waganaar, Zhehui Wang, J. H. Degnan, E. L. Ruden, M. Domonkos, P. Adamson, C. Grabowski, D. G. Gale, M. Kostora, W. Sommars, M. H. Frese, S. D. Frese, J. F. Camancho, S. K. Coffey, N. F. Roderick, P. Parks, R. E. Siemon, T. Awe, and A. G. Lynn. Frchx magnetized target fusion hedlp experiments. October 2008.

[32] Y. C. F. Thio, E. Panarella, R. C. Kirkpatrick, C. E. Knapp, and F. J. Wysocki. Magnetized target fusion in a spheroidal geometry with standoff drivers. In E. Panarella, editor, *Current Trends in International Fusion Research - Proceedings of the Second Symposium*, Ottawa, Canada, 1999. NRC Research Press.

[33] J. Cassibry, R. Samulyak, K. Schillo, W. Shih, and S. Hsu. Numerical modeling of plasma-liner formation and implosion for the plx-α project. *Bulletin of the American Physical Society*, 61(18), 2016.

[34] M. Stanic, J. T. Cassibry, and R. B. Adams. Project icarus: Analysis of plasma jet driven magneto-inertial fusion as potential primary driver for the icarus probe. *Acta Astronautica*, 86:47–54, 2013.

[35] J. D. Lawson. Some criteria for a useful thermonuclear reactor. techreport AERE GP/R -1807, Harwell, Berkshire, U.K., dec 1955.

[36] S. Pfalzner. *An Introduction to Inertial Confinement Fusion*. Series in Plasma Physics. CRC Press, 2006.

[37] Michael A. Liberman, John S. De Groot, Arthur Toor, and Rick B. Spielman. *Physics of High-Density Z-Pinch Plasmas*. Number ISBN: 978-0-387-98568-8. Springer, 1999.

[38] M. G. Haines. A review of the dense z-pinch. *Plasma Physics and Controlled Fusion*, 53(9):093001, 2011.

[39] Dmitri D. Ryutov. Characterizing the plasmas of dense z-pinches. *IEEE Transactions on Plasma Science*, 43(8), aug 2015.

[40] S V Lebedev, D J Ampleford, S N Bland, S C Bott, J P Chittenden, J Goyer, C Jennings, M G Haines, G N Hall, D A Hammer, J B A Palmer, S A Pikuz, T A Shelkovenko, and T Christoudias. Physics of wire array z-pinch implosions: experiments at imperial college. *Plasma Physics and Controlled Fusion*, 47(5A):A91, 2005.

[41] D. J. Ampleford, S. V. Lebedev, S. N. Bland, S. C. Bott, J. P. Chittenden, C. A. Jennings, V. L. Kantsyrev, A. S. Safronova, V. V. Ivanov, D. A. Fedin, P. J. Laca, M. F. Yilmaz, V. Nalajala, I. Shrestha, K. Williamson, G. Osborne, A. Haboub, and A. Ciardi. Dynamics of conical wire array z-pinch implosions. *Physics of Plasmas*, 14(10):102704, 2007.

[42] S. N. Bland, S. V. Lebedev, J. P. Chittenden, D. J. Ampleford, and G. Tang. Use of linear wire array z pinches to examine plasma dynamics in high magnetic fields. *Physics of Plasmas*, 11(11):4911–4921, 2004.

[43] J. P. Chittenden, S. V. Lebedev, B. V. Oliver, E. P. Yu, and M. E. Cuneo. Equilibrium flow structures and scaling of implosion trajectories in wire array z pinches. *Physics of Plasmas*, 11(3):1118–1127, 2004.

[44] C. A. Coverdale, C. Deeney, A. L. Velikovich, J. Davis, R. W. Clark, Y. K. Chong, J. Chittenden, S. Chantrenne, C. L. Ruiz, G. W. Cooper, A. J. Nelson, J. Franklin, P. D. LePell, J. P. Apruzese, J. Levine, and J. Banister. Deuterium gas-puff z-pinch implosions on the z accelerator. *Physics of Plasmas*, 14(5):056309, 2007.

[45] L. Christensen, M. Babineau, V. Kenyon, L. Whitehead, K. Brandon, C. Wellington, and K. Ware. Decade radiation test facility - plans and capabilities. *Space Technology Conference & Exhibit*, 1999.

[46] L. Tonks. Theory and phenomena of high current densities in low pressure arcs. *Journal of The Electrochemical Society*, 72(1):167–182, 1937.

[47] D. R. Welch, D. V. Rose, C. Thoma, R. E. Clark, C. B. Mostrom, W. A. Stygar, and R. J. Leeper. Kinetic simulations of a deuterium-tritium z pinch with 10^{16} neutron yield. *Physics of Plasmas*, 18(5), 2011.

[48] J D Sethian, A E Robson, K A Gerber, and A W DeSilva. Enhanced stability and neutron production in a dense z-pinch plasma formed from a frozen deuterium fiber. *Physical Review Letters*, 59(8):892–895, aug 1987.

[49] D. R. Welch, D. V. Rose, R. E. Clark, C. B. Mostrom, W. A. Stygar, and R. J. Leeper. Fully kinetic particle-in-cell simulations of a deuterium gas puff z-pinch. *Physical Review Letters*, 103(25), 2009.

[50] A. L. Velikovich, R. W. Clark, J. Davis, Y. K. Chong, C. Deeney, C. A. Coverdale, C. L. Ruiz, G. W. Cooper, A. J. Nelson, J. Franklin, and L. I. Rudakov. Z-pinch plasma neutron sources. *Physics of Plasmas*, 14(2):022701, 2007.

[51] M. G. Haines, M. Coppins, and I. D. Culverwell. The inapplicability of ideal mhd stability theory to the dense zpinch. *AIP Conference Proceedings*, 195(1):203–210, 1989.

[52] O. A. Anderson, W. R. Baker, S. A. Colgate, J. Ise Jr., and R. V. Pyle. Neutron production in linear deuterium pinches. *Physical Review*, 110(6), 1958.

[53] M. Kruskal and M. Schwarzchild. Some instabilities of a completely ionized gas. 223:348.

[54] I. Kurchatov. On the possibility of producing thermonuclear reactions in a gas discharge. 4:193.

[55] M. S. Derzon, P. C. Galambos, and E. C. Hagen. Analytical estimation of neutron yield in a micro gas-puff x pinch. *Journal of Applied Physics*, 112(11):114516, 2012.

[56] Brian L. Bures and Mahadevan Krishnan. An alternative scaling model for neutron production in z-pinch devices. *Physics of Plasmas*, 19(11), 2012.

[57] B. Appelbe and J. Chittenden. Understanding neutron production in the deuterium dense plasma focus. *AIP Conference Proceedings*, 1639:9–14, 2014.

[58] B. L. Bures, M. Krishnan, and Y. Eshaq. Controlling the neutron yield from a small dense plasma focus using deuterium-inert gas mixtures. *AIP Conference Proceedings*, 1088:195–198, 2009.

[59] B. L. Bures, M. Krishnan, R. E. Madden, and F. Blobner. Enhancing neutron emission from a 500-J plasma focus by altering the anode geometry and gas composition. *IEEE Transactions on Plasma Science*, 38(4):667–671, 2010.

[60] W. L. Atchison and D. S. Lemons. Magnetically driven Rayleigh-Taylor instability with acceleration gradient. *IEEE Transactions on Plasma Science*, 32(6):2169–2174, 2004.

[61] F. Hamann, H. Calamy, C. Mangeant, F. Lassalle, and F. Bayol. How to maximize the radius of a wire-array z-pinch for the 100 ns to 1 μ s implosion time scales. *IEEE Transactions on Plasma Science*, 34(5):2263–2267, 2006.

[62] M. D. Johnston, Y. Y. Lau, R. M. Gilgenbach, T. S. Strickler, M. C. Jones, M. E. Cuneo, and T. A. Mehlhorn. Caterpillar structures in single-wire z-pinch experiments. *Applied Physics Letters*, 83(24):4915–4917, 2003.

[63] R. B. Baksht, A. V. Fedunin, A. Yu Labetsky, A. G. Russkikh, A. V. Shishlov, O. V. Diyankov, I. V. Glazyrin, and S. V. Koshelev. On stabilization of gas puff implosions: experiment and simulation. *IEEE Transactions on Plasma Science*, 26(4):1259–1266, 1998.

[64] A. Yu Labetsky, R. B. Baksht, V. I. Oreshkin, A. G. Rousskikh, and A. V. Shishlov. An experimental study of the effect of Rayleigh-Taylor instabilities on the energy deposition into the plasma of a Z pinch. *IEEE Transactions on Plasma Science*, 30(2):524–531, 2002.

[65] Ross J. Cortez and Jason T. Cassibry. Stopping power in d^6li plasmas for target ignition studies. *Nuclear Fusion*, 58(2):026009, 2018.

[66] R. L. Singleton Jr. Charged particle stopping power effects on ignition: Some results from an exact calculation. *Physics of Plasmas*, 15(056302), 2008.

[67] J. Jacoby, H. Hoffmann, W. Laux, R. Muller, H. Wahl, K. Weyrich, E. Boggasch, B. Heimrich, C. Stockl, H. Wetzler, and S. Miyamoto. Stopping of heavy ions in a hydrogen plasma. *Physical Review Letters*, 74(9), 1995.

[68] Zhigang Wang, Zhen-Guo Fu, and Ping Zhang. Theoretical studies on the stopping power of deuterium-tritium mixed with uranium plasmas for α particles. *Physics of Plasmas*, 21(102307), 2014.

[69] B. Badger, F. Arendt, K. Becker, K. Beckert, R. Bock, D. Bhne, I. Bozsik, J. Brezina, M. Dalle Donne, L. El-Guebaly, R. Engelstad, W. Eyrich, R. Frhlich, N. Ghoniem, B. Goel, A. Hassanein, D. Henderson, W. Hbel, I. Hofmann, E. Hoyer, R. Keller, G. Kessler, A. Klein, R. Kreutz, G. Kulcinski, E. Larsen, K. Lee, K. Long, N. Metzler, J. Meyer-ter Vehn, U. von Mllendorff, N. Moritz, G. Moses, R. Mller, K. O'Brien, R. Peterson, K. Plute, L. Pong, R. Sanders, J. Sapp, M. Sawan, K. Schretzmann, T. Spindler, I. Sviatoslavsky, K. Symon, D. Sze, N. Tahir, W. Vogelsang, A. White, S. Witkowski, and H. Wollnick. *HIBALL : a conceptual heavy ion beam driven fusion reactor study volume 2; Als Ms vervielfltigt*, volume KfK 3202 /2 of *HIBALL : a conceptual heavy ion beam driven fusion reactor study*. Kernforschungszentrum, Karlsruhe, 1981. Literaturangaben; English.

[70] M. Temporal, B. Canaud, W. Cayzac, R. Ramis, and R. Singleton Jr. Effects of alpha stopping power modelling on the ignition threshold in a directly-driven inertial confinement fusion capsule. *European Physical Journal D*, 71(132), 2017.

[71] T. Peter and J. Meyer-ter Vehn. Energy loss of heavy ions in dense plasma. i. linear and nonlinear vlasov theory for the stopping power. *Physical Review A*, 43(4), feb 1991.

[72] Jason T. Cassibry, Ross Cortez, Coleton Cody, Seth Thompson, and Lloyd Jackson. Three dimensional modeling of pulsed fusion for propulsion and terrestrial power using smooth particle fluid with maxwell equation solver (spfmax). In *53rd AIAA/SAE/ASEE Joint Propulsion Conference*, AIAA Propulsion and Energy Forum. American Institute of Aeronautics and Astronautics, July 2017.

[73] J A Frenje, P E Grabowski, C K Li, F H Seguin, A B Zylstra, M Gatu Johnson, R D Petrasso, V Yu Glebov, and T C Sangster. Measurements of ion stopping around the bragg peak in high-energy-density plasmas. *Physical Review Letters*, 115(205001), nov 2015.

[74] A B Zylstra, J A Frenje, P E Grabowski, C K Li, G W Collins, P Fitzsimmons, S Glenzer, F Graziani, S B Hansen, S X Hu, M Gatu Johnson, P Keiter, H Reynolds, J R Rygg, F H Seguin, and R D Petrasso. Measurement of charged-particle stopping in warm dense plasma. *Physical Review Letters*, 114(215002), may 2015.

[75] D. G. Hicks, C. K. Li, F. H. Seguin, A. K. Ram, J. A. Frenje, R. D. Petrasso, J. M. Soures, V. Yu Glebov, D. D. Meyerhofer, S. Roberts, C. Sorce, C. Stockl, T. C. Sangster, and T. W. Phillips. Charged-particle acceleration and energy loss in laser-produced plasmas. *Physics of Plasmas*, 7(12), 2000.

[76] F. R. Graziani, V. S. Batista, L. X. Benedict, J. I. Castor, H. Chen, S. N. Chen, C. A. Fichtl, J. N. Glosli, P. E. Grabowski, A. T. Graf, S. P. Hau-Riege, A. U. Hazi, S. A. Khairallah, L. Krauss, A. B. Langdon, R. A. London, A. Markmann, M. S. Murillo, D. F. Richards, H. A. Scott, R. Shepherd, L. G. Stanton, F. H. Streitz, M. P. Surh, J. C. Weisheit, and H. D. Whitley. Large-scale molecular dynamic simulations of dense plasmas: The cimarron project. *High Energy Density Physics*, 8:105–131, 2012.

[77] M. K. Issanova, S. K. Kodanova, T. S. Ramazanov, N. Kh. Bastykova, Zh. A. Moldabekov, and C.-V. Meister. Classical scattering and stopping power in dense plasmas: the effect of diffraction and dynamic screening. *Laser and Particle Beams*, 34(3):457–466, may 2016.

[78] M. M. et al Marinak. Three-dimensional hydra simulations of national ignition facility targets. *Physics of Plasmas*, 8:2275, 2001.

[79] R. E. J. Peterkin, M. H. Frese, and C. R. Sovinec. Transport of magnetic flux in an arbitrary coordinate ale code. *Journal of Computational Physics*, 140:148–171, 1998.

[80] G. B. Zimmerman and W. L. Kruer. *Comments on Plasma Physics and Controlled Fusion*, 2:51, 1975.

[81] D. R. Welch, D. V. Rose, B. V. Oliver, and R. E. Clark. Simulation techniques for heavy ion fusion chamber transport. *Nuclear Instruments and Methods*, 464(1-3):134–139, may 2001.

[82] C. D. Levermore and G. C. Pomraning. A flux-limited diffusion theory. *Astrophysical Journal*, 248:321–334, 1981.

[83] R. A. Agnew, J. T. Cassibry, and B. H. Winterling. Analytic model to estimate thermonuclear neutron yield in z-pinches using the magnetic noh problem. *IEEE Transactions on Plasma Science*, 44(10):2181–2189, 2016.

[84] J J Monaghan. Smoothed particle hydrodynamics. *Reports on Progress in Physics*, 68(8):1703, 2005.

[85] Ya. B. Zel'dovich and Yu. P. Raizer. *Physics of Shock Waves and High-Temperature Hydrodynamic Phenomena*. Dover Publications, Inc., Mineola, NY, 2002.

[86] J.G. Linhart and L. Bilbao. Zpinch spark of an axial detonation in dt. *Nuclear Fusion*, 40(5):941, 2000.

[87] J. G. Linhart, L. Bilbao, R. Miklaszewski, and W. Stepniewski. Detonation energy amplification in conical channels. *Plasma Physics Reports*, 26(3):203–218, 2000.

[88] D. R. Welch, D. V. Rose, C. Thoma, R. E. Clark, C. B. Mostrom, W. A. Stygar, and R. J. Leeper. Kinetic simulation of thermonuclear-neutron production by a 10^7-a deuterium Z pinch. *Physics of Plasmas*, 17(072702), 2010.

[89] M. G. Haines, P. D. LePell, C. A. Coverdale, B. Jones, C. Deeney, and J. P. Apruzese. Ion viscous heating in a magnetohydrodynamically unstable z pinch at over 2×10^9 kelvin. *Physical Review Letters*, 96(075003), 2006.

[90] L. S. Brown, D. L. Preston, and R. L. Singleton Jr. Electron-ion energy partition when a charged particle slows in a plasma: Theory. *Physical Review E*, 86(016407), 2012.

[91] L. S. Brown, D. L. Preston, and R. L. Singleton Jr. Electron-ion energy partition when a charged particle slows in a plasma: Results. *Physical Review E*, 86(016406), 2012.

[92] B. He, Z. Wang, and J. Wang. Slowing down of alpha particles in icf dt plasmas. *Physics of Plasmas*, 25(012704), 2018.

[93] J. R. McNally Jr. Fusion chain reactions - i. *Nuclear Fusion*, 11:187–189, jan 1971.

[94] J. R. McNally Jr. Fusion chain reactions - ii. *Nuclear Fusion*, 11:189–191, jan 1971.

[95] J. R. McNally Jr. Fusion chain reactions - iii - the production of mev plasmas. *Nuclear Fusion*, 11:191–193, jan 1971.

[96] J. R. McNally Jr. Autocatalytic burning of 6lid nuclear fuel via the p + 9be resonance reaction. *Nuclear Fusion*, 11:554–556, jun 1971.

[97] M M Basko, A J Kemp, and J Meyer ter Vehn. Ignition conditions for magnetized target fusion in cylindrical geometry. *Nuclear Fusion*, 40(1):59–68, 2000.

[98] I. R. Lindemuth. The ignition design space of magnetized target fusion. *Physics of Plasmas*, 22(122712), 2015.

[99] I. R. Lindemuth. An extended study of the ignition design space of magnetized target fusion. *Physics of Plasmas*, 24(055602), 2017.

[100] V. T. Voronchev, V. I. Kukulin, and V. M. Krasnopol'skij. The kinetics of nuclear processes in hot D^6Li and DD plasmas. *Nuclear Fusion*, 24(9), 1984.

[101] M. J. Hay and N. J. Fisch. Ignition threshold for non-maxwellian plasmas. *Physics of Plasmas*, 22(112116), 2015.

[102] D Klir. *The Study of a Fibre Z-Pinch*. PhD thesis, Czech Technical University in Prague, 2005.

[103] D. Klir, J. Kravarik, P. Kubes, K. Rezac, S. S. Ananev, Yu. L. Bakshaev, P. I. Blinov, A. S. Chernenko, E. D. Kazakov, V. D. Korolev, B. R. Meshcherov, G. I. Ustroev, L. Juha, J. Krasa, and A. Velyhan. Neutron emission generated during wire array z-pinch implosion onto deuterated fiber. *Physics of Plasmas*, 15(3), 2008.

[104] D. Klir, A. V. Shishlov, V. A. Kokshenev, P. Kubes, A. Yu. Labetsky, K. Rezac, R. K. Cherdizov, J. Cikhardt, B. Cikhardtova, G. N. Dudkin, F. I. Fursov, A. A. Garapatsky, B. M. Kovalchuk, J. Krasa, J. Kravarik, N. E. Kurmaev, H. Orcikova, V. N. Padalko, N. A. Ratakhin, O. Sila, K. Turek, V. A. Varlachev, A. Velyhan, and R. Wagner. Deuterium z-pinch as a powerful source of multi-mev ions and neutrons for advanced applications. *Physics of Plasmas*, 23(3), 2016.